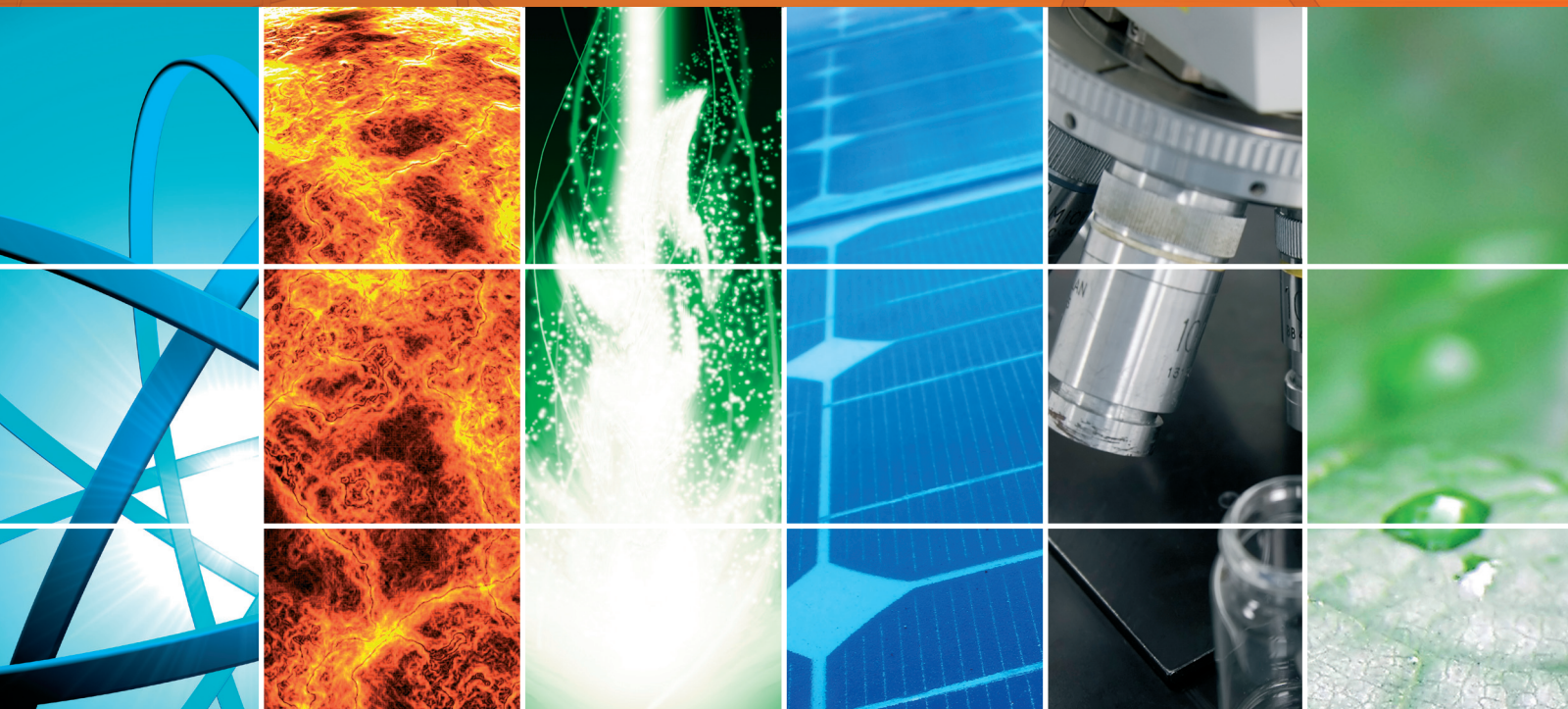


Nanotechnology for Solar Energy 2012

Guest Editors: M. S. A. Abdel-Mottaleb, Xavier Allonas,
James T. McLeskey, and Latika Menon





Nanotechnology for Solar Energy 2012

International Journal of Photoenergy

Nanotechnology for Solar Energy 2012

Guest Editors: M. S. A. Abdel-Mottaleb, Xavier Allonas,
James T. McLeskey, and Latika Menon



Copyright © 2012 Hindawi Publishing Corporation. All rights reserved.

This is a special issue published in "International Journal of Photoenergy." All articles are open access articles distributed under the Creative Commons Attribution License, which permits unrestricted use, distribution, and reproduction in any medium, provided the original work is properly cited.

Editorial Board

M. Sabry Abdel-Mottaleb, Egypt
Nihal Ahmad, USA
Nicolas Alonso-Vante, France
Wayne A. Anderson, USA
Vincenzo Augugliaro, Italy
Detlef W. Bahnemann, Germany
Mohammad A. Behnajady, Iran
Ignazio Renato Bellobono, Italy
Raghu N. Bhattacharya, USA
Pramod H. Borse, India
Gion Calzaferri, Switzerland
Adriana G. Casas, Argentina
Wonyong Choi, Korea
Věra Cimrova, Czech Republic
Vikram Dalal, USA
D. Demetriou Dionysiou, USA
Mahmoud M. El-Nahass, Egypt
Ahmed Ennaoui, Germany
Chris Ferekides, USA
Beverley Glass, Australia
M. A. Gondal, Saudi Arabia
Shinya Higashimoto, Japan
Yadong Jiang, China

Chun-Sheng Jiang, USA
Shahed Khan, USA
Cooper Harold Langford, Canada
Yuexiang Li, China
Stefan Lis, Poland
N. Mohammad Mahmoodi, Iran
Dionissios Mantzavinos, Greece
Ugo Mazzucato, Italy
Jacek Miller, Poland
Jarugu N. Moorthy, India
Franca Morazzoni, Italy
Fabrice Morlet-Savary, France
Ebinazar B. Namdas, Australia
Maria da Graa P. Neves, Portugal
Leonidas Palilis, Greece
Leonardo Palmisano, Italy
Ravindra K. Pandey, USA
David Lee Phillips, Hong Kong
Pierre Pichat, France
Gianluca Li Puma, UK
Xie Quan, China
Tijana Rajh, USA
Peter Robertson, UK

Avigdor Scherz, Israel
Lukas Schmidt-Mende, Germany
Panagiotis Smirniotis, USA
Zofia Stasicka, Poland
Juliusz Sworakowski, Poland
Nobuyuki Tamaoki, Japan
G. N. Tiwari, India
Nikolai V. Tkachenko, Finland
Veronica Vaida, USA
Roel van De Krol, Germany
Mark van Der Auweraer, Belgium
Ezequiel Wolcan, Argentina
Man Shing Wong, Hong Kong
David Worrall, UK
Fahrettin Yakuphanoglu, Turkey
Minjoong Yoon, Korea
Hongtao Yu, USA
Jimmy C. Yu, Hong Kong
Jun-Ho Yum, Switzerland
Klaas Zachariasse, Germany
Lizhi Zhang, China
Jincai Zhao, China

Contents

Effect of Carbon Modification on the Electrical, Structural, and Optical Properties of TiO₂ Electrodes and Their Performance in Labscale Dye-Sensitized Solar Cells, R. Taziwa, E. L. Meyer, E. Sideras-Haddad, R. M. Erasmus, E. Manikandan, and B. W. Mwakikunga

Volume 2012, Article ID 904323, 9 pages

Influence of TiO₂ Nanocrystals Fabricating Dye-Sensitized Solar Cell on the Absorption Spectra of N719 Sensitizer, Puhong Wen, Yinfeng Han, and Weixing Zhao

Volume 2012, Article ID 906198, 7 pages

Effect of Accelerated Thermal Ageing on the Selective Solar Thermal Harvesting Properties of Multiwall Carbon Nanotube/Nickel Oxide Nanocomposite Coatings, Kittessa T. Roro, Bonex Mwakikunga, Ngcali Tile, Brian Yalisi, and Andrew Forbes

Volume 2012, Article ID 678394, 7 pages

Photoelectrochemical Performance of Smooth TiO₂ Nanotube Arrays: Effect of Anodization Temperature and Cleaning Methods, Chin Wei Lai and Srimala Sreekantan

Volume 2012, Article ID 356943, 11 pages

CdSe Quantum Dots for Solar Cell Devices, A. B. Kashyout, Hesham M. A. Soliman, Marwa Fathy, E. A. Gomaa, and Ali A. Zidan

Volume 2012, Article ID 952610, 7 pages

Electric Characterization and Modeling of Microfluidic-Based Dye-Sensitized Solar Cell, Adriano Sacco, Andrea Lamberti, Marzia Quaglio, Stefano Bianco, Elena Tresso, Anca-Luiza Alexe-Ionescu, and Candido F. Pirri

Volume 2012, Article ID 216780, 11 pages

Research Article

Effect of Carbon Modification on the Electrical, Structural, and Optical Properties of TiO₂ Electrodes and Their Performance in Labscale Dye-Sensitized Solar Cells

R. Taziwa,¹ E. L. Meyer,¹ E. Sideras-Haddad,² R. M. Erasmus,²
E. Manikandan,³ and B. W. Mwakikunga^{4,5}

¹ Institute of Technology, University of Fort Hare, Private Bag X1314, Alice 5700, South Africa

² Center of Excellence in Strong Materials, School of Physics, University of Witwatersrand, Braamfontein 2000, Johannesburg, South Africa

³ Nano Research Centre, PNTC, B. S. Abdur Rahman University, Chennai 600048, India

⁴ CSIR National Centre for Nano-Structured Materials, P. O. Box 395, Pretoria 001, South Africa

⁵ Department of Physics, University of Malawi-The Polytechnic, Private Bag 303, Chichiri, Blantyre 3, Malawi, South Africa

Correspondence should be addressed to B. W. Mwakikunga, bmwakikunga@csir.co.za

Received 6 February 2012; Accepted 15 June 2012

Academic Editor: Latika Menon

Copyright © 2012 R. Taziwa et al. This is an open access article distributed under the Creative Commons Attribution License, which permits unrestricted use, distribution, and reproduction in any medium, provided the original work is properly cited.

Carbon-modified titanium dioxide nanoparticles (C:TiO₂ NPs) have been synthesized by ultrasonic nebulizer spray pyrolysis (USP) and pneumatic spray pyrolysis (PSP) techniques. HRTEM on the NPs shows difference in lattice spacing in the NP structures prepared by the two methods—2.02 Å for the USP NPs and an average of 3.74 Å for the PSP NPs. The most probable particle sizes are 3.11 nm and 5.5 nm, respectively. Raman spectroscopy supported by FTIR confirms the TiO₂ polymorph to be anatase with the intense phonon frequency at 153 cm⁻¹ blue-shifted from 141 cm⁻¹ ascribed to both carbon doping and particle size. A modified phonon confinement model for nanoparticles has been used to extract phonon dispersion and other parameters for anatase for the first time. Electronic measurements show “negative conductance” at some critical bias voltage, which is characteristic of *n*-type conductivity in the carbon-doped TiO₂ NPs as confirmed by the calculated areas under the *I*-*V* curves, a property suited for solar cell applications. Practical solar cells built from carbon-doped TiO₂ electrodes show up to 1.5 times improvement in efficiency compared to pure TiO₂ electrodes of similar construction.

1. Introduction: Efficiency Improvement Efforts on Dye Solar Cells

Various tables reporting figures of efficiency for different types of solar cells have been released several times by different groups. But the most up-to-date chart has been released by the National Renewable Energy Laboratory [1]. The chart shows that efficiency values for all solar cell types are steadily increasing from the earliest reported levels in the 1970s and 1980s. The highest values from 16–41% are found in multijunction concentrators GaAs with the latest (2007) figure of 41% reported by Boeing. Crystalline silicon cells range from 16–24%, multicrystalline Si from 12–18%, thin-film solar cells containing either Cu(In,Ga)Se₂ or CdTe

or amorphous SiH or nano-Si or micro-Si or poly-Si or multijunction Si ranging from 1–17%. The rapid increase in efficiency in nano-Si from about 8% in 1997 to 14% in 2001 demonstrates the importance of nanotechnologies in the improvement of the solar cells level of efficiency. Dye-sensitized solar cells (DSSCs) with a range of 5% in 1991 to 11% in 2006 have nearly the lowest range with the partners—the organic solar cells—at the lowest end of 1% in 2001 to 5.4% in 2006.

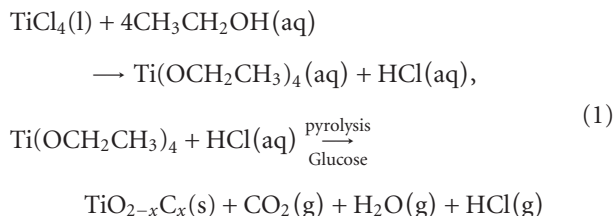
Solar cell types displaying the highest efficiency figures are difficult to produce due to material processing costs such as in silicon and GaAs alloys or precursor toxicity such as in selenides and sulfides and hence expensive [2]. These disadvantages are not an issue in low efficient types such as

the organic ones and the dye-sensitized cells. For the reasons of nontoxicity and the possibility of mass production from low-cost starting materials, it is wise to study the materials properties for the emerging solar cell types especially the dye-sensitized one. The discovery of the pertinent properties that would drastically raise the efficiency of DSSCs will be very indispensable. The DSSCs, the Grätzel cells, consist of thin films of *n*-type titanium dioxide (TiO₂) coated with a ruthenium metal organic dye [3]. They offer easy processing and can attain new roles over conventional silicon solar cells. Generally, the ways explored to improve the efficiency of DSSCs have focused on upgrading the components of the solar cell to enhance photovoltage (*V*_{OC}) by varying (a) the supporting oxide, (b) the electrolyte which stabilizes the solar cell, and (c) the dyes which enhance the photocurrent [4, 5]. Carbon in DSC electrodes has gained attention recently, for instance, flexible C to complete with Pt:FTOs [6], C:TiO₂ for photocatalysis [7–9].

We report on the optical, structural, and electronic properties of TiO₂ NPs when doped with carbon (C:TiO₂ NPs) synthesized by spray pyrolysis and how that C:TiO₂ NPs increase the visible light absorption coefficient. These C:TiO₂ NPs are tested in DSSCs.

2. Experimental: Preparation and Characterization of Carbon Modified TiO₂

The proposed reaction sequence for the production of C:TiO₂ NPs, similar to that proposed by Livage [10] in the production of vanadium ethoxide and Mwakikunga et al. [11] in the production of tungsten ethoxide, is as follows:



C:TiO₂ NPs were synthesized by USP and PSP. The schematics for USP and PSP are given in Figure 1.

The USP technique involves focusing ultrasound waves of frequency *F* producing capillary waves of frequency *f*_{USP} at the surface of the precursor liquid. This produces ultrafine droplets of the precursor liquid. The ultrasonic nebulizer uses an ultrasound generator to drive a piezoelectric crystal at a fixed frequency, *F*. The surface of the liquid will break down when the longitudinal waves propagate from the crystal to the liquid-air interface. The PSP involves blowing the precursor liquid through fine nozzles to produce a mist of the precursor liquid at audible sound and ultrasonic frequencies, *f*_{PSP}. In both cases, the precursor droplets were generated in a chamber that was housing the nebulizer. The vapors generated are transported to a heated zone through a quartz tube onto glass substrate precoated with a transparent conducting layer of F:SnO₂ placed inside a furnace. The spray deposition is carried out for an hour. The wavelength of the capillary waves

is expressed as $\lambda = (8\pi\sigma/\rho \cdot f^2)^{1/3}$ where σ and ρ are the surface tension and density of the liquid, which, for high enough intensity of the forcing sound, erupt into droplets of mean diameter $D_{\text{USP}} = (8\pi\sigma/\rho \cdot f_{\text{USP}}^2)^{1/3}$ and $D_{\text{PSP}} = (8\pi\sigma/\rho \cdot f_{\text{PSP}}^2)^{1/3}$ respectively. After decomposition and deposition in the pyrolysis process, the solid-state particles obtained have mean diameter that can be estimated respectively as $d_{\text{USP}} = (D_{\text{USP}}(C_{\text{pr}}M_{\text{p}})/(\rho_{\text{p}}M_{\text{pr}}))^{1/3}$ and $d_{\text{PSP}} = (D_{\text{PSP}}(C_{\text{pr}}M_{\text{p}})/(\rho_{\text{p}}M_{\text{pr}}))^{1/3}$ where *C*_{pr} is the concentration of the precursor, *M*_{pr} and *M*_p are the molar masses of the precursor and deposited particles respectively; and ρ_{p} and ρ_{pr} are the densities of the deposited particles and precursor liquid respectively [12–15].

An aliquot of 0.1 M precursor solution of titanium ethoxide was prepared by adding 11.8825 g of titanium tetrachloride (TiCl₄) and 0.2162 g of glucose into a 250 mL volumetric flask in absolute ethanol (99.99%, Aldrich). The solution was then mixed vigorously till all the glucose particles were not visible. The precursor solution was then decanted into (1) a chamber that was housing the ultrasonic nebulizer operating at a frequency of 1.67 MHz for USP and (2) into tube connected to a pneumatic pump for PSP. F:SnO₂ transparent glass substrates were first washed with detergent then thoroughly rinsed with distilled water, isopropanol, distilled water and finally acetone. The glass substrates were then dried under hot air to evaporate the acetone. Nano-particle deposition was done on F:SnO₂ glass substrate at furnace temperatures of 450–455°C, at various substrate positions inside the furnace using argon as the carrier gas at a flow rate of 5.5 mL/min. Structural studies of the as deposited nano-particles were done using a Philips XPert powder X-ray diffractometer with a CuK_α wavelength of 0.154184 nm. High resolution transmission electron micrography (HRTEM) performed on a Jeol JSM 2100 was used to determine structure—lattice parameters—of the C:TiO₂ NPs; the HRTEM was also equipped with the energy dispersive X-ray spectroscopy (EDXS) setup using a Thermo Fisher Scientific detector cooled at liquid nitrogen temperature. Optical characterization (Diffuse reflectance spectra) was done using a Varian Cary Uv-Vis-IR spectrometer in the wavelength range of 250–2000 nm.

Raman spectroscopy (RS) was carried out using a Jobin-Yvon T64000 Raman spectrograph with a 514.5 nm line from an argon ion laser. The power of the laser at the sample at the post-annealed samples was small enough (0.384 mW) in order to minimise localised heating of the sample. The T64000 was operated in single spectrograph mode, with the 1800 lines/mm grating and three objective lenses on the microscope with the following magnifications: 20x, 50x and 100x.

Fourier Transform Infrared (FTIR) spectra of both pure and carbon modified titanium dioxide samples were carried out in the 350–4000 cm^{−1} frequency range. The infrared absorption spectra were recorded on Nicolet Nexus 870 system FTIR spectrometer at room temperature. Dried solid samples were pressed with KBr (FT-IR grade Aldrich) and pellets were scanned 34 times using transmission mode with a resolution of 4 cm^{−1}.

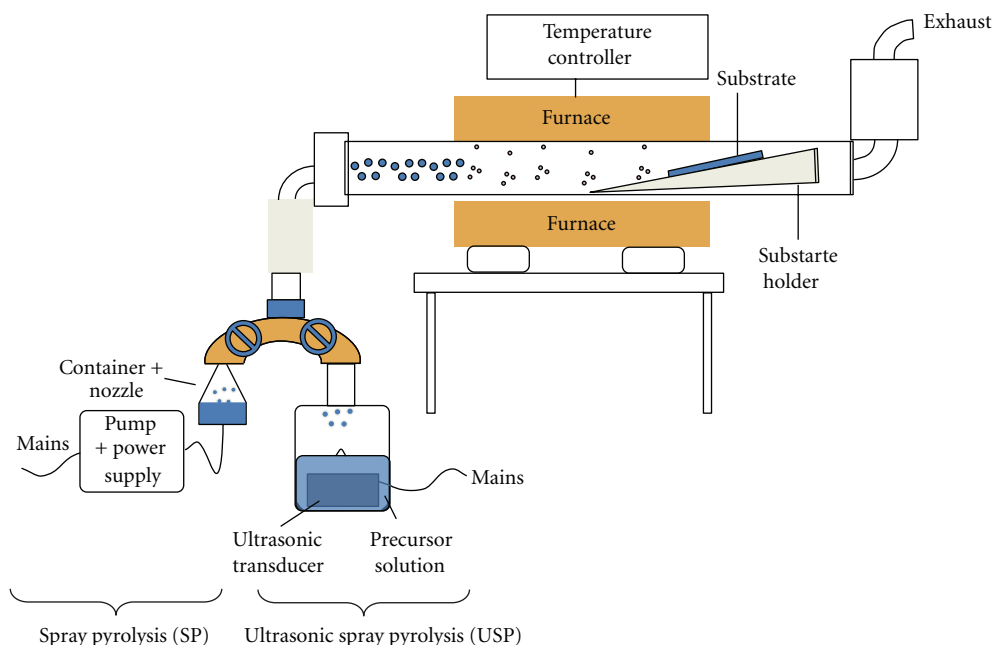


FIGURE 1: Schematic setup of pneumatic spray pyrolysis (PSP) and ultrasonic spray pyrolysis (USP).

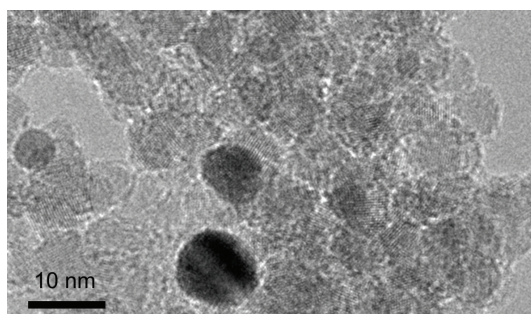


FIGURE 2: HRTEM image C:TiO₂ QDs growing by PSP.

A colinear four-point probe system from Cascade Microtech, Inc., Oregon, USA was used to perform conductance measurements on the C:TiO₂ NPs. The equidistant tungsten carbide probes have a separation distance, a , of 0.127 cm and a probe radius of 0.005 cm. The Keithley 4200 semiconductor characterization system (SCS), equipped with four supply-and-measure units (SMUs) and a pre-amplifier, was used to perform high-precision direct-current characterization capable of probing-sensitive voltages and injecting currents ranging from 1 fA–1 mA with a resolution of 0.1 fA. In this work, a current was injected through two extreme probes through the sample. The potential difference was measured across the middle probes.

3. Structural Properties of the Carbon-Modified TiO₂ Anatase

The lower magnification HRTEM showed that for the PSP prepared sample the particles were mostly spherical and had

mean diameter of 5.5 nm. The same can be said of the USP prepared sample only the particle size is smaller (Figure 2). In this case, the mean diameter is 3.11 nm. The EDXS of these PSP synthesized C:TiO₂ NPs (not shown) showed presence of Ti, O and C only signifying the purity of the obtained material. Cu peaks and some C intensity came from the carbon-hole copper grids used in these experiments.

TiO₂ exists in the following known polymorphs: anatase ($a = 3.784 \text{ \AA}$, $c = 9.514 \text{ \AA}$, $\alpha = \beta = \gamma = 90^\circ$ PDF# 78-2486) with the strongest d -spacing of 3.52 \AA [16], rutile ($a = 4.593 \text{ \AA}$, $c = 2.958 \text{ \AA}$, $\alpha = \beta = \gamma = 90^\circ$ PDF# 89-8304) with a d -spacing of 3.25 \AA [17] brookite ($a = 9.174 \text{ \AA}$, $b = 5.449 \text{ \AA}$, $c = 5.138 \text{ \AA}$, $\alpha = \beta = \gamma = 90^\circ$ PDF# 76-1934) with a d -spacing of 3.51 \AA [18] and hongquite ($a = 4.173 \text{ \AA}$, $\alpha = \beta = \gamma = 90^\circ$ PDF# 89-3660) with a d -spacing of 2.09 \AA [19].

The higher magnification HRTEM clearly reveals that USP TiO₂ NPs have a very small d -spacing compared to the normal anatase spacing of 0.352 nm . The d -spacing found in this sample is about 0.202 nm as shown Figure 3.

However, the PSP C:TiO₂ NPs have a distribution of interplanar d -spacings whose distribution is given in Figure 4(b) indicating that some particles have their d -spacings less or more than 0.352 nm . In fact, most of the particles have most probably d -spacing of 0.374 nm in agreement with the anatase TiO₂ as found by Bersani et al. [17]. It has been observed, especially in ZnO, that carbon doping, where C substitutes O, tends to reduce the d -spacing of the C:ZnO. It can, therefore, be concluded that those C:TiO₂ NPs that show larger d -spacings than the anatase observed in PSP samples have interstitial carbon doping as presented in Figure 4. The lower d -spacings suggest substitutional C doping as seen in some particles in the PSP sample and in almost all the particles in the USP sample.

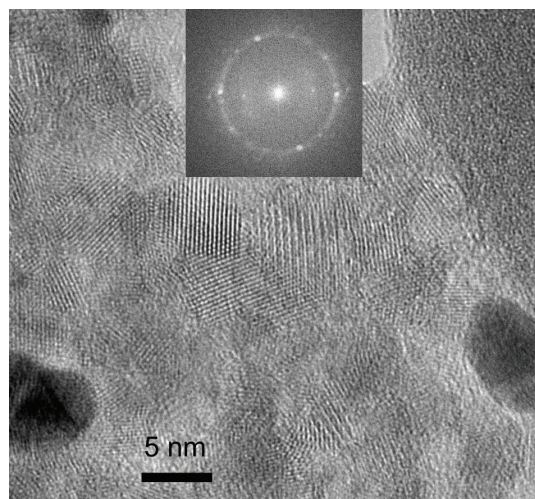


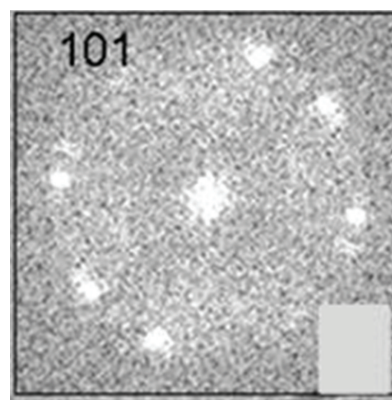
FIGURE 3: HRTEM of the USP C:TiO₂ QDs evident with a fringe separation of 2.017 Å. Inset is the FFT of the high-resolution image showing the reflection from the predominant (101) plane of the TiO₂ lattice.

We can, therefore, speculate that USP is a more efficient technique for incorporating carbon uniformly in the TiO₂ matrix. On the other hand, such a large change in lattice spacing, compounded with the large distribution shown in Figure 4(b) cannot be entirely due to carbon doping. This can be attributed to the fact there are various types of crystallites in the intrinsic TiO₂ material itself. Therefore, we can conclude this is a polycrystalline material.

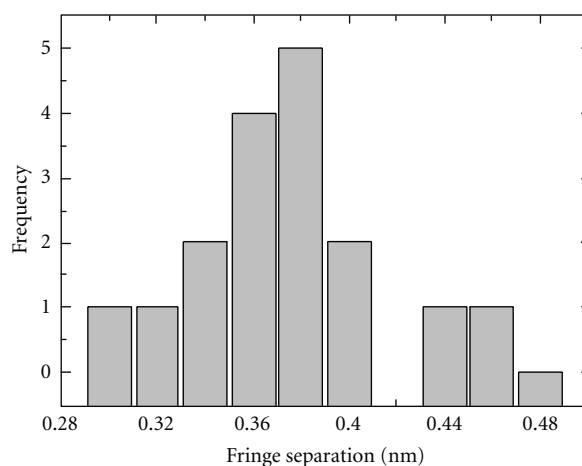
The fast Fourier transform (FFT) of the images, synonymous to the selected area electron diffraction, displays the fact that only the main diffraction (reflection) plane of Miller indices (101) in TiO₂ [17] is responsible for diffraction pattern. In the PSP sample, the particles with the same Miller indices are oriented in different direction. This is why their spots on the FFT image (Figure 4 inset a) give a circle of uniform radius, which is indexed to the (101) plane. However, in the USP sample, the particles tend to show similar orientation with one direction on the FFT image (Figure 3(b)).

4. Phonons in the C_xTiO_{2-x} Alloy

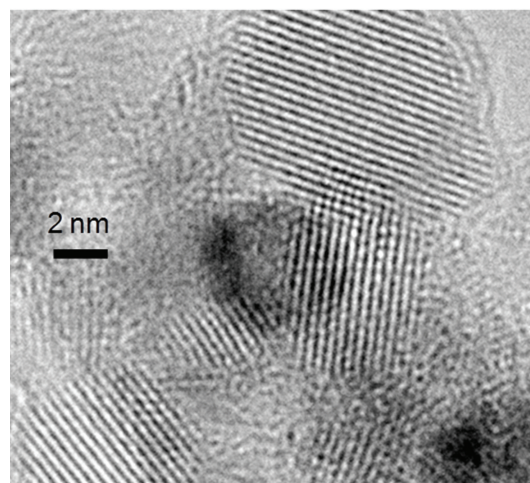
The FTIR spectra for pure unannealed TiO₂ (Pure TiO₂ spot 1 in Figure 5), pure annealed TiO₂ at 500°C (pure TiO₂ spot 2 in Figure 5), and carbon modified TiO₂ samples display significant differences: (1) the splitting of the main Ti-O phonon (at 664 cm⁻¹) into two—one at 659 cm⁻¹ and another at 536 cm⁻¹ and (2) the emergence of new absorption peaks in the range from 1400 to 1600 cm⁻¹. The phonon splitting can be assigned to surface phonons due to small particle size whereas the new peaks in the range from 1400 to 1600 cm⁻¹ can be due to the presence of carbon in the particle as shown in the enlarged inset of Figure 5. There is no indication of the structure of the carbon dopant with the



(a)



(b)



(c)

FIGURE 4: HRTEM of the PSP C:TiO₂ QDs. Inset (a) is the FFT of the high-resolution image showing the reflection from the predominant (101) plane of the TiO₂ lattice from a number of particles in the high-resolution image and inset (b) is the fringe separation distribution histogram of the PSP C:TiO₂ QDs.

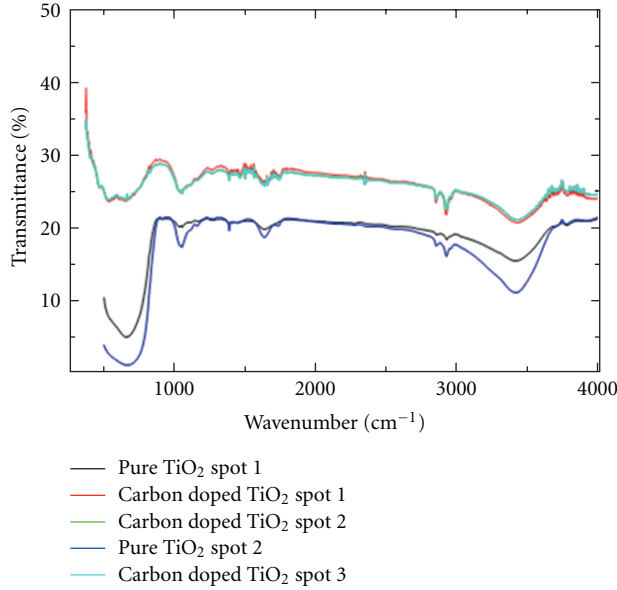
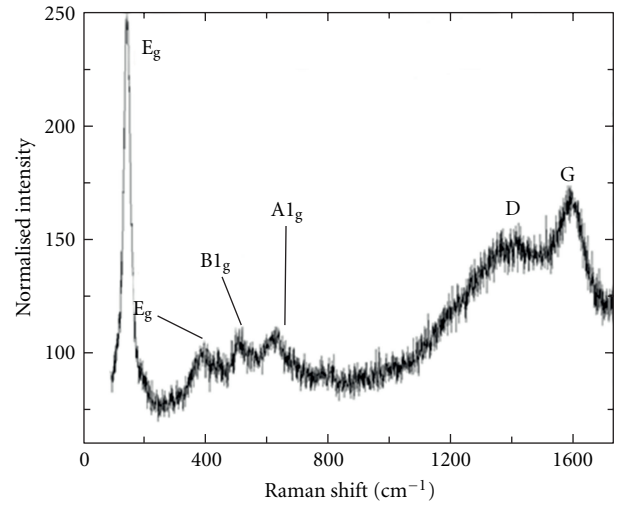


FIGURE 5: FTIR spectroscopy of pure TiO_2 compared with C:TiO₂ QDs synthesized by PSP technique.

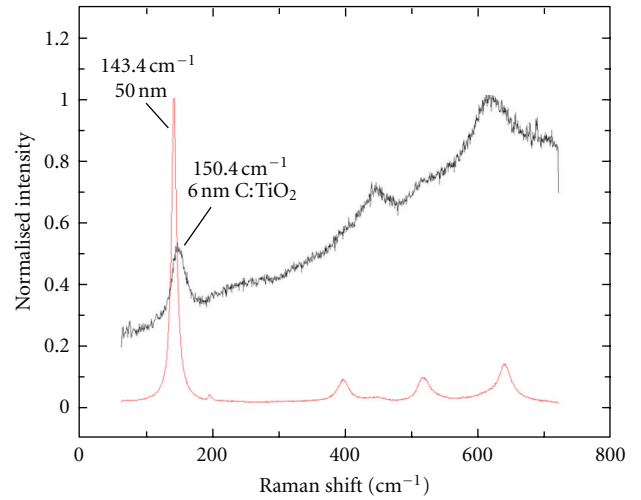
present FTIR spectra. However, these peaks are ably captured in Raman spectroscopy presented herein.

TiO_2 is known to exhibit six Raman active bands characteristic of anatase phase at 144, 197, 399, 515, 519, and 639 cm^{-1} with symmetries of E_g , E_g , B_{1g} , A_{1g} , B_{1g} , and E_g respectively [20–22]. However, it has been shown [23] that, when TiO_2 are coated with carbon as core-shell particles, the main E_g mode of 144 cm^{-1} blue shifts to $\sim 153\text{ cm}^{-1}$. This is what we see in our typical Raman spectrum for the PSP sample where this phonon mode has shifted to 152 cm^{-1} . Raman spectroscopy in this case suggests carbon doping in our samples. We have extended our RS to include the carbon bands as shown in Figure 6(a). We observed the D-band of the disordered carbon at 1354 cm^{-1} and the perfect graphite peak at 1583 cm^{-1} [23, 24]. This is a clear indication of the presence of carbon in these samples, which supports the HRTEM results in this work. Raman spectroscopy of the C:TiO₂ NPs also shows broadening and blue shift of the anatase E_g phonon lineshape (Figure 6(b)) when compared to bulk TiO_2 of mean size of 50 nm. This lineshape is also asymmetrical (Figure 6(c)) which is an indication that either there is optical phonon confinement or the inhomogeneous laser heating effects on the TiO_2 nanostructures [24, 25] or both.

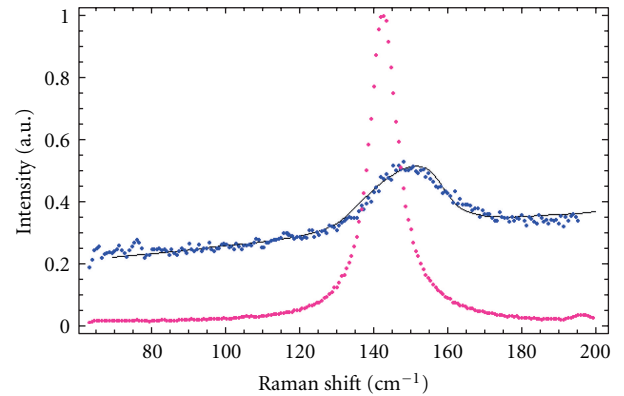
In order to pursue phonon confinement, it is important to lay a brief background. In the 1980s, it became apparent that Raman spectral line shapes for microcrystals could not follow the perfect Gaussian profile [26]. It was then realised that there was need for a deeper understanding of the origin of this asymmetry. Spatial correlation modelling, as it was called, then became one way to extract information from RS data. It was stated in our previous work [27] that the justification for this new behavior is that, for a perfect (bulk) crystal of diameter d having vibrational modes of momentum \mathbf{q} ,



(a)



(b)



(c)

FIGURE 6: Raman spectroscopy of the C:TiO₂ QDs synthesized by PSP technique showing (a) the presence of carbon D and G bands in the 6-nm QDs, (b) the major anatase peak at 153 cm^{-1} shifted from the pure bulk TiO_2 peak at 143 cm^{-1} , and (c) the present confinement model fitted to the 6-nm particles data.

the Heisenberg's uncertainty principle ($\delta d \cdot \delta \mathbf{q} \sim h$) means that as $\delta d \rightarrow \infty$ (bulk) then $\delta \mathbf{q} \rightarrow 0$ (the " $\mathbf{q} = 0$ " selection rule applies). As the diameter, $\delta d \rightarrow 0$ (nanometric) then the vibrational momentum, $\mathbf{q} \rightarrow \infty$. In this case, the " $\mathbf{q} = 0$ " selection rule breaks down; a contribution from the $\mathbf{q} \neq 0$ phonons determined by the dispersion relation $\omega \mathbf{q}$ is allowed [27]. This accounts for the asymmetric broadening of the peaks in a Raman spectrum. The Richter equation for confined phonons in spherical nanoparticles [26] was modified to include Gaussian distribution of the phonon momenta and particle size by Bhattacharyya and Samui [28] and given here as

$$I(\omega) = A_0 \int_{-\infty}^{\infty} \left[\frac{|C(0, \mathbf{q})|^2}{(\omega - \omega(\mathbf{q}))^2 + (\Gamma_0/2)^2} \right] d^3 \mathbf{q}, \quad (2)$$

In the equation, Γ_0 is the full-width-at-half-maximum (FWHM) for bulk material Raman peak (for instance $\Gamma_0 = 7.0 \text{ cm}^{-1}$ for bulk TiO_2 [29]), $\omega \mathbf{q}$ is the phonon dispersion curve relation (PDR) for the material (e.g. $A = 145 \text{ cm}^{-1}$, $a = 0.32 \text{ nm}$ for the 144 cm^{-1} phonon branch). The Richter et al. model is valid for spherical nanocrystals of mean diameter L for which the Fourier coefficient $C(0, \mathbf{q})$ was assumed to be Gaussian of the form $\exp(-\mathbf{q}^2 L^2/4\pi^2)$ with a phonon amplitude at the boundary of $1/e$. When geometry deviates from a sphere, then adjustment has to be carried out. And so, we fit the following equation to the 6 nm mean diameter nanoparticles:

$$I(\omega) = A_1 + m\omega + A_0 \int_{L_{\min}}^{L_{\max}} dL \times \rho(L) \int_{-\infty}^{\infty} \left[4\pi \mathbf{q}^2 \frac{\exp(\mathbf{q}^2 L^2/\alpha)}{(\omega - \omega_0 \pm B a \mathbf{q}^2)^2 + (\Gamma_0/2)^2} \right] d\mathbf{q}. \quad (3)$$

The fitting was performed by activating a "Statistics NonlinearFit" routine in Mathematica 4.1 and is presented graphically in Figure 6(c). From this fit, the following parameters are extracted $A_0 = 10^{-17}$, $\alpha = 3 \pi^2$ (~ 30), $\omega_0 = 150.4 \text{ cm}^{-1}$, $B = 0.005 \text{ cm}^{-2}$, and $\Gamma_0 = 20 \text{ cm}^{-1}$. Note that the value of 20 cm^{-1} for Γ_0 is 13 cm^{-1} above the value for bulk TiO_2 . Also the size distribution integral in (3) has been replaced by an expression $A_1 + m\omega = 0.25 + 0.008\omega$ to take into account the background noise inherent in the fluorescent nanostructures. These results show that the blue shift of the central Brillouin zone phonon frequency from 143.4 cm^{-1} for particles of mean diameter of 50 nm of pure TiO_2 to 150.4 cm^{-1} for particles of mean diameter of 6 nm is not only due to reduction of particle size but also could be due to the presence of carbon in the TiO_2 structure. We are yet to determine the singular contribution of carbon doping to this blue shift.

5. Optical Properties of the Carbon-Modified TiO_2

It is well known that pure TiO_2 can only absorb light below the wavelength of 387.5 nm because its bandgap is 3.2 eV.

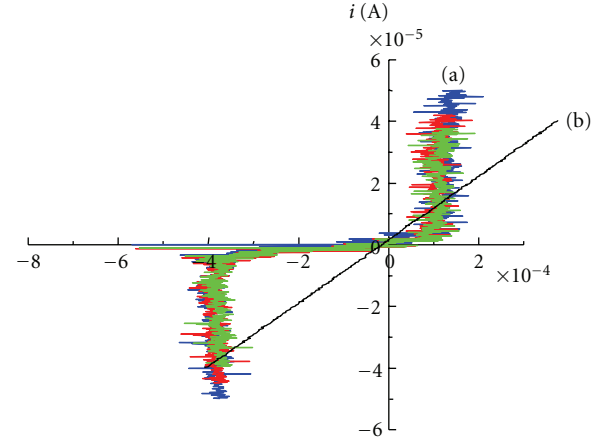


FIGURE 7: Current-Voltage characteristics for the transparent ohmic conductor F:SnO₂ on glass substrate (line (b)) showing ohmic behaviour and the C:TiO₂ QDs (curves (a)) showing semiconductor behaviour.

In order to extend the absorption region of TiO_2 to use the majority of the sunlight of the solar spectrum, doping of titanium dioxide with nonmetal, transition metals, and composite transition metal oxide has been employed [30–35]. Doping of TiO_2 inhibits recombination of photogenerated electrons and holes by increasing the charge separation and, therefore, enhances the efficiency of photon generation [30]. Carbon has been found to be a suitable dopant for TiO_2 , in applications that involve solar energy conversion. The presently carbon-doped TiO_2 samples showed a strong and broad absorption band around 637 nm in the UV-Vis-IR spectra (not shown). The solar emission spectrum ranges from 250 nm to 2500 nm. The shift in the absorption from below 387.5 nm (pure TiO_2) to 637 nm (C:TiO₂ NPs) is a positive indication that the C:TiO₂ samples will perform different in a solar cell.

6. Current-Voltage Output Characteristics of the Alloy

Figure 7 shows the I - V characteristics of the C:TiO₂ NPs. The four-point probe I - V curve characteristic of F:SnO₂ on the glass substrate is shown in Figure 7(b) with a voltage sweep from -0.4 mV to 0.4 mV . The I - V curve shows that there is a linear relationship between current and voltage where $I \sim \sigma \cdot V$ (σ being the conductance) and it also shows that the F:SnO₂ on the glass substrate is indeed a transparent ohmic conductor. Typical I - V characteristics of C:TiO₂ NPs deposited on FTO glass substrate are shown in Figure 6(a) with a current sweep in the range of $-60 \mu\text{A}$ to $+60 \mu\text{A}$. The measurements from different spots gave slightly different values, which is caused by inhomogeneous deposition of the nanoparticles onto the glass substrates during spray pyrolysis. However, there is a general similarity of the I - V curves for the different spots.

On all spots of the C:TiO₂ NPs film, the I - V curves clearly suggest that the NPs are semiconducting with a bandgap (E_g)

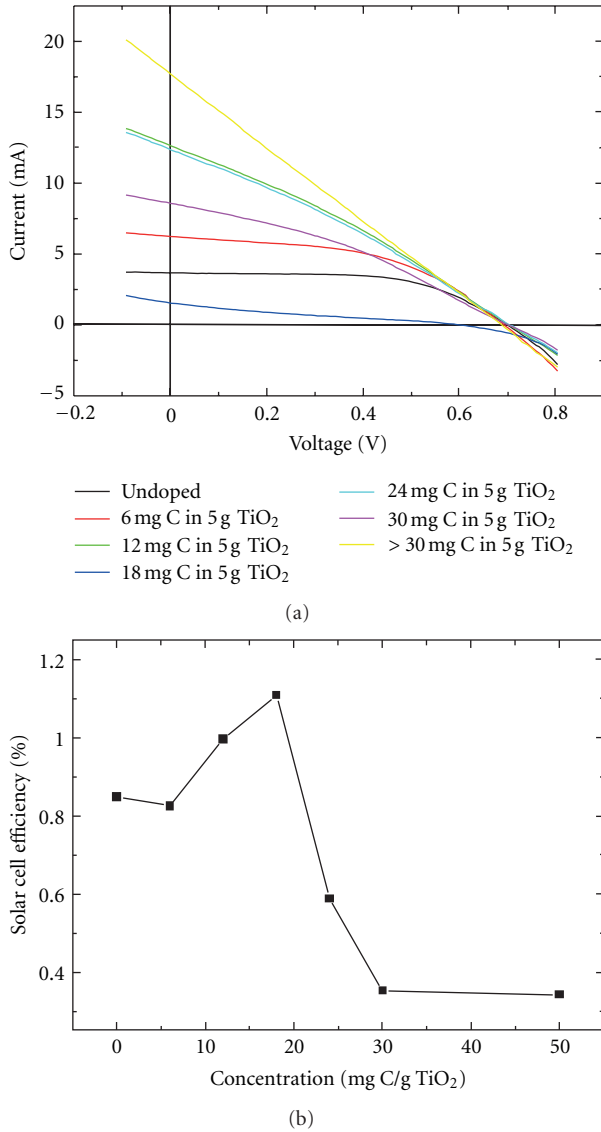


FIGURE 8: I-V characteristics of the typical dye sensitized solar cells containing varying mg of carbon in the TiO₂ as electrode (b) Efficiency of such solar cells as a function of carbon concentration.

determined from the width of the I - V curve when current is nearly zero. The bandgap here expressed in volts is found to be about 4×10^{-4} V. Extracalibration is required to convert this reading into electron volts (eV). This is beyond the scope of this paper. However, this value could be comparable to the band gap of TiO₂ of 3.2 eV found by other methods. The deviation of the E_g from 3.2 eV should be proportional to the amount of carbon doping and also particle size.

Also from the I - V curves one could speculate the type of conductivity one gets in the C:TiO₂ NPs. TiO₂ is naturally n -type semiconductor. Doping with carbon is expected to increase the electron density and make it more n -type.

The I - V characteristics in the $(-x, -y)$ quadrant of Figure 7 clearly indicates a negative slope which suggests “negative conductance.” This apparent negative conductance

could be due to the so-called Gunn effect which was discovered in III-V compounds such as GaAs and InP and reported by Gunn in 1963 [33]. Gunn saw that when an electric field reaches a threshold value in some materials the mobility of electrons decreases as the electric field is increased further, thereby producing negative resistance. Other authors such as Shikwambana et al. [36] and Mwakikunga et al. [37, 38] have reported S-shaped I - V curves in VO₂ which show negative conductance. At a critical current, a core of the low resistivity phase was seen to be formed and this was attributed to the falling of the voltage across the device while the current increased to a value dependent on a specific load line. With further increases in the circuit current, the voltage across the device was seen to decrease slightly. Also the role of doping on the negativity of the slope in the I - V curves have been reported in boron-doped diamond [38] pointing this phenomenon to the n -type conductivity of these type of diamonds.

Furthermore, by inspection, the I - V curves are not symmetrical about the $V = 0$ point but rather shifted to negative voltages such that if one fits some analytical function $i(V)$ such as Shockley’s diode equation among others and calculates the area under the I - V curves in the negative voltage and positive voltage sections, one can state that

$$\text{If } \int_{-V}^0 i(V)dV > \int_0^V i(V)dV \quad \text{then } n\text{-type} \\ \text{else } p\text{-type.} \quad (4)$$

The integral of $i(V)dV$ calculates the total electrical energy dissipated on charge carriers. The principle in (4) states that if more electrical energy is spent on driving the negative charge carriers in a semiconductor then such a material is intrinsically n -type and vice versa. From the curves in Figure 7, 20 nW are spent on electrons whereas only 5 nW are spent on the holes. We sufficiently concluded that our carbon-doped TiO₂ NPs are indeed n -type which is a necessary precursor for planned DSSC electrode.

7. TiO₂ Electrodes of Carbon-Dopant Concentration Used in the Dye-Sensitized Solar Cells

With the carbon doped TiO₂ electrode results, we continued to build dye-sensitized solar cells containing TiO₂ electrodes of varying carbon-dopant concentrations. This concentration is calculated from the amount of sucrose in mg for every litre of the total volume of the precursor material. The solar cell area was kept constant at 1.8 cm². The current-voltage characteristics of each individual cell are presented in Figure 8(a). Efficiency values were calculated from open-circuit voltage values and short-circuit current obtained from these current-voltage output characteristics. The efficiency values at varying carbon concentration are given in Figure 8(b). The current efficiency values (~ 0.3 – 1.1%) are admittedly much lower than those obtained for dye sensitized solar cells (~ 5 – 11%). This can be improved by employing more careful fabrication processes. However, the current results, at the laboratory scale, show that

carbon concentration does increase the efficiency of the dye-sensitized solar cell by about 1.5 times over the solar cell with pristine TiO₂ layer.

8. Conclusion

We have successfully synthesized C:TiO₂ NPs using ultrasonic nebulizer spray pyrolysis (USP) and pneumatic spray pyrolysis (PSP) techniques. These spherical nanoparticles have a modal particles size of 3.11 nm and 5.5 nm, respectively. The lattice fringe separations are 2.017 Å for USP and 3.74 Å for PSP. This suggests substitutional carbon doping for USP and a mixture of substitutional and interstitial carbon doping for PSP. In both processes, the TiO₂ structure changes with the most predominant reflection plane of (101) of the TiO₂ observed. The Raman active phonon of 141 cm⁻¹ from anatase is shifted to 150.4 cm⁻¹ due to both size effect and carbon doping in agreement with most previous findings. The carbon doping enhanced the TiO₂'s *n*-type conductivity with the *I*-*V* characteristics manifesting "negative conductance" especially when negative voltage is used. The *n*-type conductivity has also been confirmed by calculating areas under the *I*-*V* curves. The C:TiO₂ NPs produced in this study show properties that would not only make the materials suitable for photocatalytic activity, but also for electrodes in Grätzel-type of solar cells. Efficiency values for solar cells of varying carbon concentrations in their TiO₂ electrodes show up to 1.5 times improvement over the pure TiO₂ electrode-based solar cells.

Acknowledgments

Financial support from our sponsors, SANERI, ESKOM, and Govan Mbeki R&D Centre at the University of Fort Hare, is acknowledged. The authors are thankful for infrastructural support from Ithemba LABS (Gauteng,) and DST/CSIR National Centre for Nano-Structured Materials. Additional financial support from the India-Brazil-South Africa (IBSA) programme is also acknowledged.

References

- [1] "Reported timeline of solar cell energy conversion efficiencies," National Renewable Energy Laboratory (USA), [http://en.wikipedia.org/wiki/File:PVEff\(rev110707\)d.png](http://en.wikipedia.org/wiki/File:PVEff(rev110707)d.png).
- [2] M. Grätzel, "Molecular photovoltaics that mimic photosynthesis," *Pure and Applied Chemistry*, vol. 73, no. 3, pp. 459–467, 2001.
- [3] J. He, H. Lindström, A. Hagfeldt, and S. E. Lindquist, "Dye-sensitized nanostructured tandem cell-first demonstrated cell with a dye-sensitized photocathode," *Solar Energy Materials and Solar Cells*, vol. 62, no. 3, pp. 265–273, 2000.
- [4] J. Bandara and H. Weerasinghe, "Design of high-efficiency solid-state dye-sensitized solar cells using coupled dye mixtures," *Solar Energy Materials and Solar Cells*, vol. 90, no. 7-8, pp. 864–871, 2006.
- [5] K. T. Roro, B. Mwakikunga, N. Tile, B. Yalisi, and A. Forbes, "Effect of accelerated thermal ageing on the selective solar thermal harvesting properties of multiwall carbon nanotube/nickel oxide nanocomposite coatings," *International Journal of Photoenergy*, vol. 2012, Article ID 678394, 7 pages, 2012.
- [6] J. Chen, K. Li, Y. Luo et al., "A flexible carbon counter electrode for dye-sensitized solar cells," *Carbon*, vol. 47, no. 11, pp. 2704–2708, 2009.
- [7] G. Jiang, Z. Lin, L. Zhu, Y. Ding, and H. Tang, "Preparation and photoelectrocatalytic properties of titania/carbon nanotube composite films," *Carbon*, vol. 48, no. 12, pp. 3369–3375, 2010.
- [8] H. Wang, X. Quan, H. Yu, and S. Chen, "Fabrication of a TiO₂/carbon nanowall heterojunction and its photocatalytic ability," *Carbon*, vol. 46, no. 8, pp. 1126–1132, 2008.
- [9] R. Leary and A. Westwood, "Carbonaceous nanomaterials for the enhancement of TiO₂ photocatalysis," *Carbon*, vol. 49, no. 3, pp. 741–772, 2011.
- [10] J. Livage, "Vanadium pentoxide gels," *Chemistry of Materials*, vol. 3, no. 4, pp. 578–593, 1991.
- [11] B. W. Mwakikunga, A. Forbes, E. Sideras-Haddad, M. Scriba, and E. Manikandan, "Self assembly and properties of C:WO₃ nano-platelets and C:VO₂/V₂O₅ triangular capsules produced by laser solution photolysis," *Nanoscale Research Letters*, vol. 5, no. 2, pp. 389–397, 2010.
- [12] B. W. Mwakikunga, E. Sideras-Haddad, and M. Maaza, "First synthesis of vanadium dioxide by ultrasonic nebula-spray pyrolysis," *Optical Materials*, vol. 29, no. 5, pp. 481–487, 2007.
- [13] B. W. Mwakikunga, E. Sideras-Haddad, A. Forbes, and C. Arendse, "Raman spectroscopy of WO₃ nano-wires and thermo-chromism study of VO₂ belts produced by ultrasonic spray and laser pyrolysis techniques," *Physica Status Solidi*, vol. 205, no. 1, pp. 150–154, 2008.
- [14] B. W. Mwakikunga, E. Sideras-Haddad, C. Arendse, M. J. Witcomb, and A. Forbes, "WO₃ nano-spheres into W₁₈O₄₉ one-dimensional nano-structures through thermal annealing," *Journal of Nanoscience and Nanotechnology*, vol. 9, no. 5, pp. 3286–3294, 2009.
- [15] B. W. Mwakikunga, A. Forbes, E. Sideras-Haddad, and C. Arendse, "Optimization, yield studies and morphology of WO₃ nano-wires synthesized by laser pyrolysis in C₂H₂ and O₂ ambients-validation of a new growth mechanism," *Nanoscale Research Letters*, vol. 3, no. 10, pp. 372–380, 2008.
- [16] E. P. Meagher and G. A. Lager, "Polyhedral thermal expansion in the TiO₂ polymorphs: refinement of the crystal structures of rutile and brookite at high temperature," *The Canadian Mineralogist*, vol. 17, pp. 77–85, 1979.
- [17] D. Bersani, P. P. Lottici, and X.-Z. Ding, "Phonon confinement effects in the Raman scattering by TiO₂ nanocrystals," *Applied Physics Letters*, vol. 72, no. 1, p. 73, 1998.
- [18] D. Luca and L. S. Hsu, "Structural evolution and optical properties of TiO₂ thin films prepared by thermal oxidation of PLD Ti films," *Journal of Optoelectronics and Advanced Materials*, vol. 5, no. 4, pp. 835–840, 2003.
- [19] R. Suthyanoorthy, P. Sudhagar, S. Chadramohan, and K. P. Vijayakumar, "Photoelectrical properties of crystalline titanium dioxide thin films after thermo-annealing," *Crystal Research and Technology*, vol. 42, no. 5, pp. 498–503, 2007.
- [20] X. Hu, T. Zhanga, Z. Jina et al., "Fabrication of carbon-modified TiO₂ nanotube arrays and their photocatalytic activity," *Materials Letters*, vol. 62, no. 30, pp. 4579–4581, 2008.
- [21] G. Katumba, B. W. Mwakikunga, and T. R. Mothibinyane, "FTIR and Raman spectroscopy of carbon nanoparticles in SiO₂, ZnO and NiO matrices," *Nanoscale Research Letters*, vol. 3, no. 11, pp. 421–426, 2008.

- [22] S. Piscanec, M. Cantoro, A. C. Ferrari et al., "Raman spectroscopy of silicon nanowires," *Physical Review B*, vol. 68, no. 24, Article ID 241312, 4 pages, 2003.
- [23] H. Richter, Z. P. Wang, and L. Ley, "The one phonon Raman spectrum in microcrystalline silicon," *Solid State Communications*, vol. 39, no. 5, pp. 625–629, 1981.
- [24] I. H. Campbell and P. M. Fauchet, "The effects of microcrystal size and shape on the one phonon Raman spectra of crystalline semiconductors," *Solid State Communications*, vol. 58, no. 10, pp. 739–741, 1986.
- [25] K. R. Zhu, M. S. Zhang, Q. Chen, and Z. Yin, "Size and phonon-confinement effects on low-frequency Raman mode of anatase TiO₂ nanocrystal," *Physics Letters A*, vol. 340, no. 1–4, pp. 220–227, 2005.
- [26] D. Wang, J. Zhao, B. Chen, and C. Zhu, "Lattice vibration fundamentals in nanocrystalline anatase investigated with Raman scattering," *Journal of Physics: Condensed Matter*, vol. 20, no. 8, Article ID 085212, 2008.
- [27] C. Xu, Y. A. Shaban, W. B. Ingler, and S. U. M. Khan, "Nanotube enhanced photoresponse of carbon modified (CM)-n-TiO₂ for efficient water splitting," *Solar Energy Materials and Solar Cells*, vol. 91, no. 10, pp. 938–943, 2007.
- [28] S. Bhattacharyya and S. Samui, "Phonon confinement in oxide-coated silicon nanowires," *Applied Physics Letters*, vol. 84, no. 9, p. 1564, 2004.
- [29] Y. A. Shaban and S. U. M. Khan, "Surface grooved visible light active carbon modified (CM)-n-TiO₂ thin films for efficient photoelectrochemical splitting of water," *Chemical Physics*, vol. 339, no. 1–3, pp. 73–85, 2007.
- [30] V. Keller and F. Garin, "Photocatalytic behavior of a new composite ternary system: WO₃/SiC-TiO₂. Effect of the coupling of semiconductors and oxides in photocatalytic oxidation of methylethylketone in the gas phase," *Catalysis Communications*, vol. 4, no. 8, pp. 377–383, 2003.
- [31] V. Jokanovic, D. Janackovic, P. Spasic, and D. Uskokovic, "Modeling of nanostructural design of ultrafine mullite powder particles obtained by ultrasonic spray pyrolysis," *Nanostructured Materials*, vol. 12, no. 1, pp. 349–352, 1999.
- [32] P. G. Smetad and M. Graetzl, "Demonstrating electron transfer and nanotechnology: a natural dye-sensitized nanocrystalline energy converter," *Journal of Chemical Education*, vol. 75, no. 6, p. 752, 1999.
- [33] J. B. Gunn, "Microwave oscillations of current in III-V semiconductors," *Solid State Communications*, vol. 1, no. 4, pp. 88–91, 1963.
- [34] R. G. Cope and A. W. Penn, "High-speed solid-state thermal switches based on vanadium dioxide," *Journal of Physics D*, vol. 1, no. 2, pp. 161–168, 1968.
- [35] G. Stefanovich, A. Pergament, and D. Stefanovich, "Electrical switching and Mott transition in VO₂," *Journal of Physics Condensed Matter*, vol. 12, no. 41, pp. 8837–8845, 2000.
- [36] L. Shikwambana, M. Govender, B. Mwakikunga, E. Sideras-Haddad, and A. Forbes, "A review of the laser pyrolysis technique used to synthesize vanadium and tungsten oxide thin films," *Advanced Materials Research*, vol. 227, pp. 80–83, 2011.
- [37] B. W. Mwakikunga, A. E. Mudau, N. Brink, and C. J. Willers, "Flame temperature trends in reacting vanadium and tungsten ethoxide fluid sprays during CO₂-laser pyrolysis," *Applied Physics B*, vol. 105, pp. 451–462, 2011.
- [38] B. W. Mwakikunga, M. Maaza, K. T. Hillie, C. J. Arendse, T. Malwela, and E. Sideras-Haddad, "From phonon confinement to phonon splitting in flat nanostructures: a case of VO₂@V₂O₅ core-shell nanoribbons," *Vibrational Spectroscopy*, vol. 61, pp. 105–111, 2012.

Research Article

Influence of TiO₂ Nanocrystals Fabricating Dye-Sensitized Solar Cell on the Absorption Spectra of N719 Sensitizer

Puhong Wen, Yinfeng Han, and Weixing Zhao

Department of Chemistry and Chemical Engineering, Baoji University of Arts and Science, 1 Gaoxin Road, Shaanxi, Baoji 721013, China

Correspondence should be addressed to Puhong Wen, wenpuhong@gmail.com

Received 9 April 2012; Accepted 22 May 2012

Academic Editor: Mohamed Sabry Abdel-Mottaleb

Copyright © 2012 Puhong Wen et al. This is an open access article distributed under the Creative Commons Attribution License, which permits unrestricted use, distribution, and reproduction in any medium, provided the original work is properly cited.

The absorption spectra of N719 sensitizer anchored on the films prepared by TiO₂ nanocrystals with different morphology and size were investigated for improving the performance of dye-sensitized solar cell (DSC). We find that the morphology and size of TiO₂ nanocrystals can affect the UV-vis and FT-IR spectra of the sensitizer anchored on their surfaces. In particular, the low-energy metal-to-ligand charge-transfer transitions (MLCT) band in the visible absorption spectra of N719 is strongly affected, and locations of these MLCT bands revealed larger differences. The results indicate that there is a red shift of MLCT band in the spectra obtained by using TiO₂ nanocrystals with long morphology and large size compared to that in solution. And it produced a larger red-shift on the MLCT band after TiO₂ nanocrystals with small size mixed with some long nanocrystals. Accordingly, the utilization rate to visible light is increased. This is a reason why the DSC prepared by using such film as a photoelectrode has better performance than before mixing.

1. Introduction

As such a concept for photovoltaic devices, dye-sensitized solar cells (DSCs) have received considerable attention since 1991 due to their relatively high efficiency and low fabrication cost [1–6]. Ruthenium polypyridyl complexes are commonly used as dyes in DSCs, and the highest power conversion efficiency of 11.3% has been achieved [7]. The typical DSC consists of a dye-coated mesoporous TiO₂ nanoparticle film sandwiched between two transparent electrodes, and a liquid electrolyte, traditionally containing the tri-iodide/iodide redox couple, fills the pores of the film and contacts the nanoparticle. Many factors, in particular, in the part of the photoelectrode such as morphology, particle size, and crystal structure of semiconductor TiO₂ [8], can affect the performance of DSC. They should be investigated in order to raise power conversion efficacy. In the past decade, much work has been done to improve the photovoltaic parameters of DSC including optimizing nanostructured semiconductor electrodes [9, 10], sensitizers [11, 12], redox electrolytes [13, 14], and electric additives [15–17]. Only few studies, however, focused on the effect of the TiO₂

nanocrystals on the absorption spectra of the sensitizer anchored on their surfaces. Nazeeruddin et al. [18] reported merely the differences in the absorption spectra of sensitizer N3, N719, and N712 anchored on TiO₂ nanocrystals. In this study, the absorption spectra of sensitizer N719 anchored on TiO₂ nanocrystals with different morphology and particle size were investigated for increasing the utilization rate to visible light. The result is helpful to improve the performances of DSCs.

2. Experimental Details

2.1. Materials. 10 wt% tetrabutylammonium hydroxide (TBAOH) aqueous solution and *n*-propylamine (PA) solution were purchased from Tokyo chemicals. N719 (*cis*-di(thiocyanate)bis(2,2'-bipyridyl-4,4'-dicarboxylate)-ruthenium(II) bis-tetrabutyl-ammonium) was purchased from Sigma-Aldrich. ST01 (commercial TiO₂ powder) was obtained from Ishihara. ST111 (commercial TiO₂ powder) was obtained from Titan Kogyo. Other chemicals and reagents were of analytical grade, and all the reagents were used as received without further purification.

2.2. Synthesis of TiO_2 Nanocrystals. To prepare anatase samples QTBA, QPA, and LPA, an H^+ -form-layered titanate ($\text{H}_{1.07}\text{Ti}_{1.73}\text{O}_4$) with lepidocrocite-like structure was treated in a TBAOH solution or a PA solution to exfoliate the layered titanate into its nanosheets. The titanate nanosheet solution was then reacted under hydrothermal conditions [19, 20]. The QTBA was obtained by hydrothermal reaction of a titanate nanosheet solution of TBAOH at 120°C and pH 1.8. The samples QPA and LPA were obtained by hydrothermal reaction of a titanate nanosheet solution of PA at 120°C and pH 1.9, and at 135°C and pH 11.3, respectively.

2.3. Fabrication of Dye-Sensitized Solar Cell. A TiO_2 film electrode was prepared by the doctor-blade technique, using TiO_2 nanocrystal paste on an FTO glass plate (25×25 mm). The paste sample was prepared by dispersing TiO_2 nanocrystals sample in a 0.2 mol/L HNO_3 solution containing 3 wt% of Triton X-100, 5 wt% of acetylacetone, and 10 wt% of polyethylene glycol (PEG) (molecular weight of 20,000). The TiO_2 content in the paste was adjusted to about 15–18 wt% to control the thickness of the TiO_2 film. After being coated with the paste on the FTO glass plate, the TiO_2 film electrode was calcined at 450°C for 30 min and then immersed into a 3×10^{-4} mol/L N719 dye solution in a mixed solvent of acetonitrile and *tert*-butyl alcohol (1:1 volume ratio) for 24 h to adsorb the dye onto the TiO_2 electrode. The DSC was comprised of the dye-adsorbed TiO_2 electrode and a Pt-coated conducting glass counter-electrode, with an electrolyte solution between the electrodes. The electrolyte solution contained butylmethylimidazolium iodide (0.60 mol/L), I_2 (0.03 mol/L), guanidinium thiocyanate (0.10 mol/L), and 4-*tert*-butylpyridine (0.50 mol/L) in a mixed solvent of acetonitrile and valeronitrile (85%:15% volume ratio).

2.4. Photovoltaic Measurements. The photocurrent-voltage characteristic curves for the DSCs were measured using a Hokuto-Denko BAS100B electrochemical analyzer under irradiation with simulated sunlight of AM 1.5 (100 mW/cm²), using a sunlight simulator (YSS-E40, Yamashita Denso) and a 0.25 cm² mask. The thicknesses of the TiO_2 films were measured using a SURFCOM 480A surface-shape determiner.

2.5. Physical Analysis. Powder X-ray diffraction (XRD) analysis of the samples was carried out on a SHIMADZU XRD-6100 X-ray diffractometer with $\text{Cu K}\alpha$ ($\lambda = 0.15418$ nm) radiation for the investigation of the crystal structure of the samples. The size and morphology of the particles were observed using field-emission scanning electron microscopy (FE-SEM) (Hitachi, Model S-900). Transmission electron microscopy (TEM) observation and selected-area electron diffraction (SAED) were performed on a JEOL Model JEM-3010 system at 300 kV, and the powder sample was supported on a microgrid. Nitrogen gas adsorption was carried out on a Quantachrome Autosorb-1-MP apparatus. The specific surface area was calculated from the adsorption data using the Brunauer-Emmett-Teller (BET) method. FT-IR spectra of the samples were measured on a Perkin Elmer Spectrum One spectrophotometer at a resolution of better than 2 cm^{-1} .

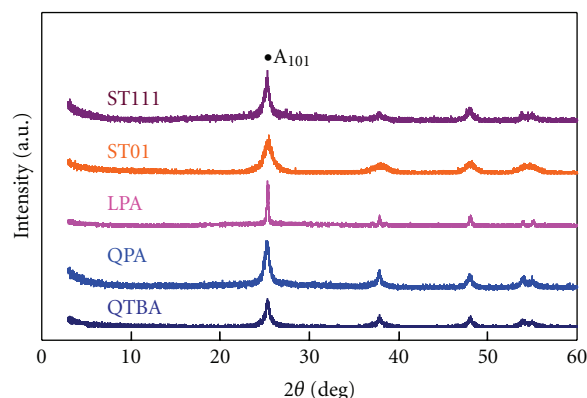


FIGURE 1: XRD patterns of the self-prepared (QTBA, QPA, and LPA) and the commercial (ST01 and ST111) TiO_2 nanocrystal samples. These samples are single phase of anatase. The width of diffraction peaks indicates the crystallinity increasing order of ST01 < ST111 < QTBA < QPA < LPA.

using the KBr technique. UV-visible spectra were recorded on a SHIMADZU UV-2450 spectrophotometer. A corresponding blank TiO_2 film was used as reference to obtain the UV-visible spectrum of the dye adsorbed on the TiO_2 film. Both have the same thickness.

3. Results and Discussion

3.1. Characterizations of TiO_2 Nanocrystals. To investigate the influences of the morphology and size of TiO_2 nanocrystals on the UV-vis and FT-IR spectra of the sensitizer anchored on their surfaces, five kinds of TiO_2 nanocrystal samples with different crystal sizes and crystal morphologies were used in this study. Two are typical commercial TiO_2 nanocrystal samples, ST01 and ST111, with different crystal sizes. And the rest are three self-prepared anatase nanocrystal samples with different crystal morphologies and sizes: QTBA, QPA, and LPA. They were prepared from exfoliated layered titanate ($\text{H}_{1.07}\text{Ti}_{1.73}\text{O}_4$) nanosheet solutions by hydrothermal reactions [19–21]. An XRD study indicated that they are single phase of anatase as shown in Figure 1. The width and acutance of diffraction peaks indicate the crystallinity increasing order of ST01 < ST111 < QTBA < QPA < LPA.

The TEM images of these TiO_2 nanocrystals are presented in Figure 2. The QTBA and QPA samples have quadrate crystal morphologies, but the size of the later is as large again as QTBA size of about 20 nm in width. The LPA sample has long nanoleaf-like crystal morphologies and larger size of about 30 nm in width and 300 nm in length. The SAED result indicated that QPA is a single crystal of anatase phase, which agrees with the XRD result in Figure 1.

The change in morphology can be explained by the effect of pH value on the dissolution reaction in the synthesis process [19]. The dissolution reactions along the (100), (001), and (101) planes of anatase phase can occur and cut the sheetlike particles into the quadrate anatase nanocrystals because of the acidic conditions (pH < 2) in the synthesis

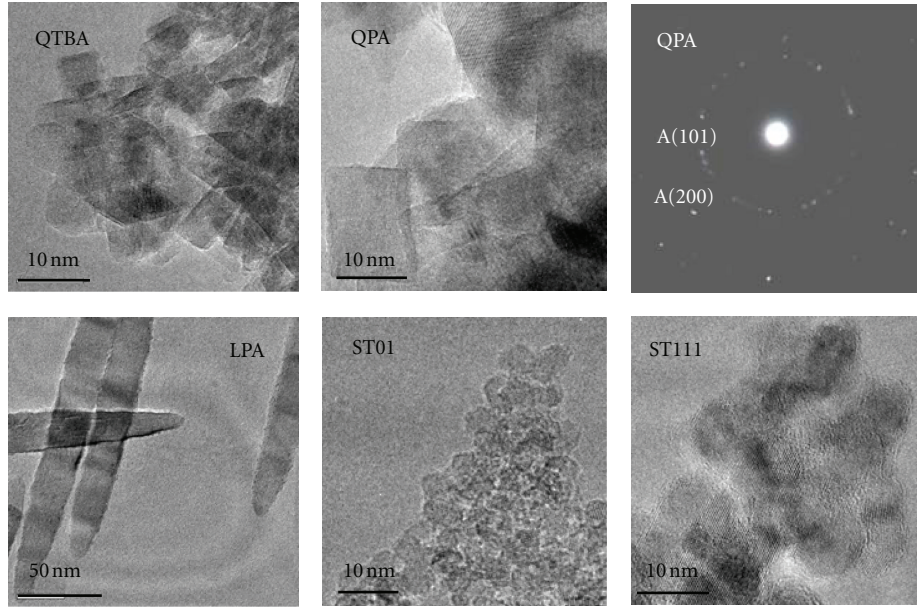


FIGURE 2: TEM images of the self-prepared (QTBA, QPA, and LPA) and the commercial (ST01 and ST111) TiO_2 nanocrystal samples and the SAED patterns of QPA sample.

TABLE 1: Morphology and surface area of the TiO_2 nanocrystals and the optical data of the N719 dye adsorbed onto TiO_2 nanocrystals films.

Sample	Morphology	S_{BET} (m^2/g)	UV-vis abs. λ_{max} (nm) ^b		FT-IR vibration band wavenumber (cm^{-1}) ^c
			MLCT	$\pi-\pi^*$	
ST01	Spherical	349	398sh 523		2105m 1657vs 1608vs 1541m 1467w 1430w 1403w 1373vs 1262vw 1235w 1165w 1107vw
ST111	Spherical	312	398sh 537		2105s 1657vs 1608vs 1542m 1466vw 1429m 1402w 1372vs 1261vw 1236w 1166m 1109vw
QTBA	Quadrate	131	395sh		2103w 1657vs 1607vs 1540m 1467w 1429w 1402w 1372vs 1262vw 1236w 1167w 1108vw
QPA	Quadrate	66	536		2104w 1713vw 1614vs 1544m 1466vw 1430m 1403m 1384vs 1262w 1231vw 1112w
LPA	Leaflike	35	598		2925s 2855m 2343w 2104m 1741m 1619s 1542m 1466w 1436w 1402m 1379s 1234m 1165w 1108w
QTBA-LPA			631		
QPA-LPA			571		
N719 ^a			390 531	215 253sh 313	2964s 2876w 2104vs 1714s 1611s 1543m 1467m 1437vw 1406m 1370s 1237s 1149vw 1021w

^a UV-vis absorption measured in ethanol, ^bsh: shoulder, ^cvs: very strong; s: strong; m: medium; w: weak; vw: very weak.

processes of QTBA and QPA samples, and the dissolution reaction only along the (100) plane can occur and cut the sheetlike particles into long nanoleaf-like anatase nanocrystals because the value of pH is 11.3 in the synthesis process of LPA sample. The ST01 and ST111 samples have spherical crystal morphologies with sizes of about 7 nm (ST01) and 10 nm (ST111), respectively. Figure 3 shows FE-SEM images of the single crystal of QTBA and LPA and the films prepared by using the corresponding single crystal. The results agree with TEM analysis and further indicate that the single crystals of QTBA and LPA are flat particles. The BET (Brunauer-Emmett-Teller) specific surface areas (S_{BET}) of the

TiO_2 nanoparticles samples are shown in Table 1. The S_{BET} values increase in the order of $\text{LPA} < \text{QPA} < \text{QTBA} < \text{ST111} < \text{ST01}$, which are in agreement with their crystal sizes.

3.2. Absorption Spectra Properties. The UV-vis and FT-IR absorption spectra properties of the N719 sensitizer anchored on the surfaces of TiO_2 nanocrystals ST01, ST111, QTBA, QPA, and LPA samples are shown in Table 1. The data about UV-vis absorption spectra of the N719 sample in ethanol solution and FT-IR absorption spectra of solid N719 sample are given in Table 1 for the comparison. The UV-vis absorption spectra of the N719 sample in ethanol

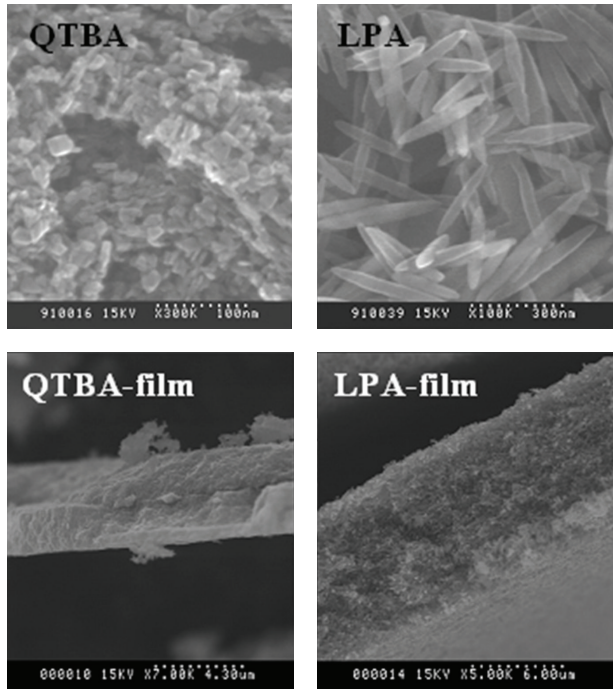


FIGURE 3: FE-SEM images of anatase TiO_2 nanocrystals QTBA and LPA samples and the films prepared by QTBA and LPA samples.

solution reveals four broad bands as shown in Figure 4(a). The two broad visible bands at 531 and 390 nm are assigned to metal-to-ligand charge-transfer (MLCT) origin. The bands in the UV region at 313 and 215 nm with a shoulder at 253 nm are specified to intraligand ($\pi-\pi^*$) charge-transfer transitions. Figure 4(b) shows a comparison of the absorption spectra of N719 dye adsorbed onto the films (6 to 10 μm thick) prepared by TiO_2 nanocrystals samples with different morphologies and sizes, and UV-vis absorption spectra of corresponding blank films without absorption band in the visible region are shown in Figure 4(c) for comparison. The low-energy MLCT maximum in N719 dye is considerably shifted upon adsorption onto these films compared to the solution spectra. The blue shifts of the low-energy MLCT band occur onto ST01 (8 nm) and QTBA (14 nm) films. On the other hand, the red shifts of the low-energy MLCT band occur to LPA (67 nm), ST111 (6 nm), and QPA (5 nm) films, and the film prepared by mixing QTBA (80%) and LPA (20%), which induces the largest red shift from 531 to 631 nm. The results reveal that there is a red shift of MLCT band in the spectra obtained by using TiO_2 nanocrystals with long morphology and large size compared to that in solution. And a larger red shift occurs on the MLCT band after TiO_2 nanocrystals with small size mixed with some long nanocrystals. Accordingly, it increases the utilization rate to visible light. The results indicate that the morphology and size of TiO_2 nanocrystals can lead to a shift in the low-energy MLCT of N719 dye. The shift is due to the change in the energy of the lowest unoccupied molecular orbital (LUMO) of the ligand, causing the $\pi-\pi^*$ and $d\pi-\pi^*$ transitions to occur at higher or lower energies [18].

The data about the FT-IR absorption spectra of solid N719 sample in Table 1 show the characteristic band at 2104 cm^{-1} due to the $\nu(\text{NCS})$ group. The bands at 1714 and 1237 cm^{-1} are assigned to the $\nu(\text{C=O})$, and $\nu(\text{C-O})$ groups, respectively. The other two strong bands at 1611 ($-\text{COO}^-_{\text{as}}$) and 1370 ($-\text{COO}^-_{\text{s}}$) cm^{-1} are assigned to the asymmetric and the symmetric stretch of the carboxylate group, respectively. The bands at 1611 , 1543 , and 1406 cm^{-1} are assigned to the bipyridyl $\nu(\text{C=C})$ absorption. The band at 1467 cm^{-1} is assigned to the $\delta(\text{CH}_2)$ of the Bu_4N^+ cations. The bands at 2876 and 2964 cm^{-1} are assigned to $\nu(\text{C-H})$ of tetrabutylammonium symmetric and asymmetric $-\text{CH}_2$ and $-\text{CH}_3$ groups, respectively [22]. To achieve high quantum yields of the excited state electron transfer process, the dye ideally needs to be in intimate contact with the semiconductor surface. The carboxylate functional groups of the dye serve as grafting agents for the oxide surface of the TiO_2 films. It is an important feature in a dye-sensitized solar cell for electronic communication between the complex and the substrate. The ruthenium complex N719 contains two carboxylic acid and two carboxylate groups. Thus, it can anchor onto the TiO_2 surface by a close overlap of the ligand π^* orbitals and the titanium 3D orbitals. A comparison of FT-IR absorption spectra properties of N719 sensitizer anchored on the surfaces of the TiO_2 nanocrystals ST01, ST111, QTBA, QPA, and LPA samples is shown in Figure 5. The major difference between the solid and the adsorbed N719 spectra occurs in carboxylic acid and carboxylate group bands. The $\nu(-\text{COO}^-_{\text{s}})$ bands in all adsorbed N719 samples are shifted to higher energy compared to the carboxylate group band (1370 cm^{-1}) of N719 complex. The shifts increase in the order of ST111 = QTBA (2 cm^{-1}) < ST01 (3 cm^{-1}) < LPA (9 cm^{-1}) < QPA (14 cm^{-1}). The $\nu(-\text{COO}^-_{\text{as}})$ band at 1611 cm^{-1} also occurs in the shifts, which is to lower energy for ST01 (3 cm^{-1}), ST111 (3 cm^{-1}) and QTBA (4 cm^{-1}), but higher energy for QPA (3 cm^{-1}) and LPA (8 cm^{-1}). The $\nu(\text{C-O})$ bands in all adsorbed N719 samples are shifted to lower energy compared to that (1237 cm^{-1}) in N719 complex. The increasing shift order of ST111 = QTBA (1 cm^{-1}) < ST01 (2 cm^{-1}) < LPA (3 cm^{-1}) < QPA (6 cm^{-1}) agrees with that of the $\nu(-\text{COO}^-_{\text{s}})$ bands. The $\nu(\text{C=O})$ band is shifted to lower energy by 57 cm^{-1} , from 1714 to 1657 cm^{-1} for ST01, ST111, and QTBA, and that in QPA is shifted only 1 cm^{-1} , but the band in LPA is at 1741 cm^{-1} shifting to higher energy (27 cm^{-1}). The $\nu(\text{NCS})$ group, the bipyridyl $\nu(\text{C=C})$ at 1543 and 1406 cm^{-1} , and the $\delta(\text{CH}_2)$ of the Bu_4N^+ cations bands are shifted hardly with the change of the morphology and the size of TiO_2 nanocrystals. The results indicated that the morphology and size of TiO_2 nanocrystals strongly affect on the $\nu(-\text{COO}^-_{\text{as}})$, $\nu(-\text{COO}^-_{\text{s}})$, $\nu(\text{C=O})$ and $\nu(\text{C-O})$ bands. A primary reason is that the morphology and size of TiO_2 nanocrystals can affect the energy level binding mode between the N719 and the TiO_2 . Therefore, the vibration bands of carboxylic acid and carboxylate groups used in grafting the N719 onto TiO_2 nanocrystals with different morphology and size reveal the obvious differences. Besides, $\nu(\text{C-H})$ bands of tetrabutylammonium symmetric and asymmetric $-\text{CH}_2$ and $-\text{CH}_3$ groups of the N719 anchoring onto the TiO_2

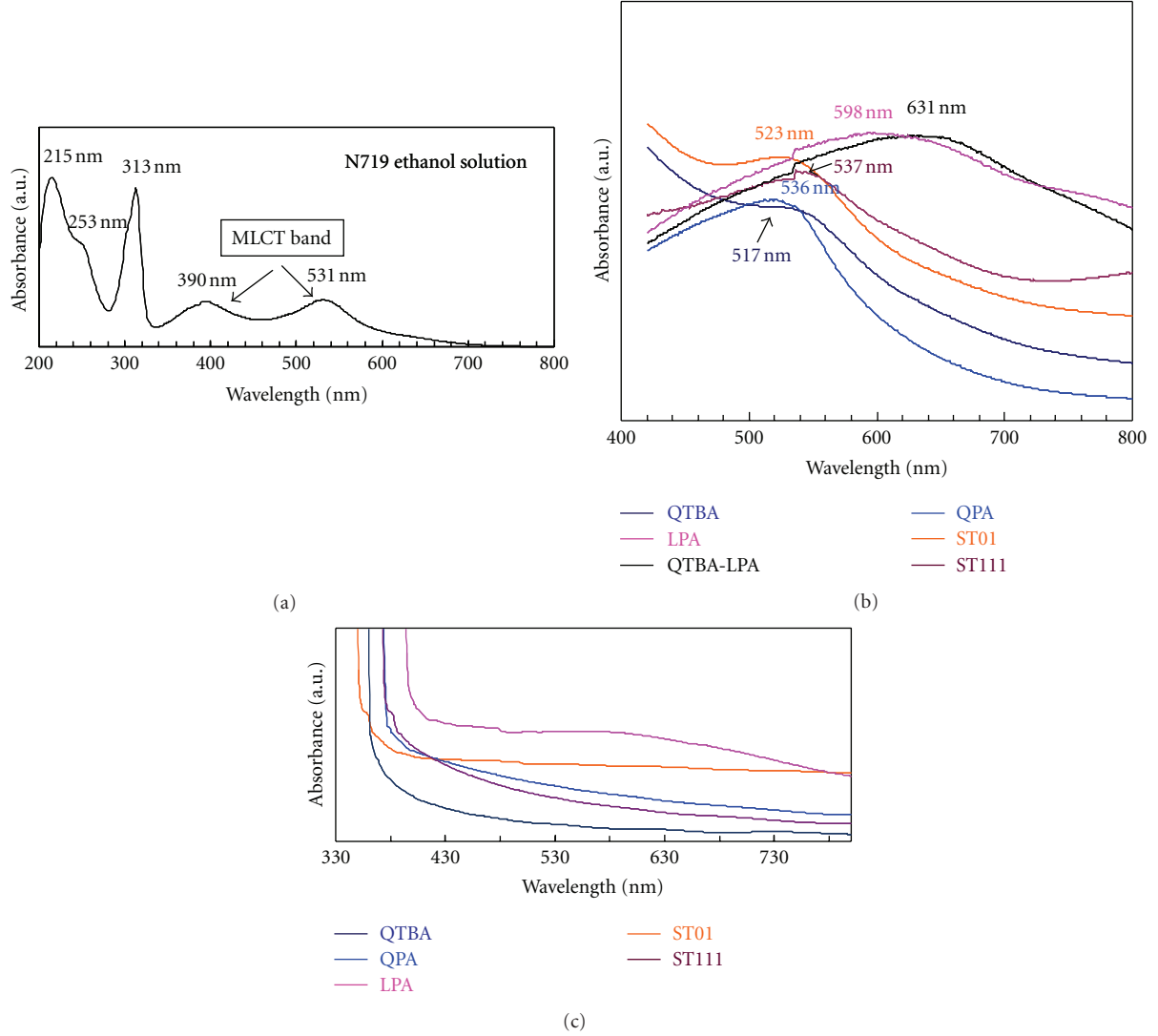


FIGURE 4: Absorption spectra of N719 dye in ethanol solution (a) and adsorbed onto TiO₂ nanocrystal films (b). Absorption spectra of the TiO₂ nanocrystals film samples (c).

surface also reveal larger differences with the change of the morphology and the size of TiO₂ nanocrystals due to steric reasons.

3.3. Photovoltaic Properties. Typical current-voltage characteristic curves (thin line) for ST01-based, ST111-based, QTBA-based, QPA-based, and LPA-based DSCs are presented in Figure 6. The power conversion efficiency (η) of the cell can be evaluated from the short circuit photocurrent density (J_{sc}), the open circuit potential (V_{oc}), the fill factor (ff) of the cell, and the intensity of the incident light ($I_s = 100 \text{ mW/cm}^2$) using the equation $\eta = J_{sc} V_{oc} ff / I_s$. Photovoltaic parameters of J_{sc} , V_{oc} , ff , and η for the DSCs prepared by using the above TiO₂ nanocrystals with different morphology and size are summarized in Table 2. These cell parameters are evaluated from the current-voltage curves of the DSCs in Figure 6. We observe that the V_{oc} value increases in the order of ST01 < QPA <

QTBA < LPA, and the J_{sc} value increases in the order of LPA < ST01 < QPA < QTBA. It is also observed that QPA sample has the lowest ff and η values, and LPA sample has the highest ff and η values. The QTBA sample with the highest J_{sc} value has lower η value due to the lower ff value. One of the important factors is the conductivity of the TiO₂ film. It has been reported that increasing the conductivity of TiO₂ film by adding one-dimensional nanowire-like particles into the spherical nanoparticles can enhance the ff value [23, 24].

In order to improve the performance of the DSCs prepared by single TiO₂ nanocrystals samples, QTBA, QPA, and ST01 samples (80%) were mixed with the long leaflike LPA(20%), respectively. The photocurrent-voltage characteristic curves (thick line) of DSCs prepared respectively using the QTBA-LPA, QPA-LPA, and ST01-LPA mixed samples are shown in Figure 6. The cell parameters of V_{oc} , J_{sc} , ff , and η for corresponding DSCs are summarized in Table 2. The cell parameters of V_{oc} , J_{sc} , ff , and η for the DSC

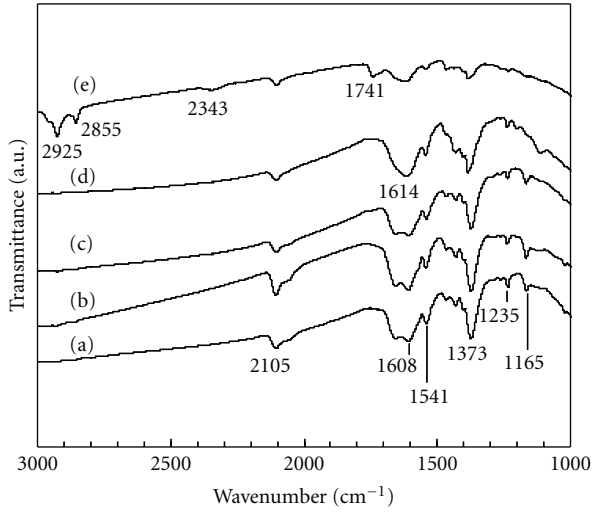


FIGURE 5: FT-IR spectra of the TiO_2 nanocrystals samples adsorbed by N719 dye. (a) N719-ST01; (b) N719-ST111; (c) N719-QTBA; (d) N719-QPA; (e) N719-LPA.

TABLE 2: Photovoltaic parameters of DSCs fabricated using the TiO_2 nanocrystals and thickness of the TiO_2 nanocrystals films.

Sample	V_{oc} (V)	J_{sc} (mA/cm ²)	ff	η (%)	Thickness (μm)
ST01	0.612	14.5	0.49	4.36	10.3
QTBA	0.637	19.9	0.43	5.40	5.8
QPA	0.630	16.9	0.38	4.07	10.6
LPA	0.717	13.2	0.61	5.77	8.8
ST01-LPA	0.659	19.2	0.51	6.45	19.6
QTBA-LPA	0.685	20.6	0.55	7.74	7.8
QPA-LPA	0.612	18.5	0.45	5.11	10.1

enhance 8%, 4%, 28%, and 43%, respectively, comparing with that for original QTBA-based DSC. And the η value (7.74%) is also much higher than that of P25-based DSC (6.3%) [25]. The η and J_{sc} values of the DSCs enhance 26% and 9% for QPA-LPA, and 48% and 32% for ST01-LPA, respectively, comparing with that for corresponding original DSC. The results reveal that the performance of the DSCs is significantly improved. The main reasons enhanced cell parameters are that the addition of the one-dimensional leaflike particles can effectively increase the conductivity for transferring the photoelectrons from the TiO_2 film to FTO glass surface that decreases the recombination loss of injected electrons in TiO_2 film [26], and the relatively larger particle size of LPA also causes the light-trapping effect that enhances the J_{sc} [27]. The other reason of the improved cell parameters is that the added LPA with the long leaf-like morphology and larger size brings the larger red shifts of MLCT band of the N719 dye onto the TiO_2 nanocrystals films. The J_{sc} value (mA/cm²) increases from 19.9 for QTBA to 20.6 for QTBA-LPA with the red shift of λ_{max} of the MLCT band from 517 to 631 nm. This red shift can expand the absorption region of visible light and thus increases the utilization rate to visible

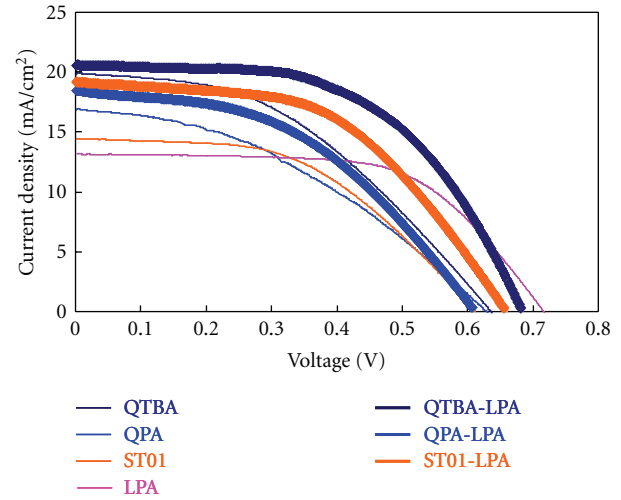


FIGURE 6: Current-Voltage characteristics for DSCs prepared using TiO_2 nanocrystals samples.

light. Therefore, this would enhance J_{sc} and η values of the DSCs as well.

4. Conclusions

The morphology and the size of TiO_2 nanocrystals can affect on the UV-vis and FT-IR spectra of the sensitizer anchored on their surfaces. In particular, the low-energy metal-to-ligand charge-transfer transitions band in the visible absorption spectra is shifted after dye N719 adsorbed onto TiO_2 nanocrystals. The maximum wavelength of low-energy MLCT bands increases in the order of quadrate < spherical < long crystal. The wavelength increases with the particle size as well. The results indicate that there is a red shift of MLCT band in the spectra obtained by using TiO_2 nanocrystals with long morphology and large size compared to that of N719 in solution. And a larger red shift of the MLCT band arises after TiO_2 nanocrystals with small size mixed with some long nanocrystals, which increases the utilization rate to visible light. This is a reason that the DSC prepared by using such film has better performance than that of before mixing. The morphology and the size of TiO_2 nanocrystals affect strongly on the $\nu(-\text{COO}^-_{as})$, $\nu(-\text{COO}^-_s)$, $\nu(\text{C}=\text{O})$, and $\nu(\text{C}-\text{O})$ bands. The main reason is that the morphology and the size of TiO_2 nanocrystals can affect the energy level binding mode between the N719 and the TiO_2 . Therefore, the vibration bands of carboxylic acid and carboxylate groups used in grafting the N719 onto TiO_2 nanocrystals with different morphology and size reveal the obvious differences.

Acknowledgments

This work was supported by the Natural Science Foundation of China (no. 21173003), the Scientific Research Project from Science and Technology Department of Shaanxi Province (no. 2011JM2009), and the Key Research Project from Baoji University of Arts and Sciences (no. ZK1051).

References

- [1] B. O'Regan and M. Grätzel, "A low-cost, high-efficiency solar cell based on dye-sensitized colloidal TiO₂ films," *Nature*, vol. 353, no. 6346, pp. 737–740, 1991.
- [2] K. Sayama, H. Sugihara, and H. Arakawa, "Photoelectrochemical properties of a porous Nb₂O₅ electrode sensitized by a ruthenium dye," *Chemistry of Materials*, vol. 10, no. 12, pp. 3825–3832, 1998.
- [3] S. Nakade, M. Matsuda, S. Kambe et al., "Dependence of TiO₂ nanoparticle preparation methods and annealing temperature on the efficiency of dye-sensitized solar cells," *Journal of Physical Chemistry B*, vol. 106, no. 39, pp. 10004–10010, 2002.
- [4] M. K. Nazeeruddin, F. De Angelis, S. Fantacci et al., "Combined experimental and DFT-TDDFT computational study of photoelectrochemical cell ruthenium sensitizers," *Journal of the American Chemical Society*, vol. 127, no. 48, pp. 16835–16847, 2005.
- [5] Y. Chiba, A. Islam, Y. Watanabe, R. Komiya, N. Koide, and L. Han, "Dye-sensitized solar cells with conversion efficiency of 11.1%," *Japanese Journal of Applied Physics*, vol. 45, no. 24–28, pp. L638–L640, 2006.
- [6] P. Wen, Z. Tao, Y. Ishikawa, H. Itoh, and Q. Feng, "Dye-sensitized solar cells based on anatase TiO₂ nanocrystals exposing a specific lattice plane on the surface," *Applied Physics Letters*, vol. 97, no. 13, Article ID 131906, 2010.
- [7] F. Gao, Y. Wang, D. Shi et al., "Enhance the optical absorptivity of nanocrystalline TiO₂ film with high molar extinction coefficient ruthenium sensitizers for high performance dye-sensitized solar cells," *Journal of the American Chemical Society*, vol. 130, no. 32, pp. 10720–10728, 2008.
- [8] S. K. Deb, "Dye-sensitized TiO₂ thin-film solar cell research at the national renewable energy laboratory (NREL)," *Solar Energy Materials and Solar Cells*, vol. 88, no. 1, pp. 1–10, 2005.
- [9] M. Murayama, N. Nishikawa, E. Yamazaki, M. Shoyama, N. Hashimoto, and K. Masuyama, "Nano-porous TiO₂ thin film for dye-sensitized solar cell," *Transactions of the Materials Research Society of Japan*, vol. 29, no. 4, pp. 1451–1454, 2004.
- [10] T. Horiuchi, H. Miura, K. Sumioka, and S. Uchida, "High efficiency of dye-sensitized solar cells based on metal-free indoline dyes," *Journal of the American Chemical Society*, vol. 126, no. 39, pp. 12218–12219, 2004.
- [11] H. Qin, S. Wenger, M. Xu et al., "An organic sensitizer with a fused dithienothiophene unit for efficient and stable dye-sensitized solar cells," *Journal of the American Chemical Society*, vol. 130, no. 29, pp. 9202–9203, 2008.
- [12] J. Song, F. Zhang, C. Li et al., "Phenylethyne-bridged dyes for dye-sensitized solar cells," *Journal of Physical Chemistry C*, vol. 113, no. 30, pp. 13391–13397, 2009.
- [13] P. Wang, S. M. Zakeeruddin, J. E. Moser, R. Humphry-Baker, and M. Grätzel, "A solvent-free, SeCN[−]/(SeCN)₃[−] based ionic liquid electrolyte for high-efficiency dye-sensitized nanocrystalline solar cells," *Journal of the American Chemical Society*, vol. 126, no. 23, pp. 7164–7165, 2004.
- [14] A. Hauch and A. Georg, "Diffusion in the electrolyte and charge-transfer reaction at the platinum electrode in dye-sensitized solar cells," *Electrochimica Acta*, vol. 46, no. 22, pp. 3457–3466, 2001.
- [15] M. Dürr, A. Yasuda, and G. Nelles, "On the origin of increased open circuit voltage of dye-sensitized solar cells using 4-ferf-butyl pyridine as additive to the electrolyte," *Applied Physics Letters*, vol. 89, no. 6, Article ID 061110, 2006.
- [16] H. Kusama, M. Kurashige, and H. Arakawa, "Influence of nitrogen-containing heterocyclic additives in I[−]/I₃[−] redox electrolytic solution on the performance of Ru-dye-sensitized nanocrystalline TiO₂ solar cell," *Journal of Photochemistry and Photobiology A*, vol. 169, no. 2, pp. 169–176, 2005.
- [17] H. Kusama and H. Arakawa, "Influence of pyrazole derivatives in I[−]/I₃[−] redox electrolyte solution on Ru(II)-dye-sensitized TiO₂ solar cell performance," *Solar Energy Materials and Solar Cells*, vol. 85, no. 3, pp. 333–344, 2005.
- [18] M. K. Nazeeruddin, R. Humphry-Baker, P. Liska, and M. Grätzel, "Investigation of sensitizer adsorption and the influence of protons on current and voltage of a dye-sensitized nanocrystalline TiO₂ solar cell," *Journal of Physical Chemistry B*, vol. 107, no. 34, pp. 8981–8987, 2003.
- [19] P. Wen, H. Itoh, W. Tang, and Q. Feng, "Single nanocrystals of anatase-type TiO₂ prepared from layered titanate nanosheets: formation mechanism and characterization of surface properties," *Langmuir*, vol. 23, no. 23, pp. 11782–11790, 2007.
- [20] P. Wen, H. Itoh, W. Tang, and Q. Feng, "Transformation of layered titanate nanosheets into nanostructured porous titanium dioxide in polycation solution," *Microporous and Mesoporous Materials*, vol. 116, no. 1–3, pp. 147–156, 2008.
- [21] P. Wen, Y. Ishikawa, H. Itoh, and Q. Feng, "Topotactic transformation reaction from layered titanate nanosheets into anatase nanocrystals," *Journal of Physical Chemistry C*, vol. 113, no. 47, pp. 20275–20280, 2009.
- [22] K. S. Finnie, J. R. Bartlett, and J. L. Woolfrey, "Vibrational spectroscopic study of the coordination of (2,2'-bipyridyl-4,4'-dicarboxylic acid)ruthenium(II) complexes to the surface of nanocrystalline titania," *Langmuir*, vol. 14, no. 10, pp. 2744–2749, 1998.
- [23] S.-H. Kang, S.-H. Choi, M.-S. Kang et al., "Nanorod-based dye-sensitized solar cells with improved charge collection efficiency," *Advanced Materials*, vol. 20, no. 1, pp. 54–58, 2008.
- [24] Y.-B. Tang, C.-S. Lee, J. Xu et al., "Incorporation of graphenes in nanostructured TiO₂ films via molecular grafting for dye-sensitized solar cell application," *ACS Nano*, vol. 4, no. 6, pp. 3482–3488, 2010.
- [25] P. Wen, M. Xue, Y. Ishikawa, H. Itoh, and Q. Feng, "Relationships between cell parameters of dye-sensitized solar cells and dye-adsorption parameters," *ACS Applied Materials & Interfaces*, vol. 4, no. 4, pp. 1928–1934, 2012.
- [26] A. Usami, "Theoretical simulations of optical confinement in dye-sensitized nanocrystalline solar cells," *Solar Energy Materials and Solar Cells*, vol. 64, no. 1, pp. 73–83, 2000.
- [27] Y. Tachibana, K. Hara, K. Sayama, and H. Arakawa, "Quantitative analysis of light-harvesting efficiency and electron-transfer yield in ruthenium-dye-sensitized nanocrystalline TiO₂ solar cells," *Chemistry of Materials*, vol. 14, no. 6, pp. 2527–2535, 2002.

Research Article

Effect of Accelerated Thermal Ageing on the Selective Solar Thermal Harvesting Properties of Multiwall Carbon Nanotube/Nickel Oxide Nanocomposite Coatings

Kittessa T. Roro,¹ Bonex Mwakikunga,² Ngcali Tile,^{1,3} Brian Yalisi,^{1,3} and Andrew Forbes^{1,3}

¹ CSIR National Laser Centre, P.O. Box 395, Pretoria 0001, South Africa

² DST/CSIR National Centre for Nano-Structured Materials, P.O. Box 395, Pretoria 0001, South Africa

³ School of Physics, University of KwaZulu Natal, Private Bag X54001, Durban 5000, South Africa

Correspondence should be addressed to Kittessa T. Roro, kroro@csir.co.za and Bonex Mwakikunga, bmwakikunga@csir.co.za

Received 6 February 2012; Accepted 27 March 2012

Academic Editor: Mohamed Sabry Abdel-Mottaleb

Copyright © 2012 Kittessa T. Roro et al. This is an open access article distributed under the Creative Commons Attribution License, which permits unrestricted use, distribution, and reproduction in any medium, provided the original work is properly cited.

Varying amounts of dispersed multiwalled carbon nanotubes in NiO have been used to develop composites that absorb the solar energy very well but lose very little through emission. Determination of absorptance, α_{sol} , and emissivity, ϵ_{ther} , from such selective solar absorbers shows that the optimum efficiency of 71% can be attained when about 10 mg of MWCNTs are composited with NiO. One such absorber was subjected to thermal ageing tests. The performance criterion (PC) limit for passing the test when simulated for 25 years is $(-\Delta\alpha + 0.25\Delta\epsilon) \leq 0.05$. It was found that the typical absorber had a PC value of -0.01 . This value is much better than the passing limit. Raman spectra of the typical absorber before and after the thermal ageing test showed a reduced intensity in the D and G bands of disordered and graphitic carbon, respectively but an enhancement of the NiO bands indicating loss of carbon atoms due to thermal ageing tests. Simple equations are derived determining the proportion of carbon atoms that are lost and the proportion of carbon atoms that remains in the absorber; both of these are in agreement with the original carbon composition before the thermal ageing test. It is reported that the typical absorber will retain 63% of the carbon after 25 years.

1. Introduction

Due to increase in energy cost, environmental concern, and a need for offgrid power systems, scientists and engineers have been working on ways to harness the energy from the sun. Solar energy is cheap, clean and widely available on the earth. The solar power reaching the earth is nearly four orders of magnitude greater than the power consumption globally. Out of the power of the sunlight reaching the surface of the earth, of 1.2×10^5 TW, man only uses about 13 TW [1]. If all the energy of the sun striking the earth is converted to a useful form of energy with maximum efficiency, the annual energy consumption by humans (4.6×10^{20} Joule/year) could be satisfied within one hour [1]. This clearly suggests a greater need in harvesting solar energy.

The two major technologies widely used for converting solar energy are solar thermal conversion and solar cell

electricity generation. Solar thermal energy is a technology for harnessing solar energy for thermal energy (heat). Solar thermal collectors for water heating use a surface that absorb sunlight and convert it to heat. Solar absorber surfaces are usually black, since dark surfaces demonstrate a particularly high degree of light absorption. The level of absorption indicates the amount of short-wave solar radiation being absorbed, that is, not being reflected. As the absorber warms up to a temperature higher than the ambient temperature, it gives off a great part of the received solar energy in the form of long-wave heat rays. The ratio of absorbed energy to emitted heat is an indication of emission.

In order to reduce energy loss through heat emission, a spectrally selective surface is used. The surface allows the conversion of a high proportion of the solar radiation into heat, while reducing the emission of heat. Thus, the requirements for the optical properties of a selective solar

absorber coating for a high efficient solar-thermal energy conversion are a high spectral absorption (that means a low spectral reflectance) in the wavelength range of the solar radiation combined with low spectral absorption (that means a high spectral reflectance) in the wavelength range of the thermal radiation to reduce radiative heat losses [2]. To achieve this, the solar absorptance, α_{sol} , and thermal emittance $\varepsilon_{\text{ther}}$, of the absorbing surface must be optimized.

Carbon-based nanostructured composite films consisting of nanosize particles embedded in metal oxide host matrix have attractive properties for selective solar absorber coatings to be used for solar water heating and cooking applications [3–6]. Recently, Katumba et al. [4, 5] have compared carbon embedded in three different metal oxides on Al substrates (SiO_2 , ZnO , and NiO). Among the three, carbon in NiO matrix has shown superior optical properties [4, 5].

Much as the composite material (metal oxides and carbon) may show good selectivity, the usual question to ask is “how long does the material sustain these good properties of high absorption α_{sol} and low emittance $\varepsilon_{\text{ther}}$?” For this reason, it is important to determine the values of α_{sol} and $\varepsilon_{\text{ther}}$ versus time in years. To quickly get this information in a shorter time than years, the so-called accelerated ageing tests simulated to cover a period of 25 years are employed [7].

In this work, we present accelerated thermal ageing test results on NiO -carbon nanotube selective solar absorbing composite coated on Al substrate. In the experimental section, we present the conditions for the accelerated thermal ageing test, and we also present the conventional minimum requirements for whether the material passes the test or not.

2. Experimental

2.1. Materials. MWCNTs (synthesized by the CVD method, purity >90%, 110–170 nm in diameter) and all other reagents were purchased from Sigma-Aldrich and used as received without further purification.

2.2. Functionalization of MWCNTs. In order to minimize tube damage, a relatively low acid concentration and exposure time, respectively, were used. The CNTs in the form of powder were added to a mixture of concentrated HNO_3 and H_2SO_4 solution (0–50%) and refluxed at 120°C for 2 hrs to treat the CNTs with the acids. Subsequently, the acidic solution was passed through a filter to collect the acid-treated CNTs. The acid-treated CNTs were washed several times with distilled water and dried at 110°C overnight.

2.3. Substrate Preparation. The absorbing films were coated on rough highly reflecting aluminium substrates. The substrates were cut into a $55 \times 55 \text{ mm}^2$ size and cleaned before deposition. The precleaning process involved cleaning the substrates with aqueous detergent and distilled water in order to remove the grease. Due to poor adhesion to the aluminium surfaces (uncleaned or cleaned with soap and water), the substrates were etched. The precleaned substrates were thoroughly rinsed and dipped in a phosphoric acid bath

at 60°C for about 30 minutes to remove the protective oxide layer. They were then thoroughly rinsed using distilled water to remove the acid. Finally, they were blown dry with a N_2 and coated immediately.

2.4. Nanocomposite Preparation. The preparation of the solution was adopted from a previous experiment [8]. The NiO precursor solution was prepared by dissolving 7.4 g of nickel acetate [(NiAc_2) , $\text{Ni}(\text{CH}_3\text{COO})_2 \cdot 4\text{H}_2\text{O}$] in 50 mL of absolute ethanol [(EtOH) , $\text{CH}_3\text{CH}_2\text{OH}$] followed by magnetic stirring at room temperature for 2 hrs. The solvent, ethanol, is evaporated from the mixture by heating at 50°C for about 20 min until the final solution is reduced to half to make the solution more viscous. Thereafter, 6.3 g of diethanolamine [(DEA), $\text{NH}(\text{CH}_2\text{CH}_2\text{OH})_2$] was added as a chelating agent and then stirred further for 5 min. Following this, 2 g of polyethylene glycol [(PEG), $\text{HO}(\text{CH}_2\text{CH}_2\text{O})_n\text{H}$], a structure directing template, was added to the NiO matrix precursor sol and stirred for 2 min. For the multiwall carbon nanotube precursor solution, different concentrations (10, 50, 100, 150, and 200 mg) of functionalized MWCNTs (f-MWCNTs) were added into 6 mL deionized water and stirred at room temperature prior to mixing with the NiO matrix precursor solutions. The oxide and multiwall carbon nanotube precursor solutions were mixed, and the resultant solution was then further stirred for 24 hrs until the formation of a sol. The final solution was spin-coated at 5000 RPM on top of the precleaned aluminium substrates. Thereafter, the samples were heat-treated at 450°C in nitrogen ambient for one hour.

2.5. Nanocomposite Analysis. The near-normal spectral reflectance of the samples was measured in the $0.3\text{--}2.5 \mu\text{m}$ wavelength range with a Perkin Elmer Lambda 900 spectrophotometer. A spectralon sample was used for reference spectrum measurements (a spectralon sample is a popular white reference standard material used during reflectance measurements to maximize data quality). The reflectance measurements were used to calculate solar absorptance, α_{sol} , of the samples using (1) [2]:

$$\alpha_{\text{sol}} = \frac{\int_{0.3}^{2.5} I_{\text{sol}}(\lambda)(1 - R(\lambda))d\lambda}{\int_{0.3}^{2.5} I_{\text{sol}}(\lambda)d\lambda}, \quad (1)$$

where $I_{\text{sol}}(\lambda)$ is the incident solar spectrum and $R(\lambda)$ is the reflectance of the material. The thermal emittance, $\varepsilon_{\text{ther}}$, of each coating was measured using an emissometer model AE1 from Device and Service (USA) company, with an accuracy of ± 0.01 emittance units. The device has a thermopile radiation detector, which is heated at 82°C . Before taking the measurement, the emissometer is calibrated using two standards, one having an emittance of 0.88, and the other having an emittance of 0.05.

The thermogravimetric analysis (TGA) was done on Perkin-Elmer TGA 4000 thermogravimetric analyzer. Approximately 100 mg final mixture of MWCNT/ NiO precursor solution was placed in open $190 \mu\text{L}$ alumina pan and heated from 25°C to 980°C at a heating rate of 5°C min^{-1} in N_2 atmosphere (flow rate 50 mL min^{-1}).

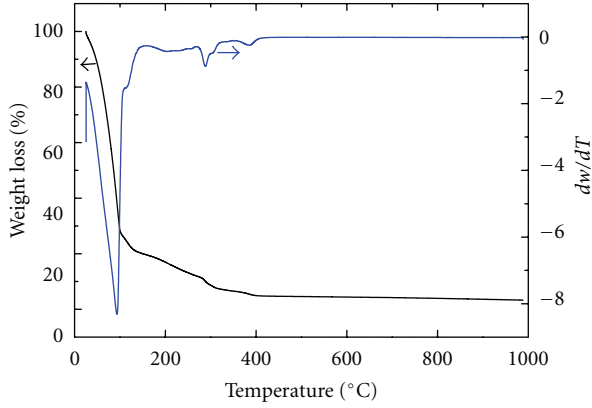


FIGURE 1: Thermogravimetric analysis (TGA) and differential TGA (DTGA) of the typical MWCNT-NiO precursor sol showing that a temperature of more than 400°C is necessary for decomposition of the precursor to the final composite.

The surface morphology of the coatings was investigated using a ZEISS ULTRA plus FEG-SEM scanning electron microscopy. Raman spectroscopy was conducted using a Jobin-Yvon T64000 Raman spectrograph with a 514.5 nm line from an argon ion laser. The T64000 was operated in single-spectrograph mode, with the 1800 lines/mm grating and a 100x objective on the microscope.

2.6. Accelerated Thermal Ageing Test. In order to simulate the expected service life time of the coating of 25 years, the IEA SHC task X [7] has defined a performance criterion (PC):

$$PC = -\Delta\alpha + 0.25\Delta\epsilon, \quad PC = \begin{cases} \leq 0.05 & \text{PASS} \\ > 0.05 & \text{FAIL}, \end{cases} \quad (2)$$

where $\Delta\alpha$ is the change in normal absorptance, and $\Delta\epsilon$ is the change in normal emittance after and before the test calculated, thus:

$$\begin{aligned} \Delta\alpha &= (\alpha_{\text{sol}})_{\text{after test}} - (\alpha_{\text{sol}})_{\text{before test}}, \\ \Delta\epsilon &= (\epsilon_{\text{therm}})_{\text{after test}} - (\epsilon_{\text{therm}})_{\text{before test}}. \end{aligned} \quad (3)$$

If PC is ≤ 0.05 , the sample passes the test. For accelerated thermal ageing test, the sample was exposed to a temperature of 250°C for 200 hours in air.

3. Results and Discussion

3.1. Thermal Characterization. A typical TGA and differential TGA (DTGA) spectra showing the different decomposition pattern of the final f-MWCNT/NiO precursor solution as a function of temperature is depicted in Figure 1. The observed weight loss corresponds to different regions indicating the intervals of the thermal decomposition of the final precursor solution. An initial mass loss of ~70% may be attributed to loss of ethanol and water. The second mass loss appears as a shoulder on the DTGA spectrum and represents a mass loss of ~10% at around 128°C could be due to decomposition of undecomposed nickel acetate or nickel

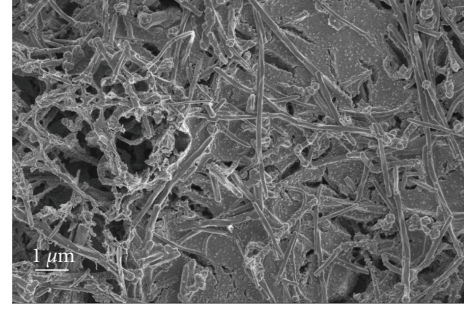


FIGURE 2: Scanning electron microscope image of a typical sample of MWCNT dispersed in NiO.

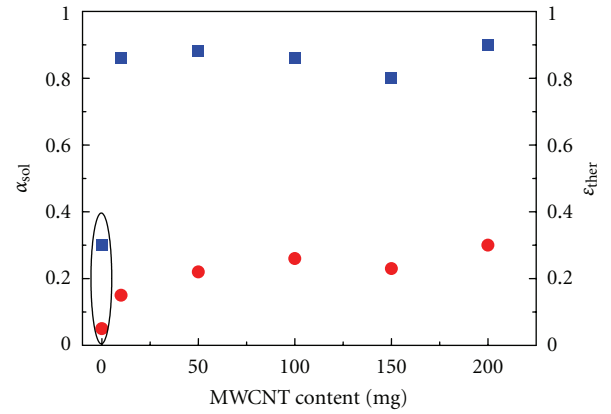


FIGURE 3: Absorptance (square) and emissivity (circle) of several MWCNT/NiO films of varying concentration of MWCNTs.

acetate/diethanolamine complexes. The third, fourth, and fifth mass losses of ~10%, 5%, and 3% at 125°C, 288°C, and 385°C can be attributed to the decomposition of the organic molecules. Taking into consideration the above observation, it has been chosen to heat treat the samples at 450–550°C.

3.2. Surface Morphology. Successful dispersion of the MWCNT in the NiO matrix was achieved. This is shown by a scanning electron microscopy image of the surface morphology of a typical sample of the MWCNT/NiO composite film on Al substrate given in Figure 2.

3.3. Optical Characterization. The solar absorptance α_{sol} calculated using (1) from reflectance spectra and thermal emittance ϵ_{ther} at 82°C measured using the emissometer as a function of f-MWCNT concentrations is shown in Figure 3. It can be seen from the figure that for the sample with no CNTs (quasi-pure NiO obtained by heat treating in air) the solar absorptance value is 0.3. Addition of small mass of CNTs followed by heat treatment in ambient nitrogen drastically increases the solar absorptance of the composite. Further increase in the concentration of CNTs did not change the solar absorptance value. However, the thermal emittance value increases with the increase in concentration of CNTs.

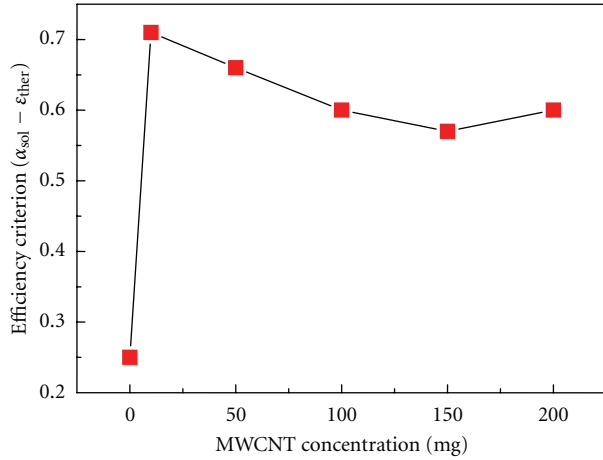


FIGURE 4: A plot of the photothermal conversion efficiency against the MWCNT concentration. The efficiency of light-to-heat conversion is small when the concentration CNT is near zero but increases rapidly when just less than 10 mg of CNTs are added to same mass of NiO. Addition of CNT beyond 10 mg decreases the conversion efficiency.

The photothermal conversion efficiency of the absorber material can be calculated by [6]:

$$\eta = \alpha_{sol} - \epsilon_{ther}. \quad (4)$$

The photothermal conversion efficiency of the f-MWCNT/NiO composites as a function of MWCNT concentration is shown in Figure 4. The efficiency is small when the concentration CNT is quasi zero but increases rapidly when just less than 10 mg of CNTs are added to same mass of NiO. Addition of CNT beyond 10 mg decreases the conversion efficiency. This indicates that only 10 mg MWCNTs in NiO is important in optimising the photothermal conversion efficiency. The optimum efficiency is found to be 71%. The efficiency is not improved by continually increasing the dose of MWCNT to the NiO. In fact, above this critical dose, one can refer to the situation as “poisoning” of the composite.

3.4. Accelerated Thermal Ageing Study. Since it is impractical to obtain the real thermal stability of a solar absorber for its service life time, indoor-accelerated thermal ageing test which simulate the actual scenario has to be conducted to determine whether the coating lasts or not for the duration of the anticipated service time. The reflectance spectra of the samples as deposited and after subjection to the heat treatment are shown in Figure 5. A spectrum of the solar radiation at atmospheric mass AM 1.5 is added to the graph. The red line represents the total reflectance of the absorber coating of the as deposited sample. This data gave a solar absorptance α_{sol} of 0.9 and the thermal emittance ϵ_{ther} (at 82°C) of 0.29.

For the accelerated thermal ageing test, the same sample has been heated in air at 250°C for 200 hrs. The reflectance spectrum is added to Figure 5. From the solar spectrum, absorptance of the sample is calculated. The emittance values

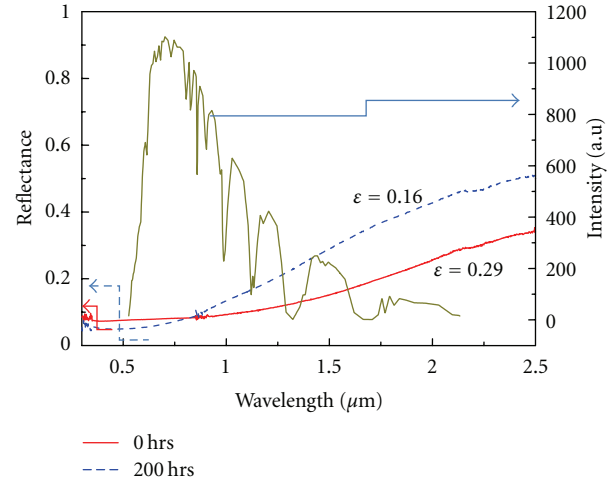


FIGURE 5: Reflectance of the typical selective solar absorber sample before and after thermal ageing test compared to the solar radiation spectrum. From the solar spectrum, absorptance of the sample is calculated. The emittance values as determined from the commercial emissometer are indicated on the reflectance spectra before and after thermal ageing tests.

as determined from the commercial emissometer are indicated on the reflectance spectra before ($\epsilon_{ther} = 0.29$) and after ($\epsilon_{ther} = 0.16$) thermal ageing tests. It can be seen from the spectrum that the reflectance decreased slightly in the solar range ($\lambda < 1 \mu m$) after heat treatment, whereas it increases in the NIR region. The solar absorptance for this sample is 0.88. The change in solar absorptance $\Delta\alpha = -0.02$. Thus, the performance criterion (PC) calculated using equation 2 is -0.012 . This implies that the sample passes the test.

3.5. Raman Spectroscopy Before and After Thermal Ageing Tests. The structural stability of f-MWCNT/NiO composite coatings was studied using micro-Raman spectroscopy. The Raman spectroscopy of the as-deposited sample and sample heat-treated at 250°C in air for 200 hrs are shown in Figure 6. It can be observed from the Raman spectrum of the as deposited sample that the sample shows four distinct peaks at 521.5, 1110.8, 1358.0, and 1583.2 cm^{-1} . The peaks at 521.5 and 1110.8 cm^{-1} are ascribed to the NiO phonons. The other two peaks are due to carbon: a G peak at around 1583.2 cm^{-1} due to optical zone centre vibrations (E_{2g} mode) in graphite of aromatic rings, and a D peak at around 1358 cm^{-1} , due to the disorder activated optical zone edge modes of microcrystalline graphite sheets [8, 9]. After the heat treatment, the NiO phonon enhanced, whereas the D and G peaks were suppressed. This can be explained by slight oxidation of carbon. This minimal change in structure is expected after exposing the sample to this extreme condition. It is interesting to mention that the shape of the Raman spectrum did not change significantly.

As can be seen in Figure 6, Raman spectroscopy of the MWCNT/NiO sample, before and after the accelerated thermal ageing test, shows an enhancement in the NiO phonon at the expense of the intensity of the D and G bands of the carbon.

TABLE 1: Tabulation of phonon peak parameters for a typical sample before and after the ageing test.

Peak assignment	Before thermal ageing test				After thermal ageing test			
	Area, $\int I(\omega)d\omega$ (cm^{-1})	Centre, ω_0 (cm^{-1})	Width, Γ (cm^{-1})	Intensity, I (arb. units)	Area, $\int I(\omega)d\omega$ (cm^{-1})	Centre, ω_0 (cm^{-1})	Width, Γ (cm^{-1})	Intensity, I (arb. units)
NiO	18051	524.3	84.2	171.1	61669	502	122.9	400.4
NiO	73115	1121.2	170.6	341.9	47305	1109.8	143.8	262.5
D	3.4×10^5	1374.9	182.2	1475.9	2.00×10^5	1361.9	143.3	1115.4
G	2.2×10^5	1580.8	101.9	1693.4	1.50×10^5	1579.6	107	1118.5

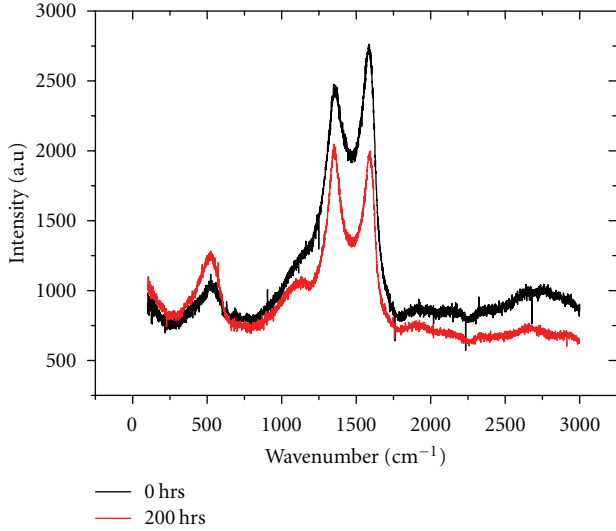


FIGURE 6: Fingerprint Raman spectra for a typical $(\text{MWCNT})_x(\text{NiO})_{1-x}$ before and after thermal ageing test. The main phonon peaks due to NiO (~ 524 and $\sim 1100 \text{ cm}^{-1}$) and carbon ($\omega_D \sim 1370 \text{ cm}^{-1}$ and $\omega_G \sim 1580 \text{ cm}^{-1}$) clearly show a loss of carbon after ageing test.

The main phonon peaks due to NiO (~ 524 and $\sim 1100 \text{ cm}^{-1}$) and carbon ($\omega_D \sim 1370 \text{ cm}^{-1}$ and $\omega_G \sim 1580 \text{ cm}^{-1}$) clearly show a loss of carbon after ageing test. This is a qualitative evidence that the film loses carbon after the ageing tests, thereby rendering the film composition more NiO-rich than before. In other words, in the initial composition, for instance, of $\text{MWCNT}_x(\text{NiO})_{1-x}$, thermal ageing tests make x tend to zero. In order to quantify the proportion of carbon lost, β , and the proportion of carbon remaining in the sample, $1 - \beta$, after the ageing test, one can proceed as follows: if one can represent carbon loss due to thermal ageing test as the difference between the area under the D and G band of graphitic carbon, thus:

$$\Delta(\text{MWCNT}) = \int_{\text{CNT}}^{\text{before}} I(\omega)d\omega - \int_{\text{CNT}}^{\text{after}} I(\omega)d\omega, \quad (5)$$

and the relative “increase” in the proportion accorded to NiO due to the lost carbon atoms as follows:

$$\Delta(\text{NiO}) = \int_{\text{NiO}}^{\text{after}} I(\omega)d\omega - \int_{\text{NiO}}^{\text{before}} I(\omega)d\omega. \quad (6)$$

One can represent the proportion of the carbon lost to the original total carbon composition [10], thus:

$$\begin{aligned} \beta &= \frac{\Delta(\text{MWCNT})}{(\int_{\text{CNT}} I(\omega)d\omega)_{\text{before}}} = 1 - \frac{(\int_{\text{CNT}} I(\omega)d\omega)_{\text{after}}}{(\int_{\text{CNT}} I(\omega)d\omega)_{\text{before}}} \\ &= 1 - \frac{(\int_D I(\omega)d\omega + \int_G I(\omega)d\omega)_{\text{after}}}{(\int_D I(\omega)d\omega + \int_G I(\omega)d\omega)_{\text{before}}}. \end{aligned} \quad (7)$$

The proportion of carbon remaining in the film after the thermal ageing test, $1 - \beta$, should be proportional to the photo-thermal conversion efficiency of the aged sample. Thus, assuming a linear correlation between them, one can write:

$$1 - \beta = \frac{(\int_D I(\omega)d\omega + \int_G I(\omega)d\omega)_{\text{after}}}{(\int_D I(\omega)d\omega + \int_G I(\omega)d\omega)_{\text{before}}} = K(\alpha_{\text{sol}} - \epsilon_{\text{ther}}), \quad (8)$$

where K is proportionality constant.

The areas under the peaks in the Raman spectra were determined by peak fitting. Peak fitting was performed in Origin software. A multipeak fit subroutine was employed to fit the Gaussians to all the phonon peaks present in the whole-sample spectrum. The fitting extracted several parameters for each phonon peak including the area under the peak, the zone centre of the phonon, ω_0 , the full width at half maximum of the peak, Γ , and the maximum intensity of such a phonon peak, I_{max} . These data are tabulated in Table 1.

From the Tuinstra and Koenig work [11], the ratio of the intensities of the D and G bands in carbon allotropes can be used to estimate the grain sizes or intergrain boundary distances, L_a , thus:

$$\frac{I_D}{I_G} = \frac{44 \text{ nm}}{L_a}. \quad (9)$$

I_D/I_G before the ageing test, from Table 1, is 1475.9/1693.4. This implies that L_a before the thermal test, is $\sim 50 \text{ nm}$. After the thermal test L_a reduces to $\sim 44 \text{ nm}$. From Figure 6, it can also be noted that both the NiO phonon at 524 cm^{-1} and 1100 cm^{-1} are asymmetrically broadened. Asymmetric broadening is ascribed to phonon confinement [12], a phenomenon that results from reduction of particle sizes. This phenomenon is observed in particles with diameter between 5 nm and 20 nm [13–19]. The spectra confirm that the NiO particles are indeed nanosized probably less than 20 nm in diameter. It can be noted that the asymmetrical broadening is enhanced after the thermal ageing test as can

be seen in Figure 6. Therefore, as much as the carbon grains reduce in size after the test, it appears that this is true for the NiO grains also, and that the particle sizes reduce to much less than 20 nm after the thermal test.

From Table 1, β can be calculated using (7) thus: $\beta = 1 - ((2 \times 10^5 + 1.5 \times 10^5) / (3.37 \times 10^5 + 2.16 \times 10^5)) = 0.37$. Also, in the present study the proportion of carbon remaining in the sample after the test, $1 - \beta$, from (8), is $1 - 0.37 = 0.63$ and the photo-thermal conversion efficiency of the aged sample, from (4), $0.88 - 0.16 = 0.72$. This implies that the proportionality constant K can be estimated to be $K \sim 0.63/0.72 = 0.875 \sim \text{unity}$. This finding reveals the fact that the values of proportions of carbon remaining in the selective solar absorber after ageing at any given time determined from Raman spectroscopy can be used to estimate the absorber's performance at that time in terms of the photothermal conversion efficiency namely $\eta = \alpha_{\text{sol}} - \epsilon_{\text{ther}} = (1/K)(1 - \beta)$.

Thermal ageing tests on five more samples and their corresponding Raman signatures are ongoing. These results will help in the further validation of the currently derived η - β relationship.

4. Conclusions

Spectrally selective MWCNT/NiO nanocomposite coatings of varying CNT concentration were prepared on Al substrate by a sol-gel process. Solar absorption and thermal emission values as a function of CNT concentration have been presented. A typical sample was taken for accelerated thermal ageing test. Preliminary accelerated thermal ageing test on the sample showed that the composite material passes the test with PC value of -0.01 which is below the lower limit of 0.05 . Raman spectroscopy was used to estimate the proportions of carbon atoms lost to those that remain in the sample after the thermal ageing test. The proportion of carbon atoms that still remain in the sample after the thermal test is correlated to the photo-thermal conversion efficiency. More experimental results are underway to validate this first correlation and to determine the performance criterion limits from Raman spectra.

List of Abbreviations and Nomenclature

α_{sol} :	Normal solar absorptance
ϵ_{ther} :	Thermal emittance
I_{sol} :	Direct normal solar irradiance
η :	Photothermal conversion efficiency
PC:	Performance criterion
f-MWCNT:	Functionalized multiwall carbon nanotube
β :	The proportion of carbon remaining in the material
FEG-SEM:	Field emission gun-scanning electron microscopy.

Acknowledgments

The authors acknowledge the financial assistance from the CSIR under these project numbers LHIE100 and LHAE00.

K. Roro acknowledges the financial assistance from the CSIR for young researcher establishment funding (Project no.: YREF_2011_32) and B. Mwakikunga acknowledges the characterization facilities from Project number HGER27S.

References

- [1] G. W. Crabtree and N. S. Lewis, "Solar energy conversion," *Physics Today*, vol. 60, no. 3, pp. 37–42, 2007.
- [2] J. A. Duffie and W. A. Beckman, *Solar Engineering of Thermal Processes*, John Wiley & Sons, New York, NY, USA, 1980.
- [3] D. Katzen, E. Levy, and Y. Mastai, "Thin films of silica-carbon nanocomposites for selective solar absorbers," *Applied Surface Science*, vol. 248, no. 1–4, pp. 514–517, 2005.
- [4] G. Katumba, L. Olumekor, A. Forbes et al., "Optical, thermal and structural characteristics of carbon nanoparticles embedded in ZnO and NiO as selective solar absorbers," *Solar Energy Materials and Solar Cells*, vol. 92, no. 10, pp. 1285–1292, 2008.
- [5] G. Katumba, G. Makiwa, T. R. Baisitse, L. Olumekor, A. Forbes, and E. Wäckelgård, "Solar selective absorber functionality of carbon nanoparticles embedded in SiO₂, ZnO and NiO matrices," *Physica Status Solidi C*, vol. 5, no. 2, pp. 549–551, 2008.
- [6] Y. Mastasi, S. Polarz, and M. Antoriet, "Silica-carbon nanocomposite—a new concept for the design of solar absorbers," *Advanced Functional Materials*, vol. 12, no. 3, pp. 197–202, 2002.
- [7] B. Carlsson, U. Frei, M. Kohl, and K. Moller, "Accelerated life testing of solar energy materials—case study of some selective materials for DHW systems," IEA SHCP Task X, 1994.
- [8] K. T. Roro, N. Tile, B. Mwakikunga, B. Yalisi, and A. Forbes, "Solar absorption and thermal emission properties of multiwall carbon nanotube/nickel oxide nanocomposite thin films synthesized by sol-gel process," *Materials Science and Engineering B*, vol. 177, no. 8, pp. 581–587, 2012.
- [9] A. C. Ferrari and J. Robertson, "Interpretation of Raman spectra of disordered and amorphous carbon," *Physical Review B*, vol. 61, no. 20, pp. 14095–14107, 2000.
- [10] B. W. Mwakikunga, M. Maaza, K. T. Hillie, C. J. Arendse, T. Malwela, and E. Sideras-Haddad, "From phonon confinement to phonon splitting in flat single nanostructures: a case of VO₂@V₂O₅ core-shell nano-ribbons," *Vibrational Spectroscopy*, vol. 61, pp. 105–111, 2012.
- [11] F. Tuinstra and J. L. Koenig, "Raman Spectrum of Graphite," *Journal of Chemical Physics*, vol. 53, no. 3, pp. 1126–1130, 1970.
- [12] H. Richter, Z. P. Wang, and L. Ley, "The one phonon Raman spectrum in microcrystalline silicon," *Solid State Communications*, vol. 39, no. 5, pp. 625–629, 1981.
- [13] B. W. Mwakikunga, E. Sideras-Haddad, and M. Maaza, "First synthesis of vanadium dioxide by ultrasonic nebula-spray pyrolysis," *Optical Materials*, vol. 29, no. 5, pp. 481–487, 2007.
- [14] B. W. Mwakikunga, A. Forbes, E. Sideras-Haddad, R. M. Erasmus, G. Katumba, and B. Masina, "Synthesis of tungsten oxide nanostructures by laser pyrolysis," *International Journal of Nanoparticles*, vol. 1, no. 3, pp. 185–202, 2008.
- [15] B. W. Mwakikunga, A. Forbes, E. Sideras-Haddad, and C. Arendse, "Raman spectroscopy of WO₃ nano-wires and thermo-chromism study of VO₂ belts produced by ultrasonic spray and laser pyrolysis techniques," *Physica Status Solidi A*, vol. 205, no. 1, pp. 150–154, 2008.
- [16] G. Katumba, B. W. Mwakikunga, and T. R. Mothibinyane, "FTIR and Raman spectroscopy of carbon nanoparticles in

- SiO₂, ZnO and NiO matrices,” *Nanoscale Research Letters*, vol. 3, no. 11, pp. 421–426, 2008.
- [17] M. Govender, L. Shikwambana, B. W. Mwakikunga, A. Forbes, E. Sideras-Haddad, and R. M. Erasmus, “Esopen accessformation of tungsten oxide nanostructures by laser pyrolysis: stars, fibres and spheres,” *Nanoscale Research Letters*, vol. 6, no. 1, article 166, 2011.
- [18] R. Machaka, B. W. Mwakikunga, E. Manikandan, T. E. Derry, and I. Sigalas, “Raman spectrum of hot-pressed boron suboxide,” *Advanced Materials Letters*, vol. 2, no. 1, p. 68, 2011.
- [19] G. Goudec and Ph. Colamban, “Raman spectroscopy of nanomaterials: how spectra relate to disorder, particle size and mechanical properties,” *Progress in Crystal Growth and Characterization of Materials*, vol. 53, no. 1, p. 56, 2007.

Research Article

Photoelectrochemical Performance of Smooth TiO₂ Nanotube Arrays: Effect of Anodization Temperature and Cleaning Methods

Chin Wei Lai and Srimala Sreekantan

School of Materials and Mineral Resources Engineering, Universiti Sains Malaysia, Engineering Campus, Seberang Perai Selatan, Pulau Pinang, 14300 Nibong Tebal, Malaysia

Correspondence should be addressed to Srimala Sreekantan, srimala@eng.usm.my

Received 9 December 2011; Revised 20 February 2012; Accepted 20 February 2012

Academic Editor: James T. Mcleskey

Copyright © 2012 C. W. Lai and S. Sreekantan. This is an open access article distributed under the Creative Commons Attribution License, which permits unrestricted use, distribution, and reproduction in any medium, provided the original work is properly cited.

The formation of self-organized titanium dioxide (TiO₂) nanotube arrays without bundling or clustering is essential for their high efficiency in photoelectrochemical (PEC) application. The present paper reports on the use of different temperatures to control the specific architecture of nanotube arrays and effective cleaning techniques to ensure the formation of clean TiO₂ nanotube surface. The wall thickness of nanotube arrays could be controlled from 12.5 nm to 37.5 nm through different anodization temperature ranging from 10°C to 80°C. Furthermore, ultrasonic cleaning combined with acetone showed the high-ordered TiO₂ nanotube arrays without morphological disorder, bundling, and microcrack problems. Based on the results obtained, a higher PEC response of 1 mA/cm² and a photoconversion efficiency of 1.3% could be achieved using a wall thickness of 12.5 nm and defect-free TiO₂ nanotube arrays for low charge transfer resistance.

1. Introduction

At present, modern society is habituated to a high degree of mobility, fast communication, and daily comfort, all of which require considerable energy input. The increase in world population and industrial development has all led to accelerated energy consumption, which, in turn, leads to various diseases and global warming [1]. Due to these factors, new energy sources that are inexhaustible and nonpolluting have been studied intensively [2–4]. In recent years, interest in photocatalysts for the production of hydrogen as a clean fuel, as concerns over the cost of fossil fuels to the economy, environment, and national security have become paramount. In these aspects, one-dimensional titanium dioxide (TiO₂) has emerged as the leading candidate for developing hydrogen fuel cell as a potential future energy and possibly the best substitute for fossil fuel [5, 6]. The uniform morphology, better charge transfer properties, and high surface area with controllable pore size of TiO₂ nanotube arrays make them a promising functional material in photoelectrochemical (PEC) application [7–12]. However, the ability to produce

the best dimension for such application has remained a major challenge.

Geometrical features of the nanotube arrays, including length, pore diameter, and wall thickness, are controlled by a variety of parameters, such as anodic voltage, anodization time, electrolyte composition (fluoride content, viscosity, and pH), electrolyte temperature, and surface condition of nanotube arrays [13–15]. However, a detailed investigation on the effect of electrolyte temperature and effective cleaning technique to produce clean TiO₂ nanotube arrays for PEC performance is lacking. Electrolyte temperature plays a critical role in the determination of the final dimensions of the nanotubes' various surface morphologies and architectures [12, 16]. The earlier report on the effect of electrolyte temperature has been reported by Mor et al. since 2005 [17]. They reported that wall thickness of the nanotube was increased with decreasing anodization temperature while the length of the nanotube increases with decreasing anodization bath temperature from 50°C to 5°C. Later, Wang and Lin claimed that the diameters of nanotube arrays are smaller in an ice bath condition when anodized in organic electrolyte

[18]. However, their anodization process was only conducted either at room temperature or in an ice bath. Next, Chen et al. reported that the inner diameter of the tubes increases with increasing electrolyte temperature from 10°C to 35°C. They found that the tube profile could be improved from the general V-shape to a U-shape by gradually increasing the electrolyte temperature [19]. However, the listed work was conducted at low electrolyte temperature; details on the investigation using higher temperature (>50°C) were not reported. The present paper studies the electrochemical anodization of Ti foil in organic electrolyte (ethylene glycol (EG)), with main focus on the effect of electrolyte temperatures from 10°C to 80°C on the growth of TiO₂ nanotube arrays.

Previous researchers have studied various cleaning procedures for TiO₂ nanotubes and have come up with an effective way of producing clean TiO₂ nanotube surfaces. Zhu et al. reported that TiO₂ nanotube arrays cleaned with ethanol, followed by the supercritical CO₂ drying technique, could effectively remove the structural disorder from oriented TiO₂ nanotube arrays by removing capillary stress [20]. Later, Kim et al. claimed that the structural disorder (nanoglass) and bundling problem of TiO₂ nanotube arrays could be avoided by forming a protective top layer on polished Ti samples to delay the chemical attack of the tube ends [21]. However, these techniques are costly and complicated. In addition, some authors have reported that hydrofluoric acid (HF) treatment can significantly remove the precipitated layer on the top surface of nanotubes [18, 22–24]. However, the issue is still far from being solved. The chemical etching of HF for as-anodized TiO₂ nanotubes can remove the precipitated layer, but etching the nanotube surface can make it serrated and irregular in texture [18, 24]. The serrated surface and nanotube disorder could significantly retard PEC performance due to the higher density of surface recombination in the photoinduced electrons [20]. To minimize the distortion-induced surface defects in nanotube arrays and reduce the consumption of hazardous chemical from HF, the present study introduces a simple, cost-effective, fast, and environmentally safe technique for producing highly specific clean surface areas of TiO₂ nanotube arrays using ultrasonic cleaning combined with acetone. The high aspect ratio, bundle-free TiO₂ nanotube arrays alter the spatial dimensionality of the transport and recombination mechanism, which affect photon absorption efficiency and PEC response [12, 15, 20, 25]. The mechanistic understanding of various electrolyte temperatures and cleaning methods is very important for the controlled growth of ordered TiO₂ nanotube structures, which have potential uses in the development of viable hydrogen fuel cell for a sustainable energy system.

2. Experimental

A total of 99.6% Ti foils, with a thickness of 0.127 mm (STREM Chemicals), were used in the current study. Ti foils were cut into desired dimensions (50 mm × 10 mm). Before anodization, the Ti foils were degreased in ethanol through sonication for 30 min. The foils were then rinsed in

deionized (DI) water and dried by the blowing of nitrogen. After drying, the Ti foil was placed in 100 mL EG containing 5 wt% ammonium fluoride (NH₄F) and 5 wt% hydrogen peroxide (H₂O₂) [15]. Anodization was performed in a two-electrode bath with Ti foil as the anode and a platinum rod as the cathode. The experiments were conducted at 10°C to 80°C electrolyte temperature.

During the anodization process, air bubble was blown in the electrolyte to maintain a uniform current near the Ti foil. Anodization was done at a constant potential of 60 V using a Keithley DC Power Supply for 1 h. After the anodization process, as-anodized Ti foils were cleaned using different cleaning treatments. For the first approach, ultrasonic cleaning combined with DI water was applied to the as-anodized sample using a WiseClean Ultrasonic Cleaner WUC-A06H (40 kHz, 150 W). For the second approach, the as-anodized sample was cleaned using DI water with a hot rinse at 90°C. For the third approach, ultrasonic cleaning combined with 2% HF was applied to the as-anodized sample. The last approach used ultrasonic cleaning combined with acetone for the as-anodized sample. All samples were dried in nitrogen stream. After the cleaning and drying treatments, the as-anodized samples were annealed at 400°C for 4 h in argon atmosphere for conversion into the TiO₂ anatase phase. The morphology of the anodized Ti foils was viewed using a field emission scanning electron microscope (FESEM) (Zeiss SUPRA 35VP) at a working distance of approximately 1 mm. To obtain the thickness of the anodic oxide formed, cross-sectional measurements were conducted on mechanically bent samples, wherein a partial lift-off of the anodic layer occurred. Phase determination of the anodic layer was determined via XRD (Philips, PW 1729), operated at 45 kV and 40 mV. The Raman spectra were recorded at room temperature using an LS 55 luminescence spectrometer (Jobin-Yvon HR 800UV).

The PEC properties of the samples were characterized using a three-electrode PEC cell, with TiO₂ nanotube arrays as the working photoelectrode, platinum rod as a counter-electrode, and saturated calomel electrode (SCE) as the reference electrode. A solution of 1 M KOH with 1 wt% EG was used as the electrolyte in the current experiment. All three electrodes were connected to the potentiostat (μ Autolab III), and the current and voltage were measured. An 800 W/m² xenon lamp (Zolix LSP-X150) was used to produce a largely continuous and uniform spectrum; the quartz glass permitted 100% transmittance of the light as the xenon lamp shined on the TiO₂ nanotube arrays (photoanode). The xenon lamp was switched on after the three electrodes were connected to the potentiostat. During the voltage sweeping (5 mV/s), the corresponding photocurrent was measured. Subsequently, the photocurrent was plotted against the potential applied. The photoconversion efficiency (η) for the water splitting reaction was calculated based on the following equation [26–28]:

$$\eta (\%) = j_p \frac{[(V_{ws} - V_B)]}{I_o}, \quad (1)$$

where j_p is the photocurrent density (mA/cm²); V_{ws} is 1.229 V is the potential corresponding to the Gibbs free energy

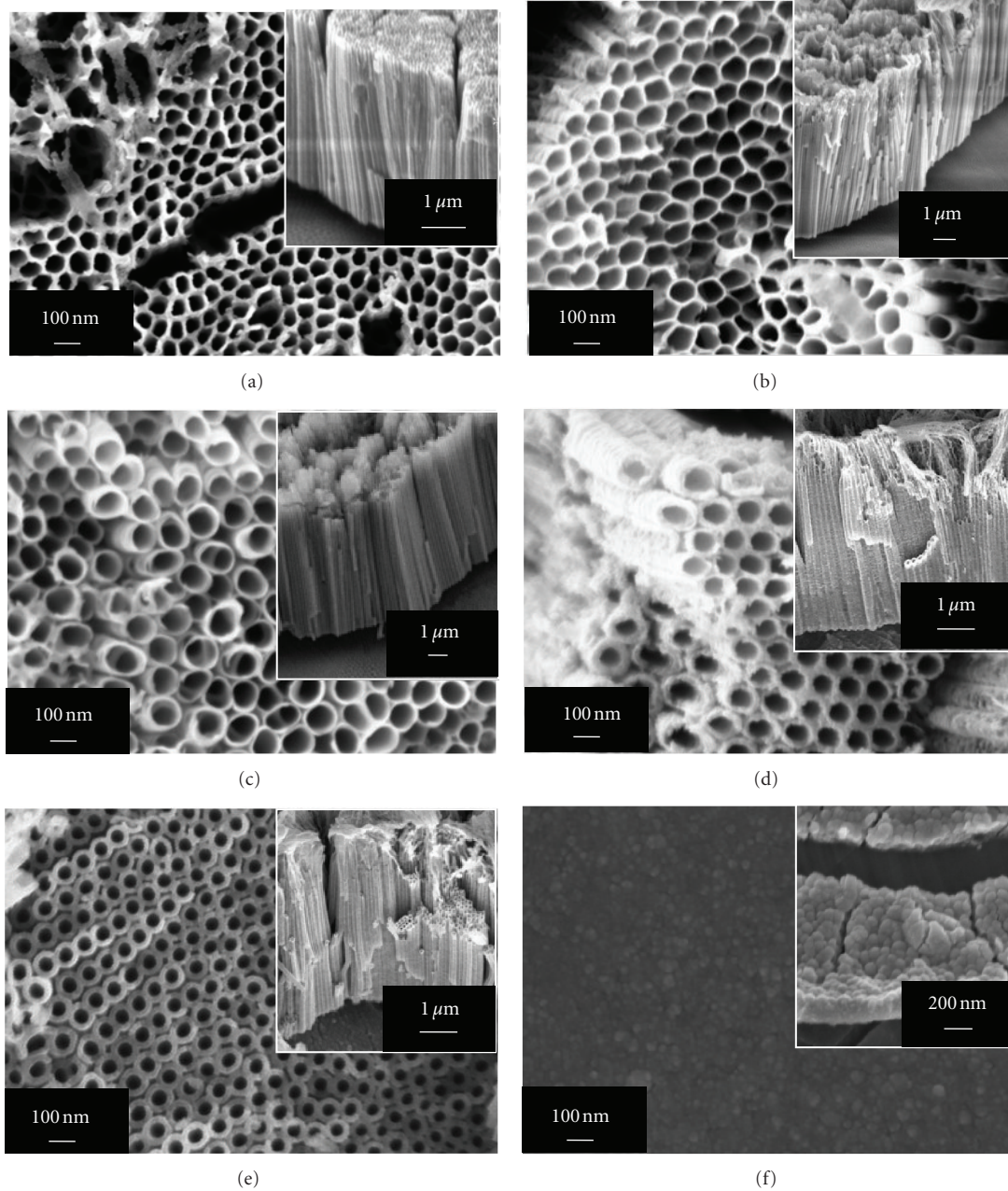


FIGURE 1: FESEM images of TiO_2 nanotube arrays fabricated at (a) 10°C , (b) 20°C , (c) room temperature, (d) 40°C , (e) 60°C , and (f) 80°C in ethylene glycol electrolyte containing 5 wt% H_2O_2 and 5 wt% NH_4F anodized at 60 V for 1 h. Insets are the cross-section morphologies of the TiO_2 nanotube arrays.

change per photon required to split water; V_B is the bias voltage applied between the working and counterelectrodes; I_o is the power density of the incident light (mW/cm^2).

3. Results and Discussion

3.1. Effect of Anodization Temperature. The current section discusses the effect of anodization temperature on the morphology of the TiO_2 array nanotubes. Figure 1 shows the FESEM images of the surface morphology of the Ti foils

anodized in EG containing 5 wt% H_2O_2 and 5 wt% NH_4F at 60 V for 1 h with various anodization temperatures ranging from 10°C to 80°C . Insets are the cross-section morphologies of the TiO_2 nanotube arrays. These images show that the appearance of anodic oxides on the Ti foils was dependent on the anodization temperature in the fluorinated electrolyte. The relationship of the length, pore diameter, and wall thickness of the tubes with different anodization temperatures are summarized in Figure 2(a). In this graph, two different stages are shown to indicate the changing dimensions of TiO_2

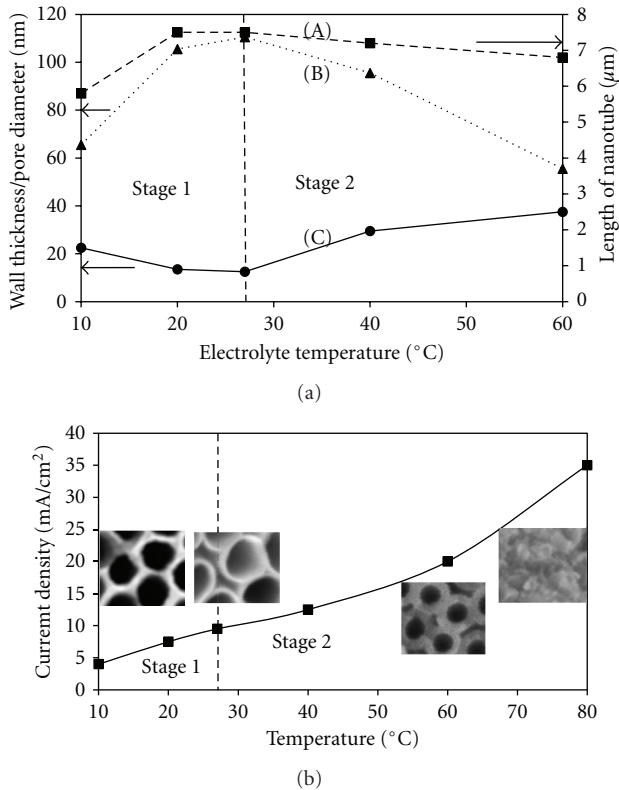


FIGURE 2: (a) Effect of anodization temperature on the (A) length, (B) pore diameter, and (C) wall thickness of the TiO₂ nanotube arrays anodized at 60 V for 1 h; (b) current density as function of anodization temperature.

nanotube arrays at various electrolyte temperatures. Stage 1 represents the cool condition of the electrolyte, which was below room temperature (27°C), whereas Stage 2 represents the warm condition of the electrolyte, which was beyond room temperature (27°C).

The sample anodized at a low temperature of 10°C (Figure 1(a)) produced nanotubes with an inner pore diameter of ~65.5 nm, a length of ~5.8 μm, and a wall thickness of ~22.5 nm. The FESEM image shows microcracks or defects in this sample. When the anodization temperature was increased to 20°C, the inner pore diameter of the nanotubes increased to an average 105.5 nm, and the length to ~7.5 μm; however, the wall thickness decreased to ~13.5 nm (Figure 1(b)). The shape of the nanotubes became much more uniform, compared with those produced at low anodization temperatures. When the anodization process was subsequently conducted at room temperature (27°C), TiO₂ nanotube arrays exhibited an average inner pore diameter of 110.5 nm, a length of ~7.5 μm, and a wall thickness of 12.5 nm (Figure 1(c)). Smooth, circular nanotube arrays were obtained at room temperature without a defect in the large area. When the electrolyte temperature was increased to 40°C, the wall thickness of the nanotube increased to 29.5 nm, with an inner pore diameter of 95.5 nm, and a length of approximately 7.2 μm (Figure 1(d)). Further increasing the temperature to 60°C increased the wall

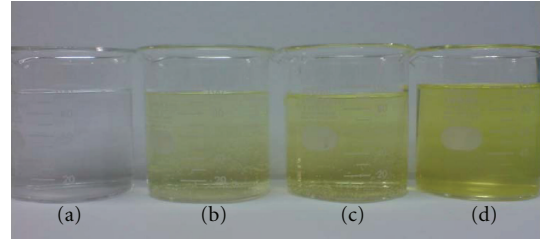


FIGURE 3: Color of electrolyte obtained upon Ti foil anodized in ethylene glycol containing NH₄F and H₂O₂ (a) before anodization process, (b) at 10°C, (c) at room temperature, and (d) at 60°C.

thickness of the nanotubes to 37.5 nm, with an inner pore diameter of 55.5 nm, and a length of approximately 6.8 μm (Figure 1(e)). However, further increasing the electrolyte temperature to 80°C negatively affected the self-organization of the anodic oxide, wherein the nanotube structure disappeared and anodic oxide consisted of an irregular porous layer, as shown in Figure 1(f). The thickness of the porous layer was approximately 0.3 μm.

In Stage 1, a temperature of up to 27°C reduced the tube's wall thickness and increased its length. The difference in wall thickness may be attributed to the increasing current density with temperature. This result clearly indicates that the chemical dissolution is increased, as shown in Stage 1 in Figure 2(b). At this stage, the rate of the oxide dissolution reaction is believed to be faster than that of Ti etching. This assumption may be attributed to the higher driving force for ionic transport through the barrier layer at higher temperatures that cause fast movements of the F⁻ and H⁺ species at the Ti/TiO₂ interface, thus resulting in the formation of thin nanotube walls [12, 16, 19].

In Stage 2, the wall thickness of the tube structure significantly increased. Furthermore, higher current density was found in the case of higher temperature environment (Figure 2(b)). This result may be attributed to the excessive Ti⁴⁺ ions diffusing outward and the O²⁻ ions transported inward at a faster rate under high temperature oxidation environments, which resulted in the formation of thick-walled TiO₂ nanotube arrays. This statement is further supported by the interaction between excessive Ti⁴⁺ ions with H₂O₂ that resulted in the intense yellowish color of electrolyte at higher temperature (Figure 3(d)), compared with the pale yellowish electrolyte at a lower temperature (Figure 3(b)) [29]. However, beyond 80°C of the electrolyte is detrimental to the formation of self-organized nanotube arrays. The chemical etching exceeded anodic oxidation, and the balance required for self-ordering was diminished. The results of the current study indicate that the growth of nanotube arrays is due to the competition between field-assisted oxide dissolution and the diffusion rate of ionic species, field-assisted oxidation of Ti, and the chemical etching process that could be controlled by the anodization temperature. Thus, the equilibrium reactions are important in driving the Ti/TiO₂ interface deeper into the Ti foil. A schematic illustration of the diffusion rate of ionic species

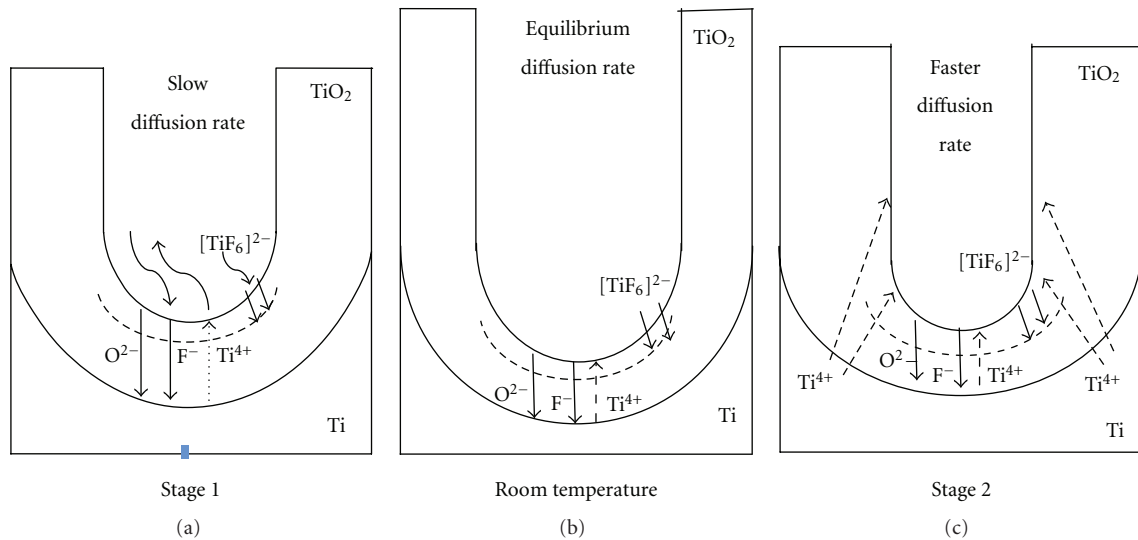


FIGURE 4: Schematic illustration explaining the diffusion rate of ionic species at metal-oxide layers above the Ti foil, (a) Stage 1 (cool condition), (b) room temperature (27°C), and (c) Stage 2 (warm condition).

at the barrier layer at different temperatures is exhibited in Figure 4.

The crystal structure of the as-anodized and TiO₂ nanotubes after annealing at 400°C in argon atmosphere fabricated at various electrolyte temperatures were identified via XRD. As-anodized TiO₂ nanotubes with an amorphous structure and no crystalline phase were observed at 10°C to 80°C anodization temperature (Figure 5(a)). The only peaks related to the Ti substrate were exhibited. These results indicate that the anodization temperature is not sufficient to induce the crystallinity of TiO₂. Therefore, heat treatment was conducted at 400°C, and TiO₂ nanotubes were found to be crystalline with anatase TiO₂. As shown in the XRD patterns in Figure 5(b), the peaks from anatase TiO₂ can be detected at 2θ of 25.5°, 38.5°, 48°, 54.5°, and 55.5°, which correspond to (101), (004), (200), (105), and (211), respectively. Although, the predominant anatase phases were detected in all samples, the peak intensities of (101) at 25.5°, (004) at 38.5°, (200) at 48°, (105) at 54.5°, and (211) at 55.5° for the sample fabricated at room temperature, 40°C, and 60°C were stronger than the sample produced at 10, 20, and 80°C. This result implies that higher thickness of the nanotube layer is responsible for the higher intensity of the anatase peaks (Figure 5 versus Figure 2). This is evident from the reduction in Ti peak intensities.

To verify the results, selected samples were analyzed via Raman to validate the crystal structure and presence of the anatase phase (Figure 6). The as-anodized TiO₂ nanotube arrays fabricated at 40 and 60°C were affirmed to be amorphous in nature; no anatase peak was observed in the Raman spectrum. However, a major band position at 192, 390, 510, and 635 cm⁻¹ was detected in the annealed TiO₂ nanotubes, corresponding to the bonding vibration of anatase phase. All samples formed anatase as the dominant phase after the annealing process at 400°C in argon atmosphere.

3.2. Effect of Different Cleaning Methods after Anodization.

After the anodization process, TiO₂ nanotubes are often covered with precipitates that need to be removed using suitable cleaning agents and methods. The pores on the oxide layer are formed because of the fluoride ions and the electric field-assisted dissolution. Both oxidation and chemical dissolutions are active at the bottom of the pores. In this condition, Ti⁴⁺ was dissolved and ejected from the nanopore to the surface, and accumulated at the entrance of the nanopore. This phenomenon could be the Ti(OH)₄ formed via the instantaneous hydrolysis reaction, which leads to the generation and accumulation of Ti(OH)₄ precipitate at the entrance of the nanopores to form the flaky structure on the surface TiO₂ nanotube [12, 30]. Therefore, the type of solvent and technique required in removing the solvent from the tubular structure is critical. This phenomenon is discussed in detail in the following section.

For comparison, a set of experiments was conducted in EG with the addition of 5 wt% H₂O and 5 wt% NH₄F under the same anodization conditions. All samples were anodized at 60 V for 1 h at room temperature. One of the samples was ultrasonically cleaned in distilled water for 1 min and subsequently dried under flowing N₂ gas. Figure 7(a) shows the top and side view images of the as-anodized sample before annealing. The image clearly shows the presence of clusters of nanotube bundles and microcrack formation. Such structure is believed to be caused by the capillary stress created during the evaporation of liquids from the nanotubes [20]. The unbalanced capillary stress within the interior and exterior of the pores accelerates the distortion of the pore structure near the ends of the nanotube, collapsing to produce an overlayer that covers the opening of the nanotubes. The extent of unbalanced capillary stress is dependent on the nanotube length and the surface tension of the cleaning solvent. A similar observation

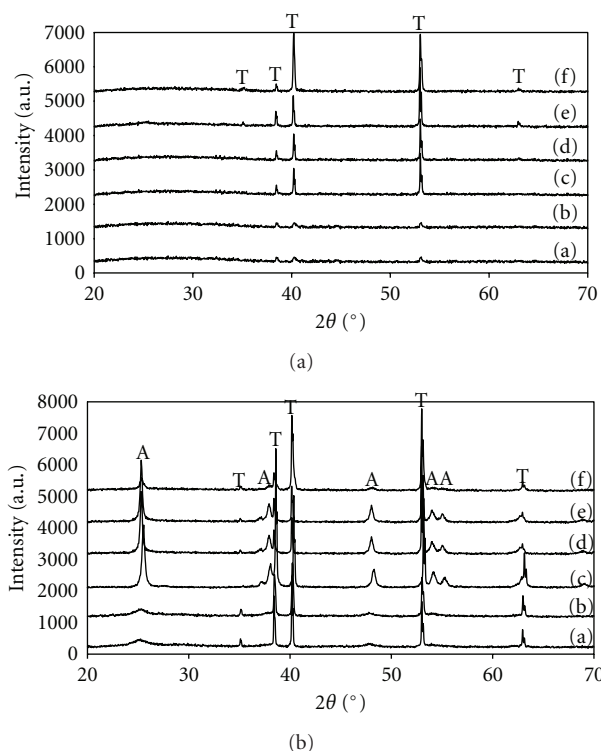


FIGURE 5: (a) XRD patterns of as-anodized TiO₂ nanotube arrays fabricated at (a) 10°C, (b) 20°C, (c) room temperature, (d) 40°C, (e) 60°C, and (f) 80°C; (b) XRD patterns of annealed TiO₂ nanotube arrays fabricated at (a) 10°C, (b) 20°C, (c) room temperature, (d) 40°C, (e) 60°C, and (f) 80°C after annealing at 400°C in argon atmosphere (A: anatase TiO₂; T: titanium).

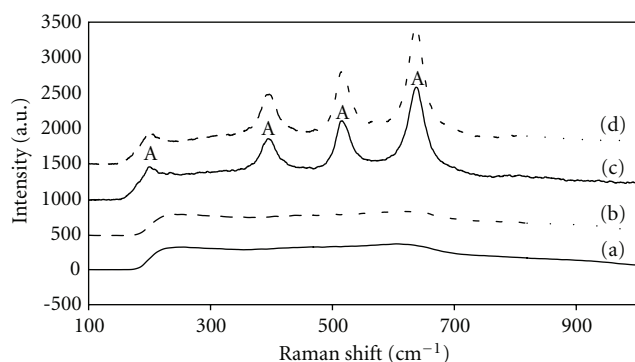


FIGURE 6: Raman spectra of (a) as-anodized TiO₂ nanotube arrays fabricated at 40°C, (b) as-anodized TiO₂ nanotube arrays fabricated at 60°C, (c) annealed TiO₂ nanotube arrays fabricated at 40°C, and (d) annealed TiO₂ nanotube arrays fabricated at 60°C (A: anatase).

was found in the sample cleaned by hot rinsing at 90°C using distilled water for 1 min and subsequently dried under flowing N₂ gas (Figure 7(b)). The presence of clusters of TiO₂ nanotube bundles and microcracks were evident in the sample.

The samples fabricated under the same conditions were cleaned via two different approaches: (1) chemical etching using 2% HF with ultrasonic and (2) ultrasonic cleaning

using acetone. Figure 8 shows the FESEM images of as-anodized nanotubes ultrasonically cleaned with 2% HF for 10, 15, 20, and 60 s. The apparent overlayers still covered the end of the nanotube channels. The different cleaning times had no significant effect on the top view of the nanotubes. However, the length of the nanotubes was reduced from 7.5 μm to 6.0 μm after 20 s (Figure 8(c)), and the length was further reduced to 3.5 μm after 60 s (Figure 8(d)). A longer cleaning time in HF might have increased the etching rate. Consequently, the nanotubes tend to break and collapse on each other, thus forming overlayers that cover them.

Figure 9 shows the FESEM images of TiO₂ nanotubes cleaned with acetone, followed by 1, 2, and 10 min of ultrasonic agitation under condition of 150 W and 40 kHz. The overlayer that covered the nanotube was minimized through ultrasonic agitation for 1 and 2 min (Figures 9(a) and 9(b)). These results show a better result of self-standing, well-ordered nanotubes with a clear opening. The nanotube arrays have an average length of 7.5 μm and a diameter of approximately 90 nm. Figure 9(c) shows the FESEM images for 10 min of ultrasonic agitation. The nanotube length was shorter by 4 μm. This result could be because the TiO₂ wall could not sustain the agitation for a longer period; thus, the nanotubes broke down to form shorter nanotubes. The broken nanotubes led to overlayer formation that covered the short nanotubes. Based on the result obtained, approximately 1 or 2 min ultrasonic agitation in acetone is effective in removing overlayers from the nanotubes leading to the formation of free-standing TiO₂ nanotube arrays without breaking the tube structure. This result is in agreement with the work reported by Xu et al. [31], in which they reported that treating time of ultrasonic was extended to 40 min, nanotubes broke down to form shorter tubes and no nanotubes were left on the Ti substrate if the treating time of ultrasonic further increased to 60 min.

The working principle of ultrasonic cleaning is performed using sound waves to microscopically scrub and clean all internal and external surfaces of the nanotube in the presence of acetone. The higher frequency of ultrasonic cleaning, combined with acetone, can penetrate deeper and clean away the Ti(OH)₄ precipitate layer at the entrance of the nanotube arrays. During ultrasonic cleaning, numerous gas bubbles are formed. The great amount of pressure exerted on the gas bubble leads to a sudden cavitation implosion. Thus, the liquid molecules collide, releasing a vast amount of energy that rapidly increases local temperature, producing a high-energy liquid stream that collides with the surface of the nanotube arrays. The reasons can be attributed to the cavitations, acoustic streaming, strong agitation and thermal oscillating flow initiated by the ultrasonic vibration that eventually increase the local temperature and produce a high energy liquid stream. This theoretical has been reported by Oh et al. and Feng et al. [32, 33]. Thus, the collision agitates contaminants adhering to the surface of the nanotube, which effectively and efficiently dislodges them at micron levels.

Another reason for the reduced degree of morphological disorder in ultrasonic agitation combined with acetone could be attributed to lower surface tension. This result indicates that acetone can reduce the surface tension and capillary

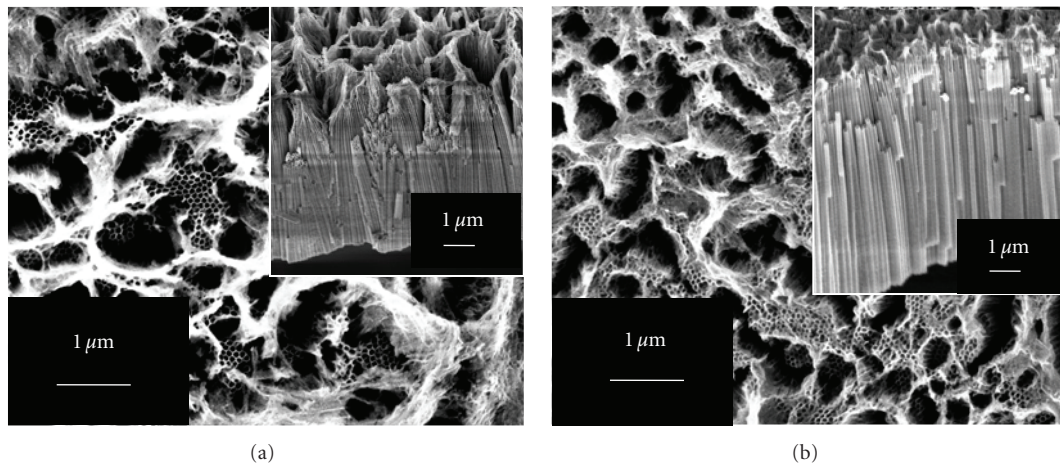


FIGURE 7: FESEM images of TiO₂ nanotubes obtained via different cleaning methods after the anodization process; (a) ultrasonically cleaned in distilled water for 1 min and subsequently dried under flowing N₂ gas and (b) cleaned by hot rinsing at 90°C using distilled water for 1 min and subsequently dried under flowing N₂ gas.

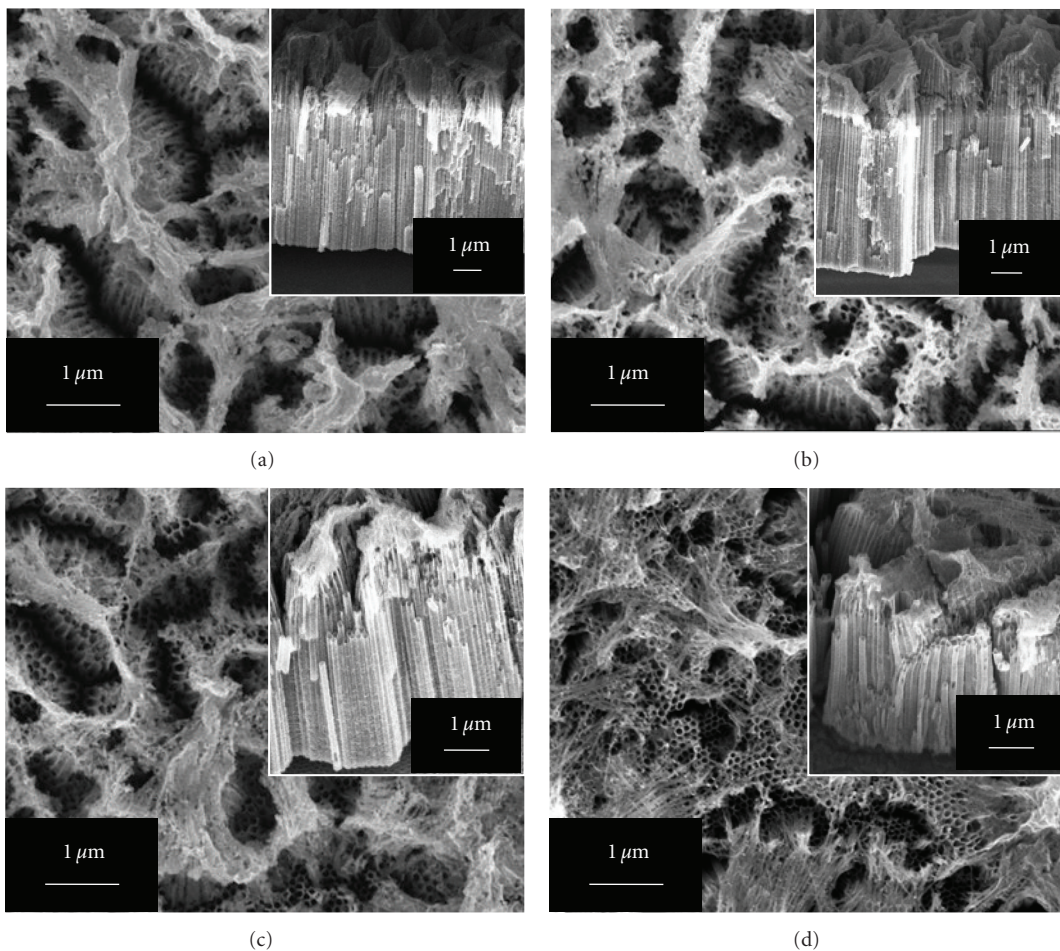


FIGURE 8: FESEM images of TiO₂ nanotubes obtained via chemical etching using 2% HF after anodization for (a) 10, (b) 15, (c) 20, and (d) 60 s.

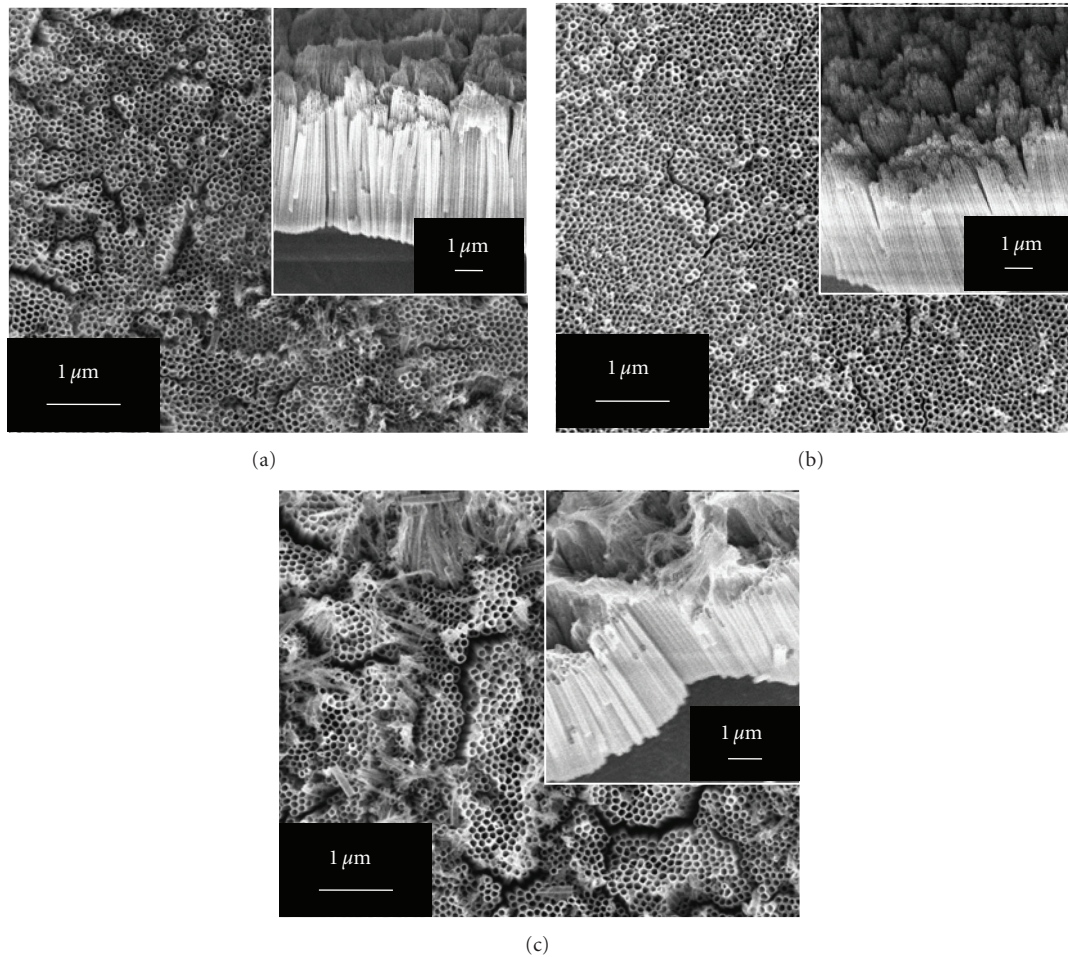


FIGURE 9: FESEM images of TiO_2 nanotubes obtained via ultrasonic cleaning using acetone after anodization for (a) 1, (b) 2, and (c) 10 min.

stress between the adjacent nanotube arrays, resulting in bundle-free and crack-free TiO_2 nanotube arrays as compared with the sample cleaned in distilled water. Acetone is a fast-evaporating cleaning detergent solution with lower surface tension and an inherent cleaning property, which results in the superior microcleaning of the nanotube surface.

3.3. PEC Response on TiO_2 Nanotube Fabricated at Different Anodization Temperatures. The variation of photocurrent responses as a function of applied potentials (I - V characteristics) for TiO_2 fabricated at different anodization temperatures was evaluated under illumination, as shown in Figure 10. Based on the previous part of the experiment, anodization temperature significantly affects the tube length, pore diameter, and wall thickness of nanotubes. The high-ordered TiO_2 nanotube arrays without morphological disorder, bundling, and microcrack problems can significantly enhance the transport properties and reduce the recombination of charge carriers (e^-/h^+), which extends the residence time of electrons [20]. Therefore, studying the different surface morphologies of clean TiO_2 nanotubes under different anodization temperatures on the PEC response is very important.

The initial chemical potential of electrons in a semiconductor and an electrolyte is determined through the Fermi energy of the semiconductor and the redox potential of the redox couples in the electrolyte, respectively. When a TiO_2 photoanode is submerged in the electrolyte, the initial chemical potential of the electrons is different for the two phases. Charge redistribution between TiO_2 and solution is required to equilibrate the two phases; hence, a space charge layer (depletion layer) will form in the TiO_2 adjacent to the electrolyte. For tube-shaped n -type TiO_2 semiconductor, majority of the photoinduced charge carriers (e^-/h^+) are generated at both sides of the tube walls and the entire tube sidewalls, which consist of space charge layers. Theoretically, the space charge layer is necessarily close to the tube wall to generate the photocurrent under illumination [25, 34]. The photoinduced electrons in this space charge layer transfer from the TiO_2 nanotubes photoanode will migrate towards the bulk of the TiO_2 and eventually these photoinduced electrons move to counterelectrode (Pt) with an external bias, while the photoinduced holes move to the electrolyte under illumination. This situation will cause the valence and conduction bands to move relatively to the Fermi level (bend upwards) by an illumination of energy greater than the

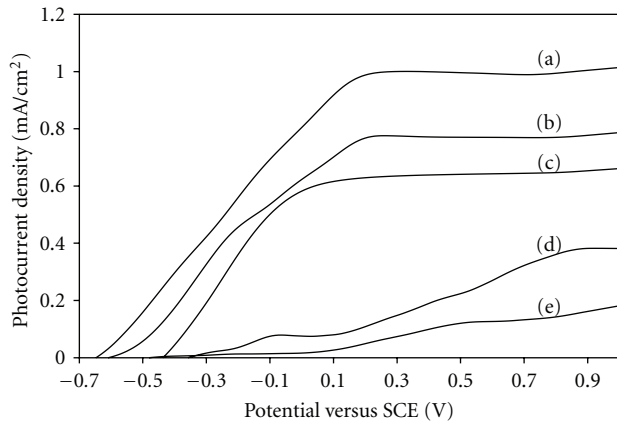


FIGURE 10: I - V characteristics of TiO_2 nanotubes under light-on condition at (a) room temperature, (b) 40, (c) 60, (d) 10, and (e) 80°C anodization temperatures.

band gap of TiO_2 nanotubes photoanode [35]. In this case, an electric field will be generated and, therefore, potential barriers will form along the inner and outer surfaces of the nanotubes [25, 34–37].

The current density was approximately 10^{-7} A to 10^{-6} A in the dark condition for the entire sample. However, the photocurrent density increased under illumination. Therefore, TiO_2 nanotubes can act well as a representative n -type semiconductors for the transfer and decay of the photoinduced electrons under light pulse illumination. The wall thickness of the sample fabricated at room temperature showed the highest photocurrent density throughout the potential window. This result suggests an efficient charge separation. The photocurrent reached a high value of 1 mA/cm², whereas samples fabricated at 40, 60, 10, and 80°C showed a decreased photocurrent density of approximately 0.7, 0.6, 0.3, and 0.1 mA/cm², respectively. The highest photocurrent density, 1 mA/cm², indicates that the width of space charge layer is near to the wall thickness of the nanotube (~ 12.5 nm). Therefore, this sample effectively generates more photoinduced electrons transfer to the counterelectrode and has a great tendency to reduce the recombination of charge carriers (e^-/h^+). However, samples with thicker tube walls produced at 40 and 60°C exhibited poor photocurrent density. This result indicates that wall thickness is significantly larger than the width of the space charge layer, which may be attributed to the transfers of photoinduced electrons to the counterelectrode (Pt) and the photoinduced holes to the surface of TiO_2 nanotubes photoanode were hindered due to the longer path to cross and these charge carriers will recombine readily. Thus, poor PEC performance exhibited due to the less of photoinduced electrons for reduction reaction and less of photoinduced holes for the oxidation of electrolyte species. In addition, the length of the nanotube is another important factor in controlling its PEC performance. Poor photoresponses were recorded for the short TiO_2 nanotubes (5.8 μm) produced at 10°C, which have an irregular TiO_2 oxide layer with a thickness of 0.3 μm . Shorter nanotubes and oxide layers have less effective

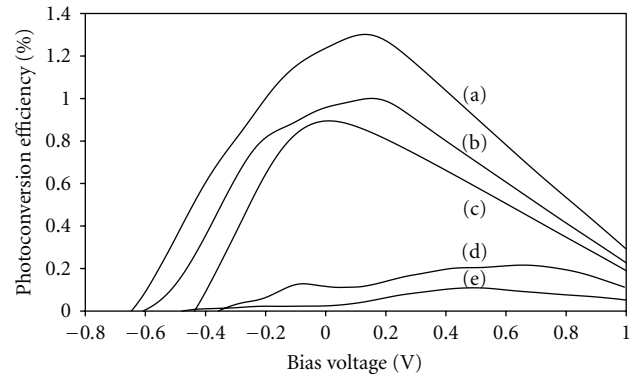


FIGURE 11: Corresponding photoconversion efficiencies of TiO_2 nanotubes at (a) room temperature, (b) 40, (c) 60, (d) 10, and (e) 80°C anodization temperatures.

surface areas for light (photon) absorption, which definitely limits the chemical reactions that allow the photocurrent to generate [38–40]. In summary, these results clearly imply that wall thickness and nanotube length play important roles in enhancing the migration of photoinduced electrons to the counterelectrode (Pt) through external circuit for reduction reaction and thus influence PEC performance.

The photoconversion efficiency (η) for the water splitting reaction was calculated based on the two-electrode configuration. The main reason is because of the applied bias voltage is versus the counterelectrode and not the reference electrode. Thus, the second half-reaction of water splitting process occurring at the counterelectrode is included in the two electrode configuration photoconversion efficiency [26, 27]. Figure 11 shows that the maximum photoconversion efficiency is obtained from the sample produced at room temperature was 1.3%, followed by the photoconversion efficiency of 1.1%, 0.9%, 0.2%, and 0.1% obtained at 40, 60, 10, and 80°C anodization temperatures, respectively. Such differences in photocurrent and photoconversion efficiencies reflect the overall photoelectron efficiency in generation, separation, and transport for the sample fabricated in different anodization temperatures with different surface morphologies.

4. Conclusion

Self-organized TiO_2 nanotube arrays were successfully synthesized from a low temperature of 10°C to a high temperature of 60°C in EG electrolyte containing 5 wt% NH_4F and 5 wt% H_2O_2 at 60 V for 1 h. Nanoporous TiO_2 favors temperatures beyond 80°C. Based on the result obtained, anodization temperature significantly affects the wall thickness, length, and pore size. The length of the tubes decreased, whereas its wall thickness increased when synthesized at low and high temperatures. Furthermore, approximately 1 or 2 min of ultrasonic agitation in acetone is effective in removing overlayers on the nanotubes. This process results in the formation of bundle-free and crack-free TiO_2 nanotube arrays. In addition, the thin wall and higher length of the

TiO₂ nanotube arrays fabricated at room temperature exhibit the highest photocurrent density at 1 mA/cm², with a maximum photoconversion efficiency of 1.3%. This result is due to the effective transfer of photoinduced electrons to the counterelectrode (Pt) with an external bias, which has a great tendency to reduce the recombination of charge carriers (e⁻/h⁺) at the thin walls of the nanotubes.

Acknowledgments

The author would like to thank Universiti Sains Malaysia for sponsoring this work under RU grant 814075, PRGS grant 8044058, FRGS grant 6071213, Fellowship USM and Research University Postgraduate Research Grant Scheme, 80430146.

References

- [1] M. Kitano, M. Matsuoka, M. Ueshima, and M. Anpo, "Recent developments in titanium oxide-based photocatalysts," *Applied Catalysis A*, vol. 325, no. 1, pp. 1–14, 2007.
- [2] M. Grätzel, "Dye-sensitized solar cells," *Journal of Photochemistry and Photobiology C*, vol. 4, no. 2, pp. 145–153, 2003.
- [3] V. M. Aroutiounian, V. M. Arakelyan, and G. E. Shahnazaryan, "Metal oxide photoelectrodes for hydrogen generation using solar radiation-driven water splitting," *Solar Energy*, vol. 78, no. 5, pp. 581–590, 2005.
- [4] E. Y. Kim, J. H. Park, and G. Y. Han, "Design of TiO₂ nanotube array-based water-splitting reactor for hydrogen generation," *Journal of Power Sources*, vol. 184, no. 1, pp. 284–287, 2008.
- [5] G.-J. Wang, G.-Y. Chen, and M.-W. Lee, "Fabrication of dye-sensitized solar cells with a 3D nanostructured electrode," *International Journal of Photoenergy*, vol. 2010, Article ID 585621, 7 pages, 2010.
- [6] S. K. Mohapatra, M. Misra, V. K. Mahajan, and K. S. Raja, "A novel method for the synthesis of titania nanotubes using sonoelectrochemical method and its application for photoelectrochemical splitting of water," *Journal of Catalysis*, vol. 246, no. 2, pp. 362–369, 2007.
- [7] S.-J. Kim, N.-H. Lee, H.-J. Oh, S.-C. Jung, W.-J. Lee, and D.-H. Kim, "Photocatalytic properties of nanotubular-shaped TiO₂ powders with anatase phase obtained from titanate nanotube powder through various thermal treatments," *International Journal of Photoenergy*, vol. 2011, Article ID 327821, 7 pages, 2011.
- [8] S. Kim, S. J. Hwang, and W. Choi, "Visible light active platinum-ion-doped TiO₂ photocatalyst," *Journal of Physical Chemistry B*, vol. 109, no. 51, pp. 24260–24267, 2005.
- [9] M. Paulose, H. E. Prakasham, O. K. Varghese et al., "TiO₂ nanotube arrays of 1000 μm length by anodization of titanium foil: Phenol red diffusion," *Journal of Physical Chemistry C*, vol. 111, no. 41, pp. 14992–14997, 2007.
- [10] M. Anpo and M. Takeuchi, "The design and development of highly reactive titanium oxide photocatalysts operating under visible light irradiation," *Journal of Catalysis*, vol. 216, no. 1–2, pp. 505–516, 2003.
- [11] M. Ni, M. K. H. Leung, D. Y. C. Leung, and K. Sumathy, "A review and recent developments in photocatalytic water-splitting using TiO₂ for hydrogen production," *Renewable and Sustainable Energy Reviews*, vol. 11, no. 3, pp. 401–425, 2007.
- [12] D. Wang, Y. Liu, B. Yu, F. Zhou, and W. Liu, "TiO₂ nanotubes with tunable morphology, diameter, and length: synthesis and photo-electrical/catalytic performance," *Chemistry of Materials*, vol. 21, no. 7, pp. 1198–1206, 2009.
- [13] C. Trapalis, N. Todorova, T. Giannakopoulou, G. Romanos, T. Vaimakis, and J. Yu, "Preparation of fluorine-doped TiO₂ photocatalysts with controlled crystalline structure," *International Journal of Photoenergy*, vol. 2008, Article ID 534038, 9 pages, 2008.
- [14] K. Yasuda, J. M. Macak, S. Berger, A. Ghicov, and P. Schmuki, "Mechanistic aspects of the self-organization process for oxide nanotube formation on valve metals," *Journal of the Electrochemical Society*, vol. 154, no. 9, pp. C472–C478, 2007.
- [15] S. Sreekantan, L. C. Wei, and Z. Lockman, "Extremely fast growth rate of TiO₂ nanotube arrays in electrochemical bath containing H₂O₂," *Journal of the Electrochemical Society*, vol. 158, no. 12, pp. C397–C402, 2011.
- [16] J. M. Macak and P. Schmuki, "Anodic growth of self-organized anodic TiO₂ nanotubes in viscous electrolytes," *Electrochimica Acta*, vol. 52, no. 3, pp. 1258–1264, 2006.
- [17] G. K. Mor, K. Shankar, M. Paulose, O. K. Varghese, and C. A. Grimes, "Enhanced photocleavage of water using titania nanotube arrays," *Nano Letters*, vol. 5, no. 1, pp. 191–195, 2005.
- [18] J. Wang and Z. Lin, "Anodic formation of ordered TiO₂ nanotube arrays: effects of electrolyte temperature and anodization potential," *Journal of Physical Chemistry C*, vol. 113, no. 10, pp. 4026–4030, 2009.
- [19] X. Chen, J. Chen, and J. Lin, "Self-assembled TiO₂ nanotube arrays with U-shaped profile by controlling anodization temperature," *Journal of Nanomaterials*, vol. 2010, Article ID 753253, 4 pages, 2010.
- [20] K. Zhu, T. B. Vinzant, N. R. Neale, and A. J. Frank, "Removing structural disorder from oriented TiO₂ nanotube arrays: reducing the dimensionality of transport and recombination in dye-sensitized solar cells," *Nano Letters*, vol. 7, no. 12, pp. 3739–3746, 2007.
- [21] D. Kim, A. Ghicov, and P. Schmuki, "TiO₂ Nanotube arrays: elimination of disordered top layers ("nanograss") for improved photoconversion efficiency in dye-sensitized solar cells," *Electrochemistry Communications*, vol. 10, no. 12, pp. 1835–1838, 2008.
- [22] G. K. Mor, M. A. Carvalho, O. K. Varghese, M. V. Pishko, and C. A. Grimes, "A room-temperature TiO₂-nanotube hydrogen sensor able to self-clean photoactively from environmental contamination," *Journal of Materials Research*, vol. 19, no. 2, pp. 628–634, 2004.
- [23] Y. Liu, J. Li, B. Zhou et al., "Comparison of photoelectrochemical properties of TiO₂-nanotube-array photoanode prepared by anodization in different electrolyte," *Environmental Chemistry Letters*, vol. 7, no. 4, pp. 363–368, 2009.
- [24] K. Kant and D. Losic, "A simple approach for synthesis of TiO₂ nanotubes with through-hole morphology," *Physica Status Solidi—Rapid Research Letters*, vol. 3, no. 5, pp. 139–141, 2009.
- [25] L. Sun, S. Zhang, X. Sun, and X. He, "Effect of the geometry of the anodized titania nanotube array on the performance of dye-sensitized solar cells," *Journal of Nanoscience and Nanotechnology*, vol. 10, no. 7, pp. 4551–4561, 2010.
- [26] A. B. Murphy, P. R. F. Barnes, L. K. Randeniya et al., "Efficiency of solar water splitting using semiconductor electrodes," *International Journal of Hydrogen Energy*, vol. 31, no. 14, pp. 1999–2017, 2006.
- [27] Z. Chen, T. F. Jaramillo, T. G. Deutsch et al., "Accelerating materials development for photoelectrochemical hydrogen production: standards for methods, definitions, and reporting protocols," *Journal of Materials Research*, vol. 25, no. 1, pp. 3–16, 2010.

- [28] K. Shankar, G. K. Mor, M. Paulose, O. K. Varghese, and C. A. Grimes, "Effect of device geometry on the performance of TiO_2 nanotube array-organic semiconductor double heterojunction solar cells," *Journal of Non-Crystalline Solids*, vol. 354, no. 19–25, pp. 2767–2771, 2008.
- [29] N. K. Allam, K. Shankar, and C. A. Grimes, "Photoelectrochemical and water photoelectrolysis properties of ordered TiO_2 nanotubes fabricated by Ti anodization in fluoride-free HCl electrolytes," *Journal of Materials Chemistry*, vol. 18, no. 20, pp. 2341–2348, 2008.
- [30] S. Li, G. Zhang, D. Guo, L. Yu, and W. Zhang, "Anodization fabrication of highly ordered TiO_2 nanotubes," *Journal of Physical Chemistry C*, vol. 113, no. 29, pp. 12759–12765, 2009.
- [31] H. Xu, Q. Zhang, C. Zheng, W. Yan, and W. Chu, "Application of ultrasonic wave to clean the surface of the TiO_2 nanotubes prepared by the electrochemical anodization," *Applied Surface Science*, vol. 257, no. 20, pp. 8478–8480, 2011.
- [32] Y. K. Oh, S. H. Park, and Y. I. Cho, "A study of the effect of ultrasonic vibrations on phase-change heat transfer," *International Journal of Heat and Mass Transfer*, vol. 45, no. 23, pp. 4631–4641, 2002.
- [33] H. Feng, G. Barbosa-Canovas, and J. Weiss, *Ultrasound Technologies for Food and Bioprocessing*, Springer, Berlin, Germany, 2011.
- [34] A. Ghicov and P. Schmuki, "Self-ordering electrochemistry: a review on growth and functionality of TiO_2 nanotubes and other self-aligned MO_x structures," *Chemical Communications*, no. 20, pp. 2791–2808, 2009.
- [35] M. Grätzel, "Photoelectrochemical cells," *Nature*, vol. 414, no. 6861, pp. 338–344, 2001.
- [36] C. A. Grimes, "Synthesis and application of highly ordered arrays of TiO_2 nanotubes," *Journal of Materials Chemistry*, vol. 17, no. 15, pp. 1451–1457, 2007.
- [37] Y. Xie, L. Zhou, and J. Lu, "Photoelectrochemical behavior of titania nanotube array grown on nanocrystalline titanium," *Journal of Materials Science*, vol. 44, no. 11, pp. 2907–2915, 2009.
- [38] S. Yeonmi and L. Seonghoon, "Self-organized regular arrays of anodic TiO_2 nanotubes," *Nano Letters*, vol. 8, no. 10, pp. 3171–3173, 2008.
- [39] C. W. Lai and S. Sreekantan, "Effect of applied potential on the formation of self-organized TiO_2 nanotube arrays and its photoelectrochemical response," *Journal of Nanomaterials*, vol. 2011, Article ID 142463, 7 pages, 2011.
- [40] M. Paulose, G. K. Mor, O. K. Varghese, K. Shankar, and C. A. Grimes, "Visible light photoelectrochemical and water-photoelectrolysis properties of titania nanotube arrays," *Journal of Photochemistry and Photobiology A*, vol. 178, no. 1, pp. 8–15, 2006.

Research Article

CdSe Quantum Dots for Solar Cell Devices

A. B. Kashyout,¹ Hesham M. A. Soliman,¹ Marwa Fathy,¹ E. A. Gomaa,² and Ali A. Zidan¹

¹ Advanced Technology and New Materials Research Institute, City of Scientific Research and Technological Applications, New Borg El-Arab City, Alexandria 21934, Egypt

² Department of Chemistry, Faculty of Science, Mansoura University, Mansoura 35516, Egypt

Correspondence should be addressed to A. B. Kashyout, hady8@yahoo.com

Received 6 January 2012; Accepted 6 February 2012

Academic Editor: Mohamed Sabry Abdel-Mottaleb

Copyright © 2012 A. B. Kashyout et al. This is an open access article distributed under the Creative Commons Attribution License, which permits unrestricted use, distribution, and reproduction in any medium, provided the original work is properly cited.

CdSe quantum dots have been prepared with different sizes and exploited as inorganic dye to sensitize a wide bandgap TiO₂ thin films for QDs solar cells. The synthesis is based on the pyrolysis of organometallic reagents by injection into a hot coordinating solvent. This provides temporally discrete nucleation and permits controlled growth of macroscopic quantities of nanocrystallites. XRD, HRTEM, UV-visible, and PL were used to characterize the synthesized quantum dots. The results showed CdSe quantum dots with sizes ranging from 3 nm to 6 nm which enabled the control of the optical properties and consequently the solar cell performance. Solar cell of 0.08% performance under solar irradiation with a light intensity of 100 mW/cm² has been obtained. CdSe/TiO₂ solar cells without and with using mercaptopropionic acid (MPA) as a linker between CdSe and TiO₂ particles despite a V_{oc} of 428 mV, J_{sc} of 0.184 mAcm⁻², FF of 0.57, and η of 0.05% but with linker despite a V_{oc} of 543 mV, J_{sc} of 0.318 mAcm⁻², FF of 0.48, and η of 0.08%, respectively.

1. Introduction

Nanocrystals or quantum dots (QDs) are currently a subject of intense research activity targeting a wide range of potential applications, including light-emitting diodes (LEDs) [1, 2], photovoltaics [3, 4], single-electron transistors [5], and fluorescent tags for biological imaging [6, 7]. The utility of nanocrystals lies in their unique size-dependent optical and electronic properties, chiefly a size-tunable optical absorption and emission spectra [8]. According to these unique properties, the recent interest in utilizing semiconductor nanocrystals (or quantum dots) for harvesting light energy has drawn great attention toward metal-chalcogenide-based system [4, 9]. Of particular interest are CdX and PbX (X = S, Se, and Te) QDs, which have relatively small bandgaps and thus are capable of harvesting photons in the visible and infrared region [10]. These materials have been employed in three different types of quantum dot solar cells [11]: (i) metal junction solar cells, (ii) polymer hybrid solar cells, and (iii) quantum dot-sensitized solar cells (QDSCs). In the metal junction solar cells, charge separation is achieved at metal semiconductor interface upon visible laser excitation. The polymer hybrid solar cells utilize blends of conducting

polymers (e.g., poly(3-hexylthiophene)) and QDs to facilitate charge separation and charge transport. In the case of the QDSCs, excited electrons of semiconductor nanocrystals are injected into a large bandgap semiconductor such as TiO₂ or ZnO, and holes are scavenged by a redox couple [4].

Research on the preparation of the QDs concentrates on the syntheses and characterizations of the monodisperse QDs, especially the studies of nucleation and growth mechanisms as well as the improvement of the luminescence quantum yields (QY). The most popular route to synthesize CdSe quantum dots is the method using organometallic compounds [12]: dimethylcadmium ((CH₃)₂Cd) reacts with a selenium reagent in the presence of trioctylphosphine oxide (TOPO) surfactant at high temperature (300°C). Careful control of reaction conditions produces CdSe quantum dots that are quite homogeneous in size and tunable in size from 2 to 8 nm. However, ((CH₃)₂Cd) is extremely toxic, pyrophoric, unstable at room temperature, and explosive at elevated temperatures by releasing large amounts of gas. Because of these reasons, the (CH₃)₂Cd-related schemes require very restricted equipments and conditions and are not suitable for large-scale synthesis. In a recent development, Z. A. Peng and X. Peng [13] reported

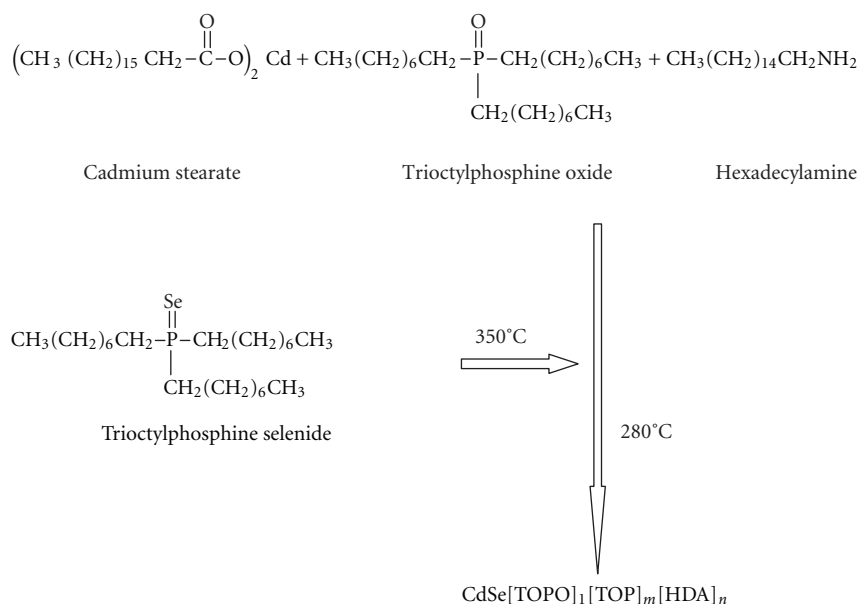


FIGURE 1: Scheme for the preparation reaction of CdSe QDs.

the use of less toxic and reactive cadmium oxide (CdO) with hexylphosphonic acid (HPA) or tetradecylphosphonic acid (TDPA), as an alternative to $(\text{CH}_3)_2\text{Cd}$ in TOPO syntheses of CdX.

In this paper, we chose different reagents as reaction media and low-toxic, air-stable inorganic reagents as precursors to synthesize CdSe QDs such as CdO instead of dimethyl cadmium and study the effect of solvent (TOPO & TOP) and the ratio of CdO to Se on the growth and the yield of QDs. Then use these CdSe QDs as sensitizer for TiO_2 nanoparticles prepared by Kashyout et al. 2010 [14]. TiO_2 films prepared by doctor-blade technique on ITO ($14\ \Omega/\square$)/glass that prepared by Kashyout et al. 2011 [15] using sputtering technique. QDs linked to TiO_2 film by using 3-mercaptopropionic acid as a linker [16].

2. Materials and Methods

2.1. Materials. Cadmium oxide CdO (99.5%, Alfa), selenium powder Se (99%, Alfa Aesar), trioctylphosphine (TOP) (99%, Aldrich), trioctylphosphine oxide (TOPO) (99%, Aldrich), hexadecylamine (HDA) (99%, Aldrich), Stearic acid (SA) (99.5%, Aldrich), and 3-mercaptopropionic acid (MPA) (99%, Alfa Aesar).

2.2. Methods

2.2.1. Preparation of CdSe QDs. This reaction procedure was originally reported by Z. A. Peng and X. Peng [13]. Figure 1 shows scheme for the preparation reaction of CdSe QDs. Se injection solution was prepared under nitrogen by mixing Se powder and TOP in a scintillation vial, which was capped by a rubber septum and fixed with two turns of Cu wire. After ~30 min of heating (~150°C, on a hot plate) and vigorously

stirring with a PTFE stir bar, the suspended Se became soluble to afford a light-yellow solution. The Se solution is allowed to cool to room temperature in the presence of nitrogen gas instead of air before injection into a heated Cd solution.

In a laminar flow hood, CdO and SA were loaded into a 3-neck round-bottom flask. The reaction flask is heated to 150°C in air with a round bottom heating mantle. After ~30 min, the reddish-brown slurry became optically clear indicating formation of cadmium stearate. To the hot reaction vessel, HDA and TOPO were added. The reaction flask was backfilled with N_2 and heated to 320°C. At this temperature, the selenium solution was swiftly injected into the reaction flask.

Upon injection, the solution temperature dropped to 280°C. The solution was maintained at 280°C for the desired amount of time to reach the desired NC size. The round-bottom flask was then removed from the heating mantle and quickly cooled to ~70°C. CdSe QDs washed more than three times by using ethanol and acetone.

Table 1 illustrates the different preparation parameters, which are used for the preparation of CdSe QDs.

2.2.2. Preparation of TiO_2 Thin Films. The ITO/glass which is used as current collector ($14\ \Omega/\square$) [15] was first cleaned in water and then acetone using an ultrasonic bath for 15 min. A layer of TiO_2 paste was coated on the ITO glass plates by spinner coating method (wafer spinner machine (100 rpm, 2 min)), then allowed to dry in air and followed by heat treatment at 450°C for 30 min. This procedure with TiO_2 paste (coating, drying, and heat treatment) was repeated to get the appropriate thickness of about 10 μm for the working electrode.

TABLE 1: Different preparation parameters used for the preparation of CdSe QDs.

Sample no.	CdO (gm)	Se (gm)	TOPO (gm)	TOP (mL)	HAD (gm)	SA (gm)	Reaction time (sec.)
S1	0.0829	0.051	9.83	6.25	9.73	0.8974	60
S2	0.0829	0.051	9.83	6.25	9.73	0.8974	40
S3	0.0829	0.051	9.83	6.25	9.73	0.8974	20
S4	0.0829	0.051	9.83	6.25	9.73	0.8974	10
S5	0.0829	0.051	10	10	9.73	0.8974	60
S6	0.0829	0.051	15	10	9.73	0.8974	60
S7	0.0829	0.051	5	10	9.73	0.8974	60
S8	0.0829	0.102	10	10	9.73	0.8974	60
S9	0.0829	0.153	10	10	9.73	0.8974	60
S10	0.0829	0.255	10	10	9.73	0.8974	60
S11	0.0829	0.357	10	10	9.73	0.8974	60

2.2.3. Preparation of CdSe QDs/TiO₂ Films. TiO₂ thin films were dipped into a solution of N₂ purged acetonitrile containing carboxyalkanethiol such as 3-mercaptopropionic acid (1 : 10 ratio) for 24 hrs. Resulting TiO₂ films, functionalized with these bifunctional surface modifiers, were washed with both acetonitrile and toluene and then immersed in a suspension of CdSe solution for 24 hrs [17].

2.2.4. Fabrication of QDs/TiO₂ Solar Cells. The counter electrode was placed directly on the top of the QDs/TiO₂ film, supported by the conducting glass sheet. Both electrodes were clamped tightly together. Drops of electrolyte (0.5 M LiI/50 mM I₂ in solvent of 3-methoxypropionitrile) and 0.5 M 4-*tert*-butylpyridine were added to the standard electrolyte solution in order to increase the stability of the electrolyte. The QDs/TiO₂ film was illuminated through the conducting glass substrate to measure the cell performance.

2.2.5. Characterization of CdSe QDs. The structural properties of these organic species were confirmed by the powder X-ray diffraction (XRD) using (Shimadzu 7000, Japan) diffractometer, operating with Cu K α radiation ($\lambda = 0.15406$ nm) generated at 30 kV and 30 mA. Scans were done at 4° min⁻¹ for 2 θ values between 20 and 60°. The morphologies and the crystallite size of TiO₂ nanoparticles were observed by high-resolution transmission electron microscopy (HRTEM) (JEOLJEM-2100F, Japan). To identify and characterize the organic species on the surfaces, the Fourier transform infrared spectroscopy (FT-IR) spectra were obtained using a Shimadzu FTIR-8400 S, Japan. The absorption spectra and their photoluminescence properties were characterized by means of LABOMED double-beam UV-Vis spectrophotometer with spectrum range from 190 to 1100 nm and using a Varian Cary Eclipse spectrofluorometer.

2.2.6. Characterization of QDs/TiO₂ Solar Cells. The QDs/TiO₂ solar cell performance was measured using solar simulator device (PET Photo Emission Tech., Inc., USA). The solar simulator simulates the AM1.5 spectrum by using xenon lamp, and the light intensity could be controlled from

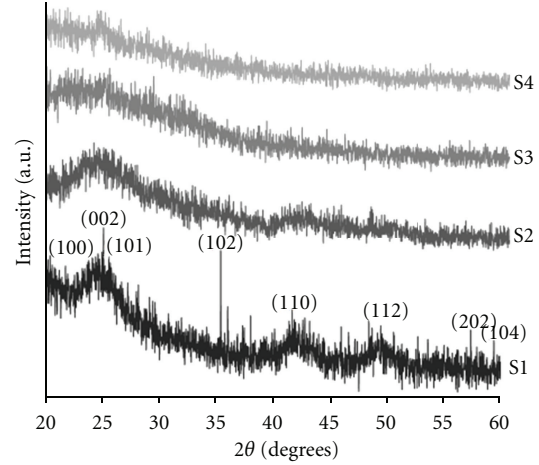


FIGURE 2: XRD spectra of CdSe samples using different growth rate.

TABLE 2: Effect of TOPO/TOP ratio on the CdSe QDs yield.

Sample	TOP (mL)	TOPO (gm)	Yield (gm)	Yield (%)
S5	10	10	0.14	29
S6	15	10	0.13	27
S7	5	10	0.12	25

0.1 Sun to 1.25 Sun. The cell ambient temperature was controlled at 25°C using a control system attached to the solar simulator.

3. Results and Discussion

3.1. Structural Analysis. Figure 2 (S1, S2, S3, and S4) shows the XRD of CdSe quantum dots with different growth rates as shown in Table 1. The XRD spectra of S1 and S2 exhibit clear peaks that confirm the wurtzite structure with (100), (002), (101), (102), (110), (112), (202), and (104) planes according to the JCPD no. 08-0456, but, for S3 and S4, it gives amorphous structure, which mean that, when the particle size became small, the sample loses its crystalline structure and transfers into amorphous structure.

The crystallite size of different samples can be determined from the broadening of corresponding X-ray spectral peaks by the Scherrer formula:

$$L = \frac{K\lambda}{(\beta \cos \theta)}, \quad (1)$$

where L is the crystallite size, λ is the wavelength of the X-ray radiation (Cu K α = 0.15418 nm), K is usually taken as 0.89, and β is the line width at half-maximum height, after subtraction of equipment broadening. It was found that the crystallite size value of S1 and S2, is 4.5 and 4, respectively.

Table 2 illustrates the effect of using different TOPO/TOP (wt/vol) ratio on the growth rate of the CdSe QDs. It was found that the growth rate of particles was decreased as the ratio of TOPO/TOP increases. Figure 3 shows the absorbance curve of different CdSe samples (S5, S6, and S7) prepared using different TOPO/TOP ratio. It was found

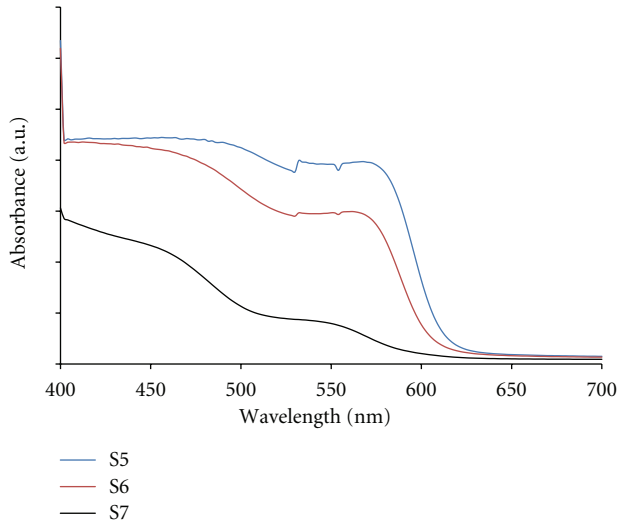


FIGURE 3: Absorbance spectra of CdS QDs prepared using different TOPO/TOP ratio.

TABLE 3: Effect of CdO/Se molar ratio on the CdSe stoichiometry and QDs yield.

Samples	CdO : Se ratio	Cd : Se atomic ratio	Yield (gm)	Yield (%)
S8	1 : 1	1.27	0.12	25
S9	1 : 3	1.42	0.13	27
S10	1 : 5	1.32	0.13	27
S11	1 : 7	—	No reaction	No reaction

that the absorbance peak for samples S5, S6, and S7 was shifted to lower value of wavelength with decrease of the particle growth rate.

Table 3 illustrates the effect of using different CdO/Se molar ratios on the stoichiometry of CdSe QDs using the TOPO/TOP ratio value of 1 : 1. It is found that the atomic ratio of Cd/Se is 1.27, 1.42, and 1.32 for CdO/Se ratios of 1 : 1, 1 : 3, and 1 : 5, respectively. When increasing the CdO/Se ratio to 1 : 7, no reaction was occurred. This result indicates that controlling the Cd/Se ratio in the precursors affects the quantum dot chemicals properties with a small effect on their yield.

Energy dispersive X-ray analysis (EDX) indicates that the quantum dots are nonstoichiometric, showing a molar ratio of Cd/Se about 1.27 (sample S8) in Table 2. This result is similar to the data previously reported by other authors such as Moreels et al. [18] and Taylor et al. [19] who found similar ratios between the metal M (Cd) and the counterion X (Se) in analogous systems for the PbSe QDs. Owen et al. [20] proposed a sphere-like structure for these materials, in which Cd^{2+} ions are present on the QDs surface, which justifies the nonstoichiometry so that metal ions can easily interact with the molecules of a ligand shell by coordination [21].

3.2. Morphological Analysis. HRTEM reveals information about the particle size and shape. Figure 4 shows the HRTEM images of the S1 example for CdSe quantum dots before

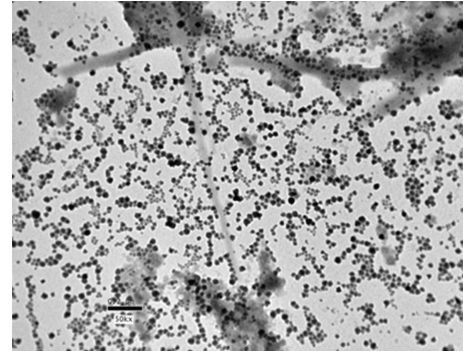
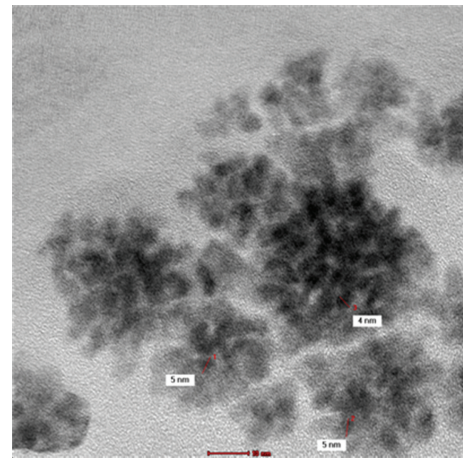
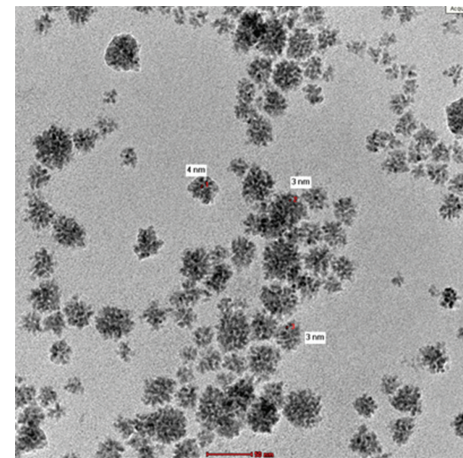


FIGURE 4: HRTEM images of CdSe QDs without purification.



(a)



(b)

FIGURE 5: HRTEM images of CdSe QDs after purification.

purification from the excess of ligands. CdSe quantum dots are collected on the surface of large chain ligands.

The concentration of the nanocrystals in samples were determined by the number of cadmium atoms contained in the samples and the size of the nearly monodisperse particles. Therefore, it was critical to remove any unreacted cadmium precursors in the sample. The extraction method

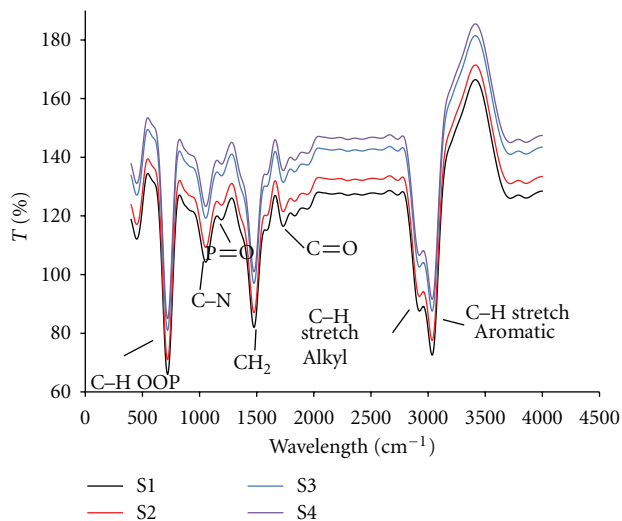


FIGURE 6: FT-IR spectra of CdSe QDs soluble in toluene.

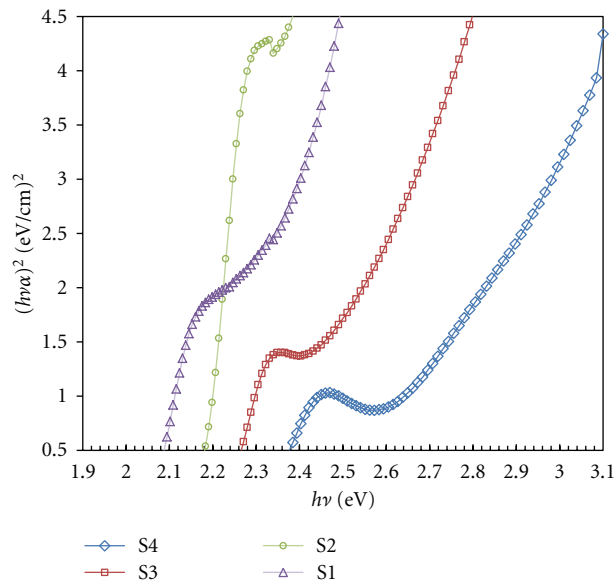


FIGURE 8: Bandgap of CdSe samples.

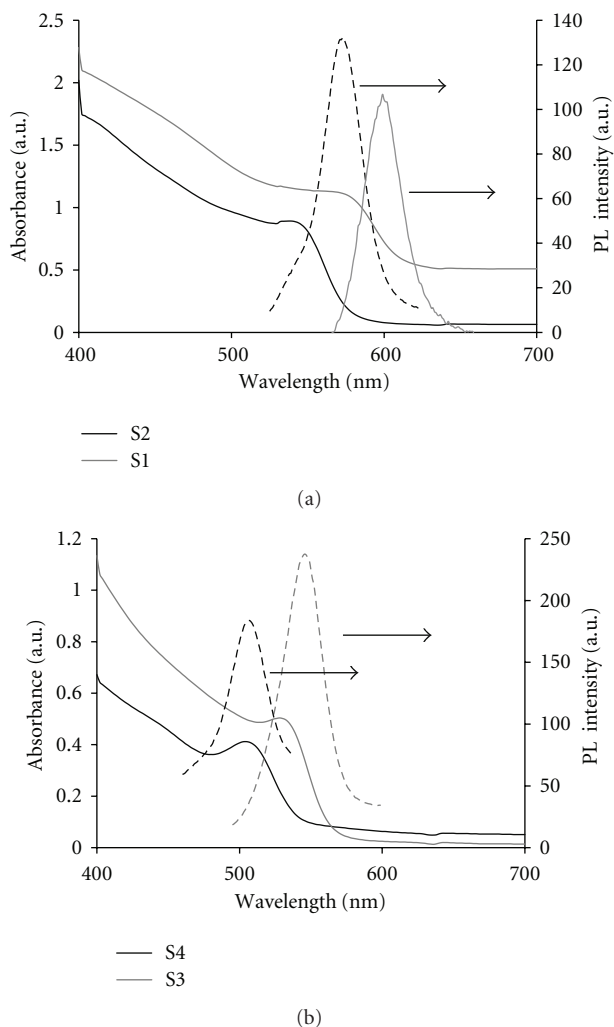


FIGURE 7: UV-Vis and photoluminescence spectra of the representative nanocrystalline samples.

is based on the fact that the solubilities of the un-reacted cadmium precursors used in the synthesis and the resulting nanocrystals were significantly different in a two-phase system, ethanol and octadecane.

Figure 5 shows the HRTEM images of CdSe powder after purification. The particle size was determined to have value of 2–4 nm. These are consistent with the result of X-ray diffraction spectrum. Also, the nanocrystals were dispersed well, and no aggregation was detected.

Figure 6 shows the FT-IR spectra of S1, S2, S3, and S4. CdSe QDs are soluble in toluene after purification. On the basis of the FT-IR data, the surface of the CdSe QDs is mainly coated with alkyl ligands. Flexible organic molecule such as phosphine alkyl ligands provides repulsive interactions between the QDs in toluene, thus preventing aggregation. Others show 3417 cm^{-1} at OH, 2360 cm^{-1} at PH₃, 1464 cm^{-1} at CH₂, 1155 cm^{-1} at P=O functional group [22].

3.3. Optical Analysis of CdSe QDs. Figure 7 shows the absorption and photoluminescence (PL) spectra (410 nm excitation) for different size of CdSe QDs (S1, S2, S3, and S4). For the absorption spectra, all CdSe samples clearly show the effect of quantum confinement. These particles exhibit absorption in the visible region with an onset corresponding to the particle size. The shift of the onset absorption peaks to higher wavelengths (506, 530, 543, and 577 nm) with increasing the particle size represents size quantization effects in these particles.

According to the literature, Yu et al., 2003, developed a theoretical method to calculate the QDs size using the position of first excitonic peak. The particle size of the different samples was determined using

$$D = (1.6122 \times 10^{-9})\lambda^4 - (2.6575 \times 10^{-6})\lambda^3 + (1.6242 \times 10^{-3})\lambda^2 - (0.4277)\lambda + (41.57), \quad (2)$$

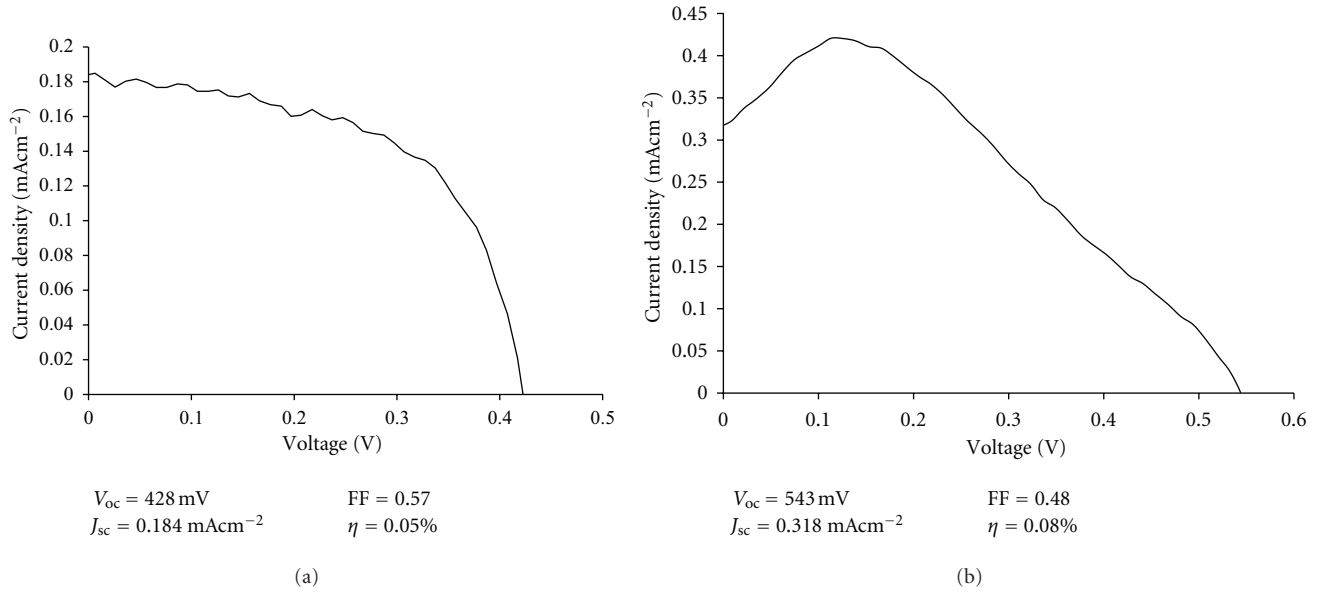


FIGURE 9: I - V curves of CdSe/TiO₂ solar cell, (a) without and (b) with using MPA as a linker between CdSe and TiO₂ particles.

where D (nm) is the size of a given sample and λ (nm) is the wavelength of the first excitonic absorption peak of the corresponding sample. The calculated particle size corresponding to the wavelength of the excitonic peaks was 2.3, 2.9, 3, and 3.7 nm for samples S1, S2, S3, and S4, respectively.

For photoluminescence spectra, CdSe samples with particle size of 2.3, 2.9, 3, and 3.7 nm were given emission peaks at 505, 547, 577, and 600 nm; respectively, it means that the peaks move toward the red end of visible region with the growth temperature which expected according to the literature.

Figure 8 shows the calculated E_g of S1, S2, S3, and S4 of CdSe QDs with different particle size. The band gap was decreased by 2.38, 2.28, 2.18, and 2.08 eV with the particle size increase of 2.3, 2.9, 3, and 3.7 nm, respectively.

The calculated diameter was used to determine the molar absorption (extinction) coefficient (ϵ) using

$$\epsilon = 5857(D)^{2.65}. \quad (3)$$

If the extinction coefficient of those nanocrystals was calculated, it would be easy to obtain the concentrations of the nanocrystals by simply taking an absorption spectrum of the sample and using Lambert-Beer's law

$$A = \epsilon CL, \quad (4)$$

where A is the absorbance at the peak position of the first exciton absorption peak for a given sample. C is the molar concentration (mol/L) of the nanocrystals of the sample. L is the path length (cm) of the radiation beam used for recording the absorption spectrum.

Unlike conventional organic and inorganic compounds, the concentration of colloidal nanocrystals is difficult to determine by gravimetric methods. Because the number of

TABLE 4: Absorbance, particle size, extinction, and the molar concentration of CdSe DQs.

Sample no.	First excitonic peak (nm)	Abs.	Size (nm)	Extinction coeff. (mol ⁻¹ cm ⁻¹ L)	Conc. (mol/L) (10 ⁻⁶)
S1	577	0.6	3.7	81150.43992	3.14
S2	543	0.9	2.9	190860.4584	6.16
S3	530	0.5	2.69	99040.01971	9.08
S4	505	0.4	2.39	59194.80559	6.75

ligands on the surface of nanocrystals is quite difficult to identify and may also vary significantly under different conditions, measurements solely based on gravimetric methods using ligands-coated nanocrystals are accurate only when the interactions between nanocrystals and ligands are sufficiently strong to withstand necessary purification procedures [23]. Therefore, the absorption spectrum method in many cases is the most practical and convenient way to determine the particle concentrations, if it is not the only possible way as shown in Table 4.

3.4. I - V Curve of CdSe/TiO₂ Solar Cell. For the fabricated solar cell using S1 CdSe QD, the efficiency (η) is calculated as $\eta = J_{sc} V_{oc} FF / I_0$, where I_0 is the incident irradiation power, J_{sc} is the short-circuit current density (current density corresponding to $V = 0$), V_{oc} is the open circuit voltage (voltage corresponding to $J_{sc} = 0$), and FF is the fill factor.

Figures 9(a) and 9(b) show the I - V curve of two CdSe QDs/TiO₂ solar cells without and with using of MPA as a linker between two semiconductors (TiO₂ and CdSe) is used to enhance the adsorption of CdSe QDs on the surface of TiO₂ particles and facilitate the charge transfer process from CdSe QDs to TiO₂ which enhances the solar cell efficiency [17]. Simulated AM1.5G solar irradiation with

a light intensity of 100 mW/cm^2 was obtained. It was found, QD solar cell without using linker despite a V_{oc} of 428 mV, J_{sc} of 0.184 mAcm^{-2} , FF of 0.57, and η of 0.05% but with linker despite a V_{oc} of 543 mV, J_{sc} of 0.318 mAcm^{-2} , FF of 0.48, and η of 0.08%.

4. Conclusions

Our results indicate that CdSe nanocrystals prepared by the common pyrolysis method have an average Cd/Se stoichiometry about 1.27 and the stoichiometry is independent on the initial Cd/Se ratio in the starting material. The results also showed CdSe quantum dots with sizes ranging from 3 nm to 6 nm which enabled the control of the optical properties and consequently the solar cell performance. Open-circuit voltage of 0.54 V, short-circuit current density of about 0.5 mA/cm^2 , and high fill factor of 0.57 are obtained, which are good results that should be improved through.

Acknowledgment

This work has been done under the project funded by the Science and Technology Development Fund (STDF), Ministry of Scientific Research, Project ID: 1414, "Quantum Dots Nanomaterials Dye Sensitized Solar Cells".

References

- [1] M. J. Bowers, J. R. McBride, and S. J. Rosenthal, "White-light emission from magic-sized cadmium selenide nanocrystals," *Journal of the American Chemical Society*, vol. 127, no. 44, pp. 15378–15379, 2005.
- [2] G. Mingyuan, C. Lesser, S. Kirstein, E. Möhwald, A. L. Rogach, and H. Weller, "Electroluminescence of different colors from polycation/CdTe nanocrystal self-assembled films," *Journal of Applied Physics*, vol. 87, no. 5, pp. 2297–2302, 2000.
- [3] H. J. Lee, J. H. Yum, H. C. Leventis et al., "CdSe quantum dot-sensitized solar cells exceeding efficiency 1% at full-sun intensity," *Journal of Physical Chemistry C*, vol. 112, no. 30, pp. 11600–11608, 2008.
- [4] J. H. Bang and P. V. Kamat, "Quantum dot sensitized solar cells. A tale of two semiconductor nanocrystals: CdSe and CdTe," *ACS Nano*, vol. 3, no. 6, pp. 1467–1476, 2009.
- [5] D. L. Klein, R. Roth, A. K. L. Lim, A. P. Alivisatos, and P. L. McEuen, "A single-electron transistor made from a cadmium selenide nanocrystal," *Nature*, vol. 389, no. 6652, pp. 699–701, 1997.
- [6] I. L. Medintz, H. T. Uyeda, E. R. Goldman, and H. Mattoussi, "Quantum dot bioconjugates for imaging, labelling and sensing," *Nature Materials*, vol. 4, no. 6, pp. 435–446, 2005.
- [7] S. J. Rosenthal, I. Tomlinson, E. M. Adkins et al., "Targeting cell surface receptors with ligand-conjugated nanocrystals," *Journal of the American Chemical Society*, vol. 124, no. 17, pp. 4586–4594, 2002.
- [8] M. A. El-Sayed, "Small is different: shape-, size-, and composition-dependent properties of some colloidal semiconductor nanocrystals," *Accounts of Chemical Research*, vol. 37, no. 5, pp. 326–333, 2004.
- [9] A. Kongkanand, K. Tvrđy, K. Takechi, M. Kuno, and P. V. Kamat, "Quantum dot solar cells. Tuning photoresponse through size and shape control of CdSe-TiO₂ architecture," *Journal of the American Chemical Society*, vol. 130, no. 12, pp. 4007–4015, 2008.
- [10] D. R. Baker and P. V. Kamat, "Photosensitization of TiO₂ nanostructures with CdS quantum dots: particulate versus tubular support architectures," *Advanced Functional Materials*, vol. 19, no. 5, pp. 805–811, 2009.
- [11] A. J. Nozik, "Quantum dot solar cells," *Physica E*, vol. 14, no. 1–2, pp. 115–120, 2002.
- [12] C. B. Murray, D. J. Norris, and M. G. Bawendi, "Synthesis and characterization of nearly monodisperse CdE (E = sulfur, selenium, tellurium) semiconductor nanocrystallites," *Journal of the American Chemical Society*, vol. 115, no. 19, pp. 8706–8715, 1993.
- [13] Z. A. Peng and X. Peng, "Formation of high-quality CdTe, CdSe, and CdS nanocrystals using CdO as precursor," *Journal of the American Chemical Society*, vol. 123, no. 1, pp. 183–184, 2001.
- [14] A. B. Kashyout, M. Soliman, and M. Fathy, "Effect of preparation parameters on the properties of TiO₂ nanoparticles for dye sensitized solar cells," *Renewable Energy*, vol. 35, no. 12, pp. 2914–2920, 2010.
- [15] A. E.-H.B. Kashyout, M. Fathy, and M. B. Soliman, "Studying the properties of RF-sputtered nanocrystalline tin-doped indium oxide," *International Journal of Photoenergy*, vol. 2011, Article ID 139374, 6 pages, 2011.
- [16] I. Mora-Seró, S. Giménez, T. Moehl et al., "Factors determining the photovoltaic performance of a CdSe quantum dot sensitized solar cell: the role of the linker molecule and of the counter electrode," *Nanotechnology*, vol. 19, no. 42, Article ID 424007, 2008.
- [17] I. Robel, V. Subramanian, M. Kuno, and P. V. Kamat, "Quantum dot solar cells. Harvesting light energy with CdSe nanocrystals molecularly linked to mesoscopic TiO₂ films," *Journal of the American Chemical Society*, vol. 128, no. 7, pp. 2385–2393, 2006.
- [18] I. Moreels, B. Fritzing, J. C. Martins, and Z. Hens, "Surface chemistry of colloidal PbSe nanocrystals," *Journal of the American Chemical Society*, vol. 130, no. 45, pp. 15081–15086, 2008.
- [19] J. Taylor, T. Kippeny, and S. J. Rosenthal, "Surface stoichiometry of CdSe nanocrystals determined by Rutherford backscattering spectroscopy," *Journal of Cluster Science*, vol. 12, no. 4, pp. 571–582, 2001.
- [20] J. S. Owen, J. Park, P. E. Trudeau, and A. P. Alivisatos, "Reaction chemistry and ligand exchange at cadmium-selenide nanocrystal surfaces," *Journal of the American Chemical Society*, vol. 130, no. 37, pp. 12279–12281, 2008.
- [21] I. Concina, M. Natile, A. Braga et al., "One pot synthesis of bi-linker stabilised CdSe quantum dots," *Journal of Physics: Conference Series*, vol. 244, no. 1, Article ID 012067, 2010.
- [22] S. H. Choi, H. Song, I. K. Park et al., "Synthesis of size-controlled CdSe quantum dots and characterization of CdSe-conjugated polymer blends for hybrid solar cells," *Journal of Photochemistry and Photobiology A*, vol. 179, no. 1–2, pp. 135–141, 2006.
- [23] W. W. Yu, L. Qu, W. Guo, and X. Peng, "Experimental determination of the extinction coefficient of CdTe, CdSe, and CdS nanocrystals," *Chemistry of Materials*, vol. 15, no. 14, pp. 2854–2860, 2003.

Research Article

Electric Characterization and Modeling of Microfluidic-Based Dye-Sensitized Solar Cell

Adriano Sacco,^{1,2} Andrea Lamberti,^{1,2} Marzia Quaglio,¹ Stefano Bianco,¹ Elena Tresso,^{1,2} Anca-Luiza Alexe-Ionescu,^{1,3} and Candido F. Pirri^{1,2}

¹Center for Space Human Robotics @Polito, Istituto Italiano di Tecnologia, Corso Trento 21, 10129 Torino, Italy

²Dipartimento di Scienza Applicata e Tecnologia, Politecnico di Torino, Corso Duca degli Abruzzi 24, 10129 Torino, Italy

³Faculty of Applied Sciences, University Politehnica of Bucharest, Splaiul Independentei 313, 060042 Bucharest, Romania

Correspondence should be addressed to Stefano Bianco, stefano.bianco@iit.it

Received 3 November 2011; Accepted 4 January 2012

Academic Editor: Latika Menon

Copyright © 2012 Adriano Sacco et al. This is an open access article distributed under the Creative Commons Attribution License, which permits unrestricted use, distribution, and reproduction in any medium, provided the original work is properly cited.

The electric response to an external periodic voltage of small amplitude of dye-sensitized solar cells (DSCs) made up with an alternative architecture has been investigated. DSCs have been fabricated with a reversible sealing structure, based on microfluidic concepts, with a precise control on the geometric parameters of the active chamber. Cells with different electrolyte thicknesses have been characterized, without varying the thickness of the TiO_2 layer, both under illumination and in dark conditions. Measurements of the electric impedance have been performed in the presence of an external bias ranging from 0 V to 0.8 V. The experimental data have been analyzed in terms of a transmission line model, with two transport channels. The results show that the photovoltaic performances of the microfluidic cell are comparable with those obtained in irreversibly sealed structures, actually demonstrating the reliability of the proposed device.

1. Introduction

Since the first paper of O'Regan and Grätzel [1], dye-sensitized solar cells (DSCs) have been widely investigated as one of the most promising candidates for the next-generation solar devices with low production costs, simple fabrication process, and good efficiency in energy conversion. It is easy to obtain DSC samples employing commercially available materials and simple process steps, nevertheless, the performances are strongly dependent on the material quality and the fabrication procedure.

Newly implemented manufacturing solutions such as advanced print screen techniques, electrolyte filling, dye profiling, and sealing machines have been reported for obtaining small laboratory DSC with efficiency up to 10%, good stability, and reproducibility [2–6]. The present DSC research and development focus on finding materials and manufacturing techniques for higher conversion efficiency, lower costs, and longer operating lifetime. In this process, the understanding of the influence of materials and components on the overall efficiency is essential. Experimental

measurements provide a basis for identifying the factors mostly limiting the efficiency of a DSC. Furthermore, when coupled to mathematical models, they can provide a quantitative understanding of the device's physics [7]. Also, numerous papers have been published on modeling and interpreting the results obtained from electrochemical impedance spectroscopy (EIS) measurements [7–16].

Several papers have been published suggesting the best fabrication procedure of the cells [2, 17, 18] and, moreover, in the papers reporting experimental results, the procedure used to obtain small laboratory cells is quite always illustrated in details. Even if sometimes a simple-clips closure has been chosen, the use of hot-melt sealants is generally adopted for closure and protection from the environment. For research purposes, this can be somewhat limiting. Indeed, some of the fabrication steps, as dye adsorption and electrolyte filling, are often performed without any direct/active control, being difficult to ensure reproducibility and reliability while fabricating a large number of cells. Both during experiments and after them, the cell, being irreversibly sealed, does not

grant the possibility of control and inspection, or postprocess modifications.

Recently, our group has proposed a new technological procedure for DSC fabrication [19], which is quite familiar to the field of microfluidics. We designed a cell that is actually made by all the parts of the traditional Grätzel's device, in which a microfluidic chamber has been designed by means of a polydimethylsiloxane (PDMS) membrane. PDMS exhibits a good spontaneous reversible adhesion to glass, metals, and oxides. The membrane acts as a spacer between the two electrodes, defining the inner active volume of the DSC. To ensure a good sealing, the TiO_2 layer is designed having a circular shape entirely confined into the microfluidic chamber. This is obtained performing a casting step into a tape-mould having a hole with a fixed diameter into it. To definitively close the device, a housing system has been designed, with an external clamp closed by screws. In this way, the sealing procedure is reversible, granting inspection and control also after the experiments. Sealing performances of such innovative structure were successfully evaluated by dynamic fluidic tests. Our aim was the engineering of a small laboratory cell which permits to distinguish between the contributions of the different components and technological steps. We employed a microfluidic device which offers good flexibility and still grants low-cost materials and technologies together with the use of very small amounts of reagents. Our modular device enables to substitute one or more components and guarantees the reproducibility of the assembly parameters such as load distribution, screw tightening, and thicknesses control. We have devoted particular care in the definition of the active surface, in the control of thickness uniformity and of the dye impregnation.

In this paper, commercially available DSC materials have been used to fabricate a set of microfluidic solar cells, with two different electrolyte thicknesses. Electric characterization has been performed through standard $I - V$ measurements and through EIS measurements under light and dark conditions, at different bias voltages. The experimental data are analyzed in terms of a transmission line model, with two transport channels, to validate already proposed models [20]. This validation is fundamental since it shows that our microfluidic approach does not change the nature of the device but simply adds flexibility and reliability. We demonstrate the effectiveness of the microfluidic cells as a standard modular prototype which can be used for testing different DSC components.

The paper is organized as follows. In Section 2, we describe the microfluidic cell preparation procedure. In Section 3, the transmission line model which is used to fit the experimental data is briefly recalled. In Section 4, experimental results are presented and the best fit parameters of our data are discussed. Section 5 is devoted to the conclusions.

2. Experimental

Fluorine-doped-tin-oxide- (FTO) covered glasses ($7\ \Omega/\text{sq}$, Solaronix) were rinsed with acetone and ethanol in an

ultrasonic bath for 10 min. Then, a TiO_2 layer (Ti-Nanoxide D37 paste, Solaronix) with a circular shape (with a fixed diameter of $(10.00 \pm 0.05)\text{ mm}$) was deposited on FTO by tape-casting technique and dried at 50°C for 30 min on a hot plate. A sintering process at 450°C for 30 min allowed the formation of nanoporous TiO_2 film with a mean thickness of $(7.5 \pm 0.5)\ \mu\text{m}$, as measured by profilometry (P.10 KLA-Tencor).

Photoelectrodes were soaked into a 0.2 mM N719 dye solution (Ruthenizer535bis-TBA, Solaronix) in ethanol for 24 h at room temperature and then rinsed in pure ethanol to remove the unadsorbed molecules. Two small pin holes for inlet/outlet connections were drilled in the FTO glass counter electrodes through powder-blasting technique. Substrates were then cleaned with the same rinsing method described above and a 5 nm Pt layer was deposited onto FTO by thermal evaporation. The inlet/outlet ports for electrolyte (Iodolyte AN 50, Solaronix) filling were connected via low-density polyethylene tubes and closed for operation with PDMS caps.

The operating chamber was defined through a PDMS membrane, prepared by casting technique. PDMS prepolymer and curing agent (Sylgard 184, Dow Corning) were mixed in a 10 : 1 weight ratio and degassed in low vacuum for 1 h. The mixture was then poured into the mould and cured in a convection oven for 1 h at 70°C . The membrane was then peeled off from the mould and reversibly sandwiched between the electrodes. Accurate control in the volume of the mould and on PDMS weight during casting process allowed a precise control in membrane thickness and uniformity. The PDMS membrane laterally defines the active chamber of the cell. For our microfluidic cells, two different membrane thicknesses have been chosen, $(200 \pm 15)\ \mu\text{m}$ and $(100 \pm 8)\ \mu\text{m}$, for obtaining one "thick" and one "thin" chamber, respectively. A double-drop membrane layout was chosen to promote air bubble evacuation during electrolyte filling. The device is closed by an external housing system (made of two poly(methyl methacrylate) frames) that clamps the two electrodes and allows fluids handling. A $50\ \mu\text{m}$ retaining ring is designed on the membrane to follow the profile of the chamber ensuring sealing by completely deforming when closing the device with screws. The complete deformation of the retaining ring grants the final distance between the electrodes to coincide with the thickness of the membranes. The strength applied to the screws is controlled by a torque spanner. In this way, the sealing procedure is reversible, allowing inspection and control after the experiments.

All cells had an active area of 0.78 cm^2 and measurements were performed with a 0.22 cm^2 shadow mask. Copper foils ($50\ \mu\text{m}$ thick, area 1.5 cm^2) were used for electric connections at the electrodes, dielectrically isolated by the PDMS membrane.

Impedance analysis was done using a potentiostat (760D, CH Instruments) in a two-electrode configuration: reference and counter electrodes were linked together to DSC cathode, while working electrode was connected to the cell photoanode. The amplitude of the AC signal was 10 mV, and the frequency was varied in the range 10^{-1} – 10^4 Hz .

The applied bias potential has been varied in the range 0–0.8 V. Measurements were taken both under 1 sun AM1.5G illumination, using a class A solar simulator (91195A, Newport), or in dark conditions.

3. Model

In electrochemical cells, the transport and charge-transfer processes are described by nonlinear equations connecting the driving forces to the flux of the particles. The impedance spectroscopy technique is based on the analysis of the electric response of a cell to a periodic external electric excitation of variable frequency. When the amplitude of the applied voltage is comparable with the thermal voltage, $V_{th} = k_B T/q$, the fundamental equations describing the charge redistribution in the cell due to the external voltage are linear [21]. In this approximation, it is possible to describe all the processes by linear equations in which the coefficient between the electrochemical potential and the current is the electric impedance. In this framework, the electrochemical cell can be described by an equivalent electric circuit.

The performances of the DSC are connected with the morphology and structure of the TiO_2 layer on which the dye molecules are attached, with the ability of the electrolyte of regenerating the photoabsorbing molecules and also with the contact between the solid film or the electrolyte and the conductive electrodes. All these processes have characteristic times ranging from hundreds of seconds to microseconds, which, transposed into the frequency domain, correspond to the mHz to MHz part of the electromagnetic spectrum. The impedance spectroscopy technique allows separating different processes occurring in such very complex systems. From the impedance spectra, it is possible to analyze the diffusion-recombination electronic processes in the TiO_2 film and at the interface solid film-electrolyte, the diffusion mechanism of the redox species in the electrolyte, and also the charge transfer at the electrodes. The diffusion time of the redox species strongly depends on the thickness of the electrolyte and this, in turn, is connected to the overall thickness of the cell.

A porous film in contact with an electrolyte is described by a transmission line model with two transport channels and crosswise elements [20]. The carrier transport is simultaneously of electronic origin in the solid phase and ionic in the liquid. Both media in contact are supposed to be homogenous and continuously connected phases. Due to the special geometrical structure of the complex system film-electrolyte, there will be a distribution of the electric current generated by the charges moving along each media and also on the direction normal to the internal surface. The total electric current can be expressed as a sum of AC currents, i_1 and i_2 , flowing in the liquid and solid phase, respectively. The impedance of the solid film in contact with the electrolyte is obtained by solving the equations for the electric currents and their local variations in both phases [22, 23]. The charge transport in the solid or liquid phases is simply showed by resistances. The electrolyte-solid film interface and the associated electrochemical processes are

described as an electric circuit formed by a parallel of a capacitor and a resistance:

$$Z_R = \frac{R_{tr} \cdot R_e}{R_{tr} + R_e} \left(1 + \frac{2\lambda/d}{\sinh(d/\lambda)} \right) + \frac{\lambda}{d} \frac{R_{tr}^2 + R_e^2}{R_{tr} + R_e} \coth\left(\frac{d}{\lambda}\right), \quad (1)$$

where

$$\frac{\lambda}{d} = \sqrt{\frac{Z_{ct}}{R_{tr} + R_e}}. \quad (2)$$

In (1), R_{tr} and R_e are the transport resistance in the solid film and the diffusion resistance in the electrolyte, respectively, and d is the thickness of the porous film [20]. Equation (1) has been obtained by imposing that the ionic current is zero at the end of the pore in the film and also that the electronic current in the solid film is zero at the outer edge of the film. These suppositions are assumed for the situation in which the edges of the solid film are planar and perfectly reflecting.

In (2), Z_{ct} is the equivalent impedance formed by a parallel R_{ct} and C_t :

$$Z_{ct} = \frac{1}{i\omega C_t + R_{ct}^{-1}}, \quad (3)$$

where C_t is the total capacitance in the solid film and within the interface, R_{ct} is the charge-transfer resistance at the solid-electrolyte interface. This description is related to the presence of both faradaic and polarization currents in the region separating the two phases. In terms of resistance and capacitance connected to the solid-electrolyte interface, it is possible to define a characteristic time $\tau_n = (\omega_n)^{-1} = R_{ct} C_t$ associated to the electron lifetime in the solid film.

The collection efficiency of the charges at the front electrode requires that the electron diffusion length, L_n , is greater than the thickness of the porous film. The electron diffusion length is related to the ratio between the charge transport time, $\tau_{tr} = R_{tr} C_t$ and the charge lifetime, $\tau_n = R_{ct} C_t$, $L_n = d(\tau_n/\tau_{tr})^{1/2}$ [23]. For good charge collection efficiency, the charge-transfer resistance has to be larger than the transport resistance.

The impedance describing the diffusion of the redox species in the electrolyte has the form:

$$Z_e = R_e \frac{\tanh(\sqrt{i\omega/\omega_d})}{\sqrt{i\omega/\omega_d}}, \quad (4)$$

where ω_d is the characteristic frequency of the diffusion [24].

The contact between the electrolyte and the counter electrode is modeled by a parallel $R_p C_p$, with the equivalent impedance:

$$Z_p = \frac{1}{i\omega C_p + R_p^{-1}}, \quad (5)$$

where C_p is the interfacial Helmholtz (double-layer) capacitance and R_p is the charge-transfer resistance at the counter electrode [25].

It follows that the total impedance for a DSC is

$$Z = R_s + Z_R + Z_e + Z_p, \quad (6)$$

where R_s is the resistance of the leads and of the ohmic contacts to the cell.

The different contributions to the total impedance Z of the cell depend on the frequency in different manners. From the fit of the full spectra of its real and imaginary parts, we can derive information on the different mechanisms responsible for the conduction across the DSC.

The best fit of the experimental data is obtained by minimizing the quantity:

$$s = \frac{\sum_{i=n_i}^{n_f} |R(\omega_i) - R_{\text{exp}}(\omega_i)|}{2(n_f - n_i + 1)\bar{R}_{\text{exp}}} + \frac{\sum_{i=n_i}^{n_f} |X(\omega_i) - X_{\text{exp}}(\omega_i)|}{2(n_f - n_i + 1)\bar{X}_{\text{exp}}}, \quad (7)$$

where $R(\omega_i) = \text{Re} Z(\omega_i)$ is the real part of the total impedance, $R_{\text{exp}}(\omega_i)$ is the measured value, \bar{R}_{exp} is the average of the experimental values $R_{\text{exp}}(\omega_i)$, and $(n_f - n_i + 1)$ is the total number of experimental points. Similar definitions stand for the imaginary part of the impedance $X = \text{Im}(Z)$. The factor 2 in the denominator was used to make $s = 1$ if $Z(\omega) \equiv 0$. We have chosen to express the minimizing function s in terms of absolute values of $R(\omega_i) - R_{\text{exp}}(\omega_i)$ and not, as usual, in terms of squares of these deviations, for the reason that the minimizing procedure was entirely numerical, no derivatives were necessary and, numerically, the evaluation of the absolute value is less time consuming than squaring.

4. Results and Discussion

4.1. Efficiency and Reproducibility of the Microfluidic Solar Cell. The microfluidic solar cells have been designed to permit control, reproducibility, and reliability in a simple system. Moreover, the reversibility of the sealing is designed to allow the inspection of the prototypes after usage. A significant attention has been devoted to the characterization of the reproducibility of the photovoltaic conversion efficiency. In Figure 1(a) we report a scheme of a microfluidic DSC in which all the elements constituting the cell are exploded, in Figure 1(b) a picture of the final device, and in Figure 1(c) the evaluation of the sun energy conversion efficiency for a statistically significant number of identical cells. The evaluated conversion efficiency is $(6.76 \pm 0.11)\%$. The variation of the predicted efficiency value around the average value is comparable with the one obtained with irreversibly-sealed structure [2]. In Table 1, the obtained electric parameters are reported for typical “thin” and “thick” cells.

4.2. EIS Measurements. Several papers have reported on the impedance spectroscopy of DSC. However, only a few have investigated the electric response of the cells with different thicknesses of electrolyte, since standard cells do not allow modifying this parameter in a controllable manner. In what follows, we compare the Nyquist plots for DSC varying their thicknesses. Special attention is devoted to the electric response under light and dark conditions. In all reported Nyquist diagrams, we subtract the resistance of the electrode,

responsible for the value of the impedance of the full system in the high-frequency limit. In this manner, the diagrams are relevant only to the electric properties of the cell.

In Figure 2, we compare the Nyquist diagrams corresponding to cells with different thicknesses ($L_1 = 200 \mu\text{m}$, $L_2 = 100 \mu\text{m}$) subjected to bias voltages ranging from 0 V to 0.8 V, under light (Figures 2(a) and 2(b)) and dark (Figures 2(c) and 2(d)) conditions. As it follows from Figure 2, in the high-frequency region the parametric plot of $-X$ versus R is a straight line with a slope quite equal to 1, and this result is independent of the thickness of the cell. The experimental results are in agreement with the model proposed by Bisquert [20] according to which in this frequency region the impedance of the DSC is mainly due to the electrolyte. In fact, for large frequency, $Z \rightarrow Z_e$.

By taking into account (4) and that in this region $\omega \gg \omega_d$, we get

$$Z \rightarrow Z_e \approx R_e \sqrt{\frac{\omega_d}{2\omega}} (1 - i). \quad (8)$$

Consequently, the real and imaginary parts of Z tend to

$$\begin{aligned} R &\rightarrow R_e \sqrt{\frac{\omega_d}{2\omega}}, \\ -X &\rightarrow R_e \sqrt{\frac{\omega_d}{2\omega}}, \end{aligned} \quad (9)$$

respectively, and $-X = R$, indicating that the parametric plot of $-X$ versus R is a straight line with the slope equal to 1. A simple analysis shows that

$$R_e = \frac{\alpha}{qD} \frac{L}{S}, \quad (10)$$

where α depends on the exchange of the charges at the electrode due to the adsorption, q is the electric charge of the ion, S is the effective surface of the porous electrode, and D is the ionic diffusion coefficient.

Furthermore, the diffusion circular frequency is $\omega_d = D/L^2$. Consequently, in the high frequency region,

$$R \rightarrow R_e \sqrt{\frac{\omega_d}{2\omega}} = \frac{\alpha}{q\sqrt{D}} \frac{1}{S} \sqrt{\frac{1}{2\omega}}. \quad (11)$$

This result indicates that both, in the considered frequency range, R and $-X$ are independent of the thickness of the electrolyte. For the dark state, the behavior in the high-frequency range coincides with that in the light state.

In Figures 2(b) and 2(d), for the bias voltage of 0.6 V and the thickness of L_2 , the different contributions to the impedance are not separable on the parametric plot. For larger bias voltages and thicknesses, the processes related to the counter electrode and TiO_2 are well separated. It can be seen that the amplitude and the position of the peak corresponding to the charge transfer at the counter electrode are the same, for the same thickness and bias voltage, under light and dark conditions. On the contrary, the peak connected with the recombination in the TiO_2 layer has smaller amplitudes for the light conditions and different positions.

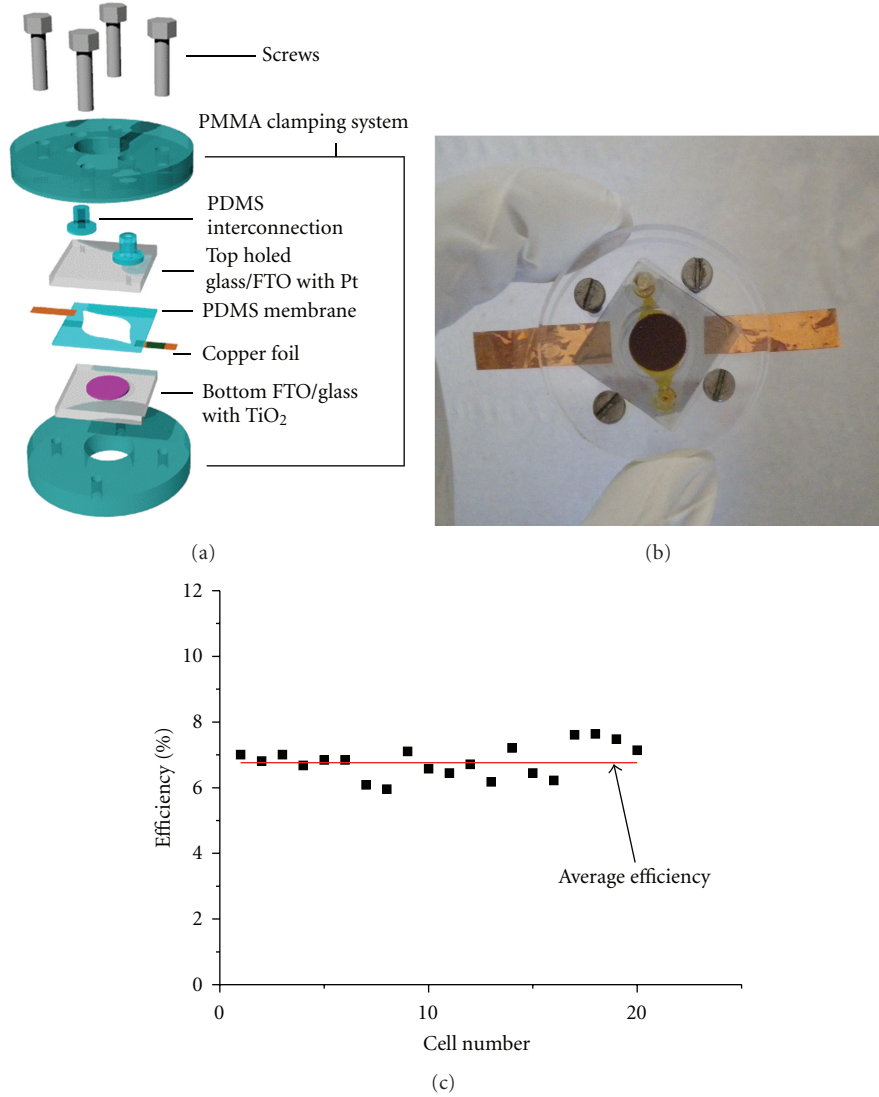


FIGURE 1: (a) Scheme of the microfluidic DSC with the detail of all the elements constituting the cell. (b) A picture of the final device. (c) Evaluation of the energy conversion efficiency for 20 nominally identical cells. Cell thickness was fixed at $200\ \mu\text{m}$.

TABLE 1: Electric parameters of two typical microfluidic cells with different thicknesses: J_{SC} , short circuit density of current, V_{OC} , open circuit voltage, FF, fill factor.

	$L_1 = 100\ \mu\text{m}$	$L_2 = 200\ \mu\text{m}$
$J_{\text{SC}}\ [\text{mA}/\text{cm}^2]$	19.5	20.5
$V_{\text{OC}}\ [\text{V}]$	0.64	0.64
FF	0.58	0.55
Efficiency [%]	7.22	7.29

In Figure 3(a), for the cell with $L_1 = 200\ \mu\text{m}$, we compare the Nyquist diagrams for three different bias voltages (0.4 V, 0.6 V, and 0.8 V) under illumination. For biases larger than 0.4 V, the Nyquist diagram indicates the presence of two well-defined dissipative processes. The semicircles in the high-frequency limit, related to the counter electrode, have a

radius which is a decreasing function of the bias voltage. The same conclusion holds true for the semicircle connected to TiO₂ electrode appearing for moderate frequency. On the contrary, with our experimental accuracy, no conclusion can be derived for the semicircle related to the diffusion process in the electrolyte, appearing in the DC limit: the 0.1 Hz lower limit in EIS is not low enough for the cells, considering the redox ion used. Figure 3(b) refers to the same cell, under dark conditions. For large frequencies, the parametric plots of $-X$ versus R are independent of the bias, and all the curves coincide, as evidenced in the zoom reported in Figure 3(b-1).

In Figure 4, the Nyquist diagrams for the two cells under the bias voltage of 0.4 V are compared: in Figure 4(a) under light and in Figure 4(b) under dark conditions. An interesting feature of the diagrams is that under illumination the resistance of the cell is larger for $100\ \mu\text{m}$ than for $200\ \mu\text{m}$, whereas for dark measurements the trend is reversed. The

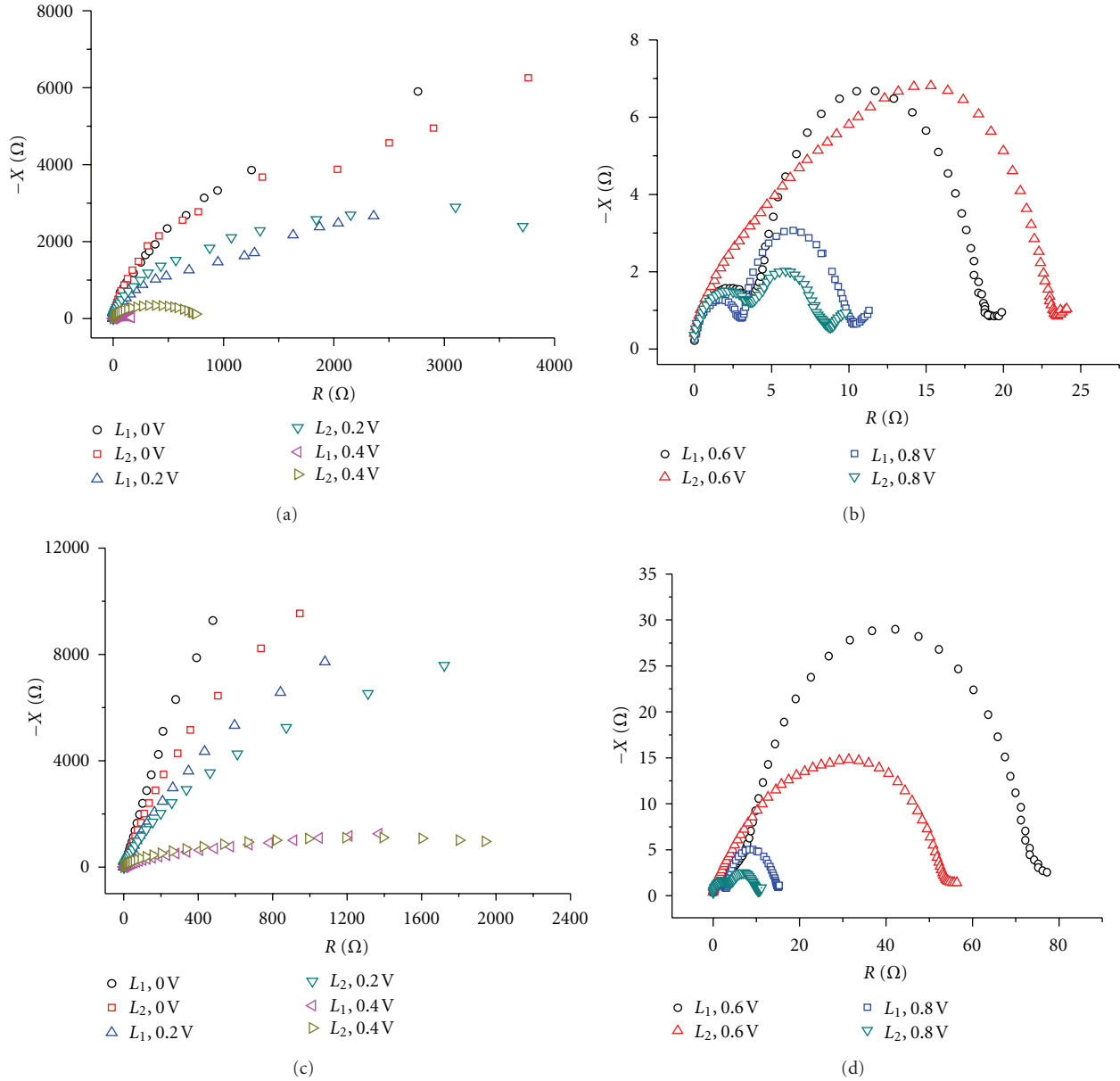


FIGURE 2: Nyquist diagrams for DSC with thicknesses $L_1 = 200 \mu\text{m}$ and $L_2 = 100 \mu\text{m}$, under bias voltages ranging from 0 V to 0.8 V, under light (a, b) and dark (c, d) conditions.

same feature may be seen in Figure 5 for 0.6 V bias, but not for 0.8 V bias. These experimental results can be interpreted in terms of the following consideration. The effect of the electrolyte in the system is to furnish the ionic charges to regenerate the dye molecules adsorbed on the porous electrode. In the ideal case, each dye molecule would have an ion nearby in order to be immediately regenerated. For imaging a dynamic process in which the ions are positioned in front of the adsorbed layer of dyes in the pores, in the “thin” cell, for low biases (≤ 0.6 V), even if the liquid electrolyte is filling all the pores, it might happen that the ions within the pore are not enough to regenerate all the nearby molecules of the dye. In the thicker cell, the overall number of ions is larger, and so, although the equilibrium

concentration is the same for the same bias, the number of ionic charges per unit surface within the pores, can be larger. For higher biases within all the pores, the dye molecules can be saturated by the ions even in thinner cells and the apparent resistance is given mainly by the resistance of the ionic film, the larger the film, the larger the resistance. Of course, for dark conditions, the regeneration process does not appear and the cells, behave normally, that is, thicker cells, larger resistances.

Until now, we just discussed the parametric plots showing $-X$ versus R , when the parameter is the frequency of the applied voltage. Some information can also be derived from the spectra of R and $-X$. In this case, the presence of the different dissipative phenomena is indicated by plateau and

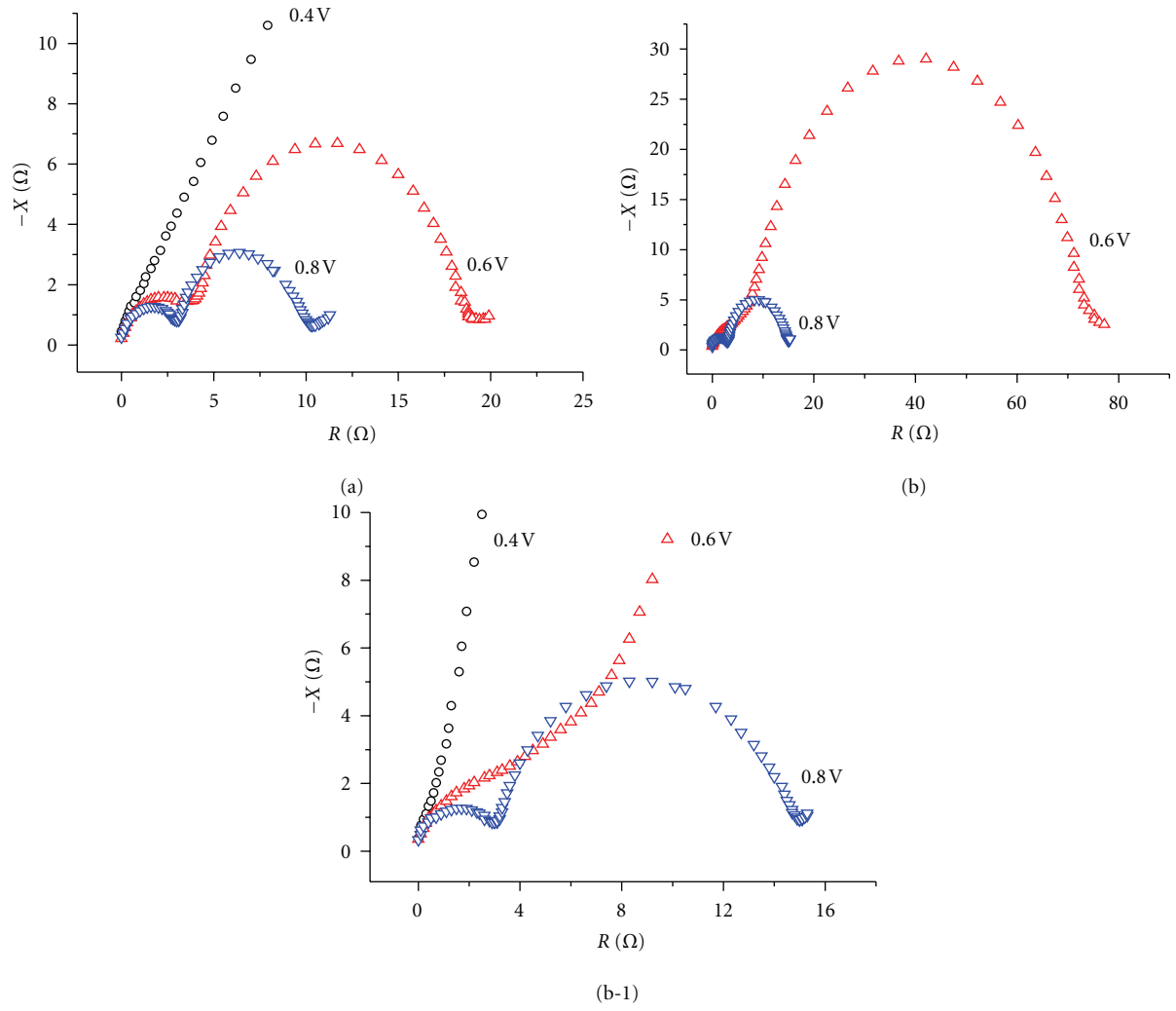


FIGURE 3: Nyquist diagrams for three different bias voltages (0.4 V, 0.6 V and 0.8 V) corresponding to the cell of $L_1 = 200 \mu\text{m}$, under light (a) and dark conditions (b). Zoom in the high-frequency region in and dark state (b-1).

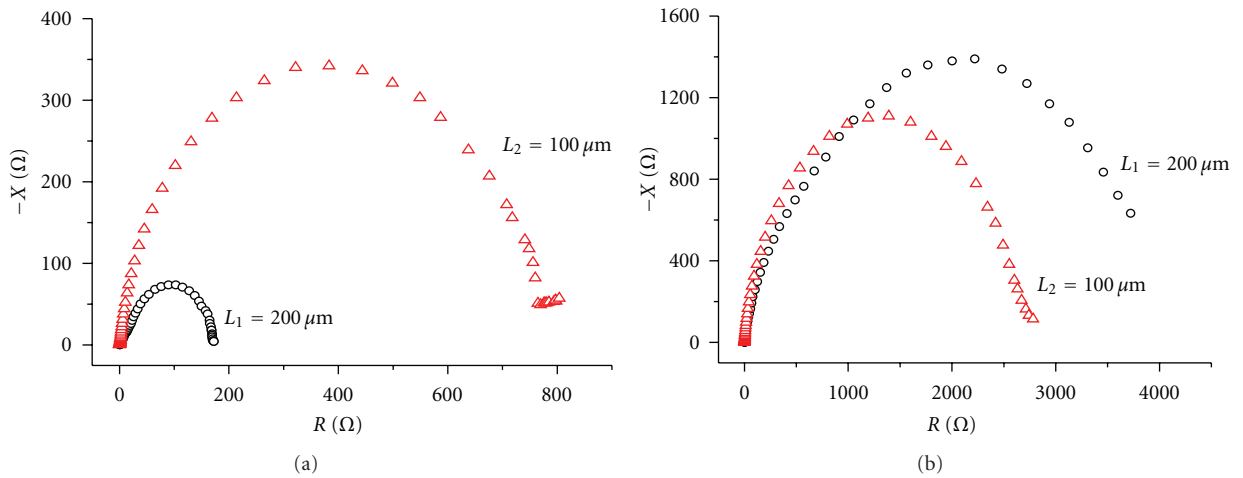


FIGURE 4: Nyquist diagrams for the cells with the thicknesses $L_1 = 200 \mu\text{m}$ and $L_2 = 100 \mu\text{m}$, under the bias voltage of 0.4 V, in light (a) and dark (b) conditions. Note the different relative positions of the corresponding curves in the light and dark conditions.

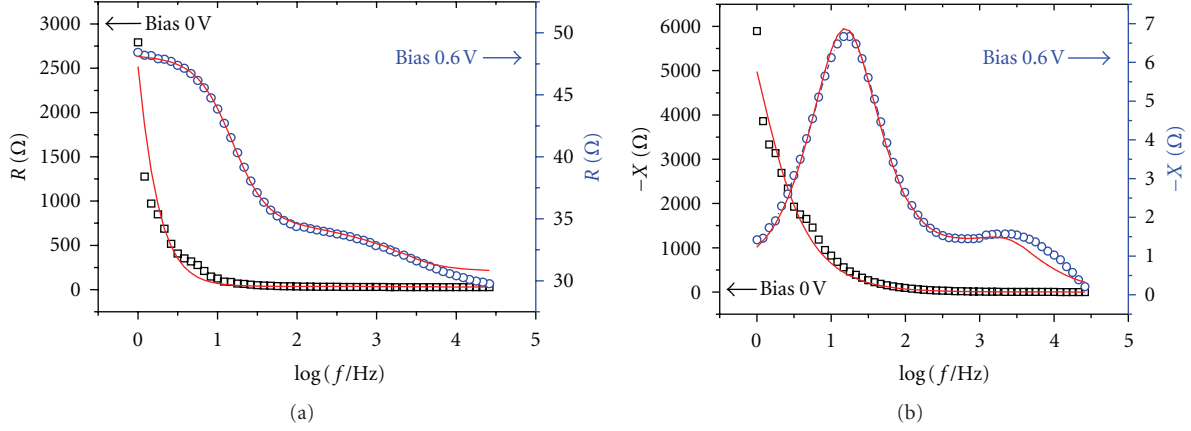


FIGURE 5: Real (a) and imaginary (b) parts of the impedance for the DSC with $L_1 = 200 \mu\text{m}$ under illumination. Black squares and blue circles are the experimental data for bias of 0 V and 0.6 V, respectively. Black and blue continuous curves are the corresponding best fits, obtained by means of the model described in the text.

maxima of R and $-X$, respectively. The spectra of the real (R) and imaginary ($-X$) parts of the total impedance Z of the cell given by (6) under light conditions are shown in Figures 5(a) and 5(b), respectively. In these figures, the squares refer to the case in the absence of bias and the circles to a bias voltage of 0.6 V.

As expected, the presence of the bias strongly reduces the resistance and the modulus of the reactance because the number of carriers increases. From Figure 5, we deduce that in the absence of any bias voltage, R and $-X$ are monotonic functions of frequency (in the range between 1 Hz and 40 kHz). On the contrary, in the presence of bias voltage, the spectrum of R presents two plateaux, one in the DC limit and the second one around 100 Hz, whereas the spectrum of $-X$ presents a dissipation peak around 30 Hz related to the plateaux in the DC limit. The second peak is not visible in this limited range. Similar diagrams, not reported, can be derived in the experimental situation described in the previous figures. The best fit parameters of these curves, used in the characterization of TiO_2 -electrolyte interface, are discussed in the following section as far as their bias voltage dependence is concerned.

4.3. Characterization of the TiO_2 -Electrolyte Interface. To investigate the dependence of the photoanode-electrolyte interface impedance on the bias voltage, we performed measurements of the same kind reported in Figure 5 for bias voltages ranging from 0 V to 0.8 V. The parameters of the best fit R_{ct} and C_t , characterizing this interface, versus the bias voltage V , are shown in Figures 6(a) and 6(b), for the cells under light conditions. The triangles and stars refer to cells of thicknesses $100 \mu\text{m}$ and $200 \mu\text{m}$, respectively. We note that these quantities weakly depend on the thickness of the DSC, as expected, as they have to describe interface properties. The bias voltage dependence of R_{ct} and C_t is well described by the model of Bisquert [20] according to which

$$\begin{aligned} R_{\text{ct}} &= R_0 \exp(-\beta V/V_{\text{th}}), \\ C_t &= C_0 \exp(\alpha V/V_{\text{th}}), \end{aligned} \quad (12)$$

where R_0 and C_0 are the resistance and capacitance of the interface at 0 V bias, and β and α are two constants [22, 25]. From the best fit of Figure 6(a) and 6(b), we find $\beta(100 \mu\text{m}) = 0.13$, $\beta(200 \mu\text{m}) = 0.17$, and $\alpha(100 \mu\text{m}) = 0.15$, $\alpha(200 \mu\text{m}) = 0.11$, values comparable with those reported in [20].

The difference between α and β may be explained by the fact that R_{ct} depends on the free contact surface between the titania and the electrolyte (i.e., the total surface of the pore minus the surface occupied by the adsorbed dye molecules) whereas C_t depends on the total surface of the pore (considering that the adsorbed dye molecular film minimally alters the dielectric constant in the interface).

C_t is mainly related with the chemical capacitance that is connected to the carrier concentration in the conductive band or with the DOS at the E_c position, but it depends also on surface interactions on TiO_2 nanoparticles. In fact, a contribution to the capacitance has a dielectric origin and is related with the depletion at semiconductor/TCO or semiconductor/electrolyte interfaces, depending on voltage as $1/\sqrt{V}$ [20, 22]. Moreover, one has to consider the double-layer capacitance in the electrolyte part of the semiconductor/electrolyte interface (in the case of concentrated electrolytes, it is known as Helmholtz capacitance). Thus, the dependence of C_t on the bias voltage may not be a pure increasing exponential. The above formulae may be compared to the bias dependence of the carrier concentration in a semiconductor, namely, $n = n_0 \exp(qV/k_B T)$, introducing an effective temperature $T_{\text{eff}} = T/\alpha$ (or T/β). As $T_{\text{eff}} > T$, we may say that to the entropic disorder characterized by T , in a single crystal semiconductor there is a supplementary disorder introduced by the porosity of titania and the adsorption of dye molecules.

At least, a part of α may correspond to a larger effective temperature in the case of porous media.

By means of the measured R_{ct} and C_t , we evaluate the relaxation time related to the charge transfer by means of $\tau_n = R_{\text{ct}} C_t$, reported in Figure 6(c). From this figure, it follows that τ_n is practically independent on the thickness of

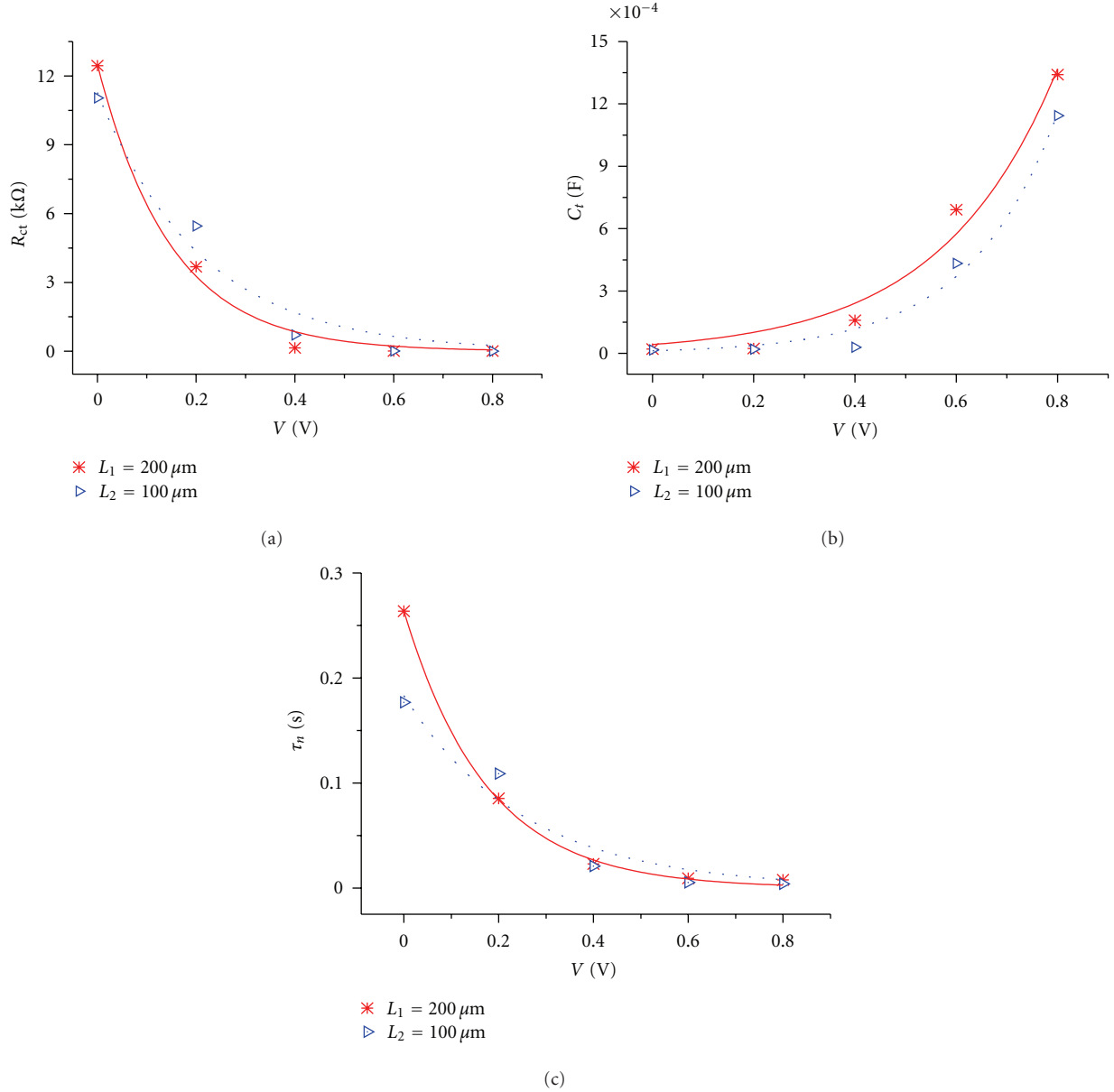


FIGURE 6: Charge transfer resistance (a), total capacitance (b), and charge lifetime (c) versus applied bias voltage for two cells with $L_1 = 200 \mu\text{m}$ (red stars) and $L_2 = 100 \mu\text{m}$ (blue triangles), under light conditions. The continuous curves are the best fit, obtained by means of the model described in the text. $\tau_n = R_{ct}C_t$ is the charge-transfer relaxation time.

the DSC and depends on the bias in an exponential manner, as it follows from the expression (12).

In Figure 7, we report the same parameters shown in Figure 6, for the DSC under dark conditions. From the best fit of Figures 7(a) and 7(b), we find $\beta(100 \mu\text{m}) = 0.17$, $\beta(200 \mu\text{m}) = 0.23$ and $\alpha(100 \mu\text{m}) = 0.25$, $\alpha(200 \mu\text{m}) = 0.12$.

From the experimental data, it is possible to evaluate the diffusion coefficient (D), the carrier concentration in the TiO_2 layer (n) and the diffusion length of the carrier in the TiO_2 layer (L_n) by means of the equations $D = d^2/R_{tr}C_t$, $n = (k_B T/q^2) \cdot (C_t/S \cdot d)$ and $L_n = d(R_{ct}/R_{tr})^{1/2}$. For our DSC of thickness $L_1 = 200 \mu\text{m}$ submitted to the bias voltage

of 0.6 V, we find $D \sim 7.6 \cdot 10^{-9} \text{ m}^2/\text{s}$, $n \sim 1.32 \cdot 10^{23} \text{ m}^{-3}$, and $L_n \sim 8.39 \cdot 10^{-6} \text{ m}$.

5. Conclusions

A new microfluidic technological procedure for DSC fabrication has been proposed. Our aim is the engineering of a small laboratory cell which permits to distinguish between the contributions of the different components and technological steps. The microfluidic structure is reversibly sealed and can be interfaced with a housing system consisting of mechanical clamping, inlet/outlet ports, and interconnections to external

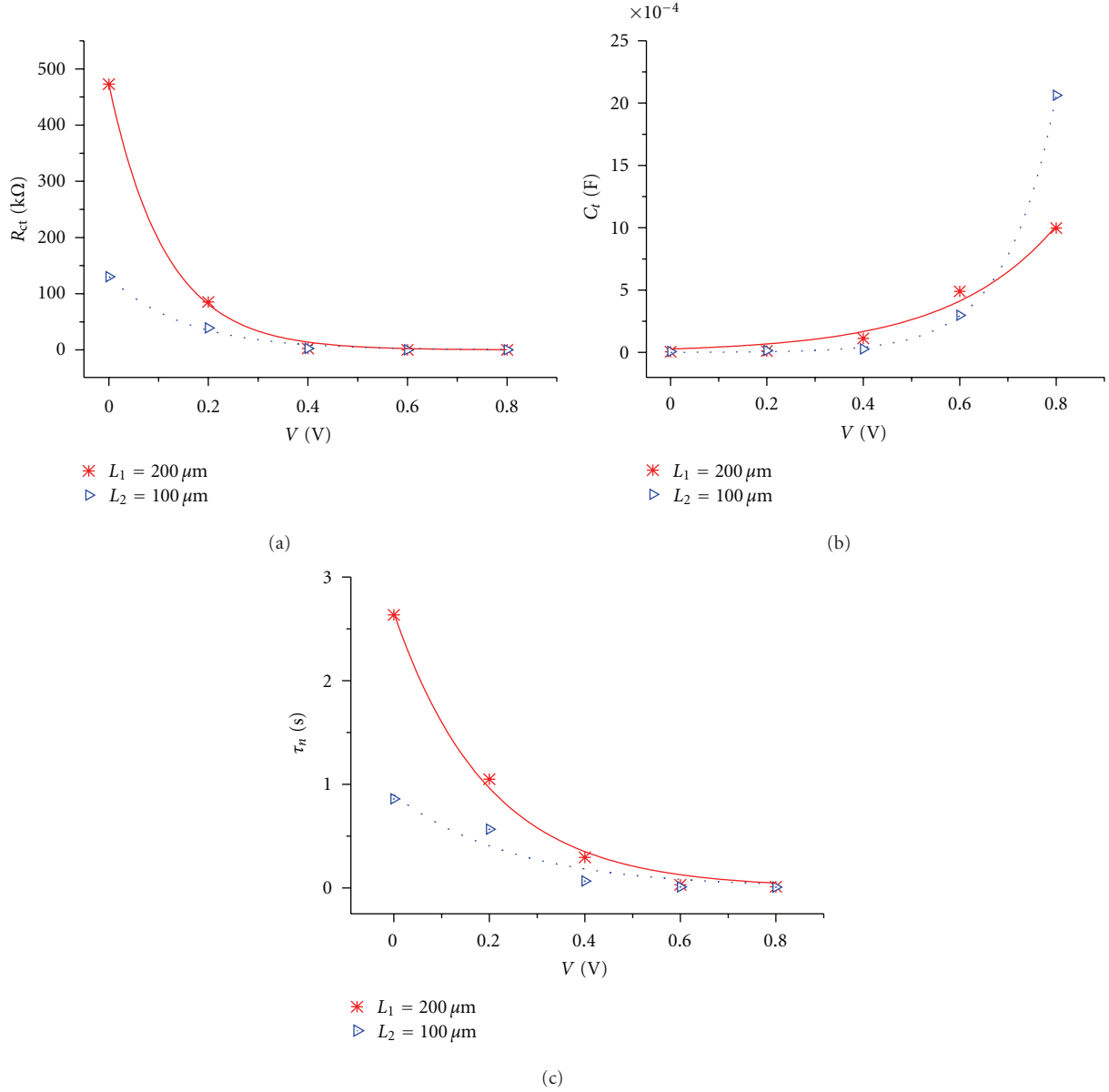


FIGURE 7: Charge transfer resistance (a), total capacitance (b), and charge lifetime (c) versus applied bias voltage for two cells with thicknesses $L_1 = 200 \mu\text{m}$ (red stars) and $L_2 = 100 \mu\text{m}$ (blue triangles), under dark conditions. The continuous curves are the best fit, obtained by means of the model described in the text. $\tau_n = R_{ct}C_t$ is the charge-transfer relaxation time.

fluids handling devices. This technological approach guarantees a high degree of reproducibility, as demonstrated by a statistical analysis. Moreover, the modularity of the device enables the possibility of postprocess control and inspection.

We have investigated the electrical response of a microfluidic DSC to an external voltage of variable frequency. EIS measurements have been performed under light and dark conditions, at different bias voltages ranging from 0 V to 0.8 V and for two different thicknesses of the cells. The experimental data are analyzed by means of a transmission line model, with two transport channels, to validate already proposed models. From the spectra of the real and imaginary parts of the electric impedance of the cell, we have derived the

charge-transfer resistance and total capacitance relevant to the interface porous electrode-electrolyte. The experimental data are well described by the transmission line model and the parameters characterizing the diffusion coefficient, carrier concentration, and the diffusion length of the carrier in the TiO_2 layer are in agreement with the values reported in the literature.

This validation is fundamental since it shows that our microfluidic approach does not change the nature of the device, but simply adds flexibility and reliability. We demonstrate the effectiveness of the microfluidic cells as a standard modular prototype which can be used for testing different DSC components.

Acknowledgment

The authors would like to thank D. Flore for the collaboration in cells fabrication.

References

- [1] B. O'Regan and M. Grätzel, "A low-cost, high-efficiency solar cell based on dye-sensitized colloidal TiO_2 films," *Nature*, vol. 353, no. 6346, pp. 737–740, 1991.
- [2] S. Ito, T. N. Murakami, P. Comte et al., "Fabrication of thin film dye sensitized solar cells with solar to electric power conversion efficiency over 10%," *Thin Solid Films*, vol. 516, no. 14, pp. 4613–4619, 2008.
- [3] J. M. Kroon, N. J. Bakker, H. J. P. Smit et al., "Nanocrystalline dye-sensitized solar cells having maximum performance," *Progress in Photovoltaics*, vol. 15, no. 1, pp. 1–18, 2007.
- [4] D. Shi, N. Postrakulchote, R. Li et al., "New efficiency records for stable dye-sensitized solar cells with low-volatility and ionic liquid electrolytes," *Journal of Physical Chemistry C*, vol. 112, no. 44, pp. 17046–17050, 2008.
- [5] M. Späth, P. M. Sommeling, J. A. M. Van Roosmalen et al., "Reproducible manufacturing of dye-sensitized solar cells on a semi-automated baseline," *Progress in Photovoltaics*, vol. 11, no. 3, pp. 207–220, 2003.
- [6] M. K. Nazeeruddin, E. Baranoff, and M. Grätzel, "Dye-sensitized solar cells: a brief overview," *Solar Energy*, vol. 85, no. 6, pp. 1172–1178, 2011.
- [7] J. Halme, P. Vahermaa, K. Miettunen, and P. Lund, "Device physics of dye solar cells," *Advanced Materials*, vol. 22, no. 35, pp. E210–E234, 2010.
- [8] G. Barbero, A. L. Alexe-Ionescu, and I. Lelidis, "Significance of small voltage in impedance spectroscopy measurements on electrolytic cells," *Journal of Applied Physics*, vol. 98, no. 11, Article ID 113703, pp. 1–5, 2005.
- [9] G. Barbero, M. Becchi, and F. C. M. Freire, "Contribution of the electrode-electrolyte interface to the impedance of an electrolytic cell," *Journal of Applied Physics*, vol. 104, no. 11, Article ID 114111, 2008.
- [10] G. Barbero and I. Lelidis, "Evidence of the ambipolar diffusion in the impedance spectroscopy of an electrolytic cell," *Physical Review E - Statistical, Nonlinear, and Soft Matter Physics*, vol. 76, no. 5, 2007.
- [11] E. K. Lenzi, L. R. Evangelista, and G. Barbero, "Fractional diffusion equation and impedance spectroscopy of electrolytic cells," *Journal of Physical Chemistry B*, vol. 113, no. 33, pp. 11371–11374, 2009.
- [12] F. Fabregat-Santiago, J. Bisquert, G. Garcia-Belmonte, G. Boschloo, and A. Hagfeldt, "Influence of electrolyte in transport and recombination in dye-sensitized solar cells studied by impedance spectroscopy," *Solar Energy Materials and Solar Cells*, vol. 87, no. 1-4, pp. 117–131, 2005.
- [13] Q. Wang, J. E. Moser, and M. Grätzel, "Electrochemical impedance spectroscopic analysis of dye-sensitized solar cells," *Journal of Physical Chemistry B*, vol. 109, no. 31, pp. 14945–14953, 2005.
- [14] J. Bisquert, D. Cahen, G. Hodes, S. Rühle, and A. Zaban, "Physical chemical principles of photovoltaic conversion with nanoparticulate, mesoporous dye-sensitized solar cells," *Journal of Physical Chemistry B*, vol. 108, no. 24, pp. 8106–8118, 2004.
- [15] M. Liberatore, F. Decker, L. Burtone et al., "Using EIS for diagnosis of dye-sensitized solar cells performance," *Journal of Applied Electrochemistry*, vol. 39, no. 11, pp. 2291–2295, 2009.
- [16] F. Fabregat-Santiago, J. Bisquert, E. Palomares, S. A. Haque, and J. R. Durrant, "Impedance spectroscopy study of dye-sensitized solar cells with undoped spiro-OMeTAD as hole conductor," *Journal of Applied Physics*, vol. 100, no. 3, Article ID 034510, 2006.
- [17] S. Ito, M. K. Nazeeruddin, P. Liska et al., "Photovoltaic characterization of dye-sensitized solar cells: effect of device masking on conversion efficiency," *Progress in Photovoltaics*, vol. 14, no. 7, pp. 589–601, 2006.
- [18] N. G. Park, J. Van De Lagemaat, and A. J. Frank, "Comparison of dye-sensitized rutile- and anatase-based TiO_2 solar cells," *Journal of Physical Chemistry B*, vol. 104, no. 38, pp. 8989–8994, 2000.
- [19] A. Lamberti, A. Sacco, S. Bianco et al., "Microfluidic sealing and housing system for innovative dye-sensitized solar cell architecture," *Microelectronic Engineering*, vol. 88, no. 8, pp. 2308–2310, 2011.
- [20] J. Bisquert, "Influence of the boundaries in the impedance of porous film electrodes," *Physical Chemistry Chemical Physics*, vol. 2, no. 18, pp. 4185–4192, 2000.
- [21] G. Barbero and A. L. Alexe-Ionescu, "Role of the diffuse layer of the ionic charge on the impedance spectroscopy of a cell of liquid," *Liquid Crystals*, vol. 32, no. 7, pp. 943–949, 2005.
- [22] Q. Wang, S. Ito, M. Grätzel et al., "Characteristics of high efficiency dye-sensitized solar cells," *Journal of Physical Chemistry B*, vol. 110, no. 50, pp. 25210–25221, 2006.
- [23] J. W. Ondersma and T. W. Hamann, "Impedance investigation of dye-sensitized solar cells employing outer-sphere redox shuttles," *Journal of Physical Chemistry C*, vol. 114, no. 1, pp. 638–645, 2010.
- [24] P. W. Atkins and J. DePaula, *Atkins' Physical Chemistry*, Oxford University Press, Oxford, UK, 9th edition, 2009.
- [25] J. Bisquert, "Theory of the impedance of electron diffusion and recombination in a thin layer," *Journal of Physical Chemistry B*, vol. 106, no. 2, pp. 325–333, 2002.